**Bangor University**

**DOCTOR OF PHILOSOPHY**

**Shear wave studies of interfacial lubrication**

Connor, Paul

*Award date:*
2001

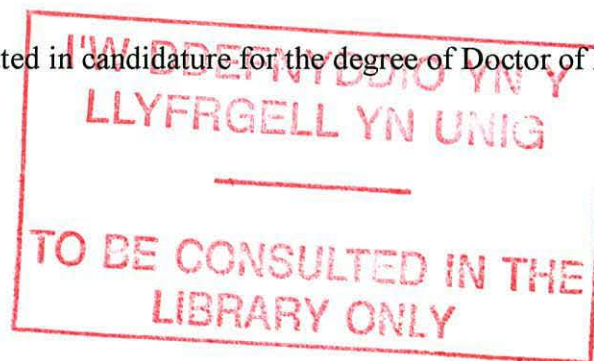*Awarding institution:*
Bangor University

[Link to publication](Link to publication)

# Shear Wave Studies of Interfacial Lubrication

by

Paul Connor MEng

A thesis submitted in candidature for the degree of Doctor of Philosophy

July 2001

School of Informatics
University of Wales, Bangor
Dean Street, Bangor, Gwynedd. LL57 1UT

# Dedication

To my family,
for their love and support

# Acknowledgements

# Summary

The AT-cut quartz crystal shear wave sensor was applied to the study of boundary layer lubrication.

The oscillating quartz crystal generates shear waves at its surfaces which propagate into acoustic loads in contact with the surfaces. Measurement of the electrical properties of the sensor allows the viscoelastic properties of the load to be derived. These shear waves are typically absorbed within 2-3 $\mu$m of the surface making the quartz crystal an ideal instrument for the study of interfacial phenomena.

An instrument was developed which allowed the friction force between the electrode surfaces of the quartz crystal and a matched acoustic load to be measured simultaneously with the viscoelastic properties of a lubricant layer between the surfaces. It was hoped that this instrument would fill the gap between the study of the friction of macroscopic engineering surfaces and the study of atomically perfect surfaces on the nanoscale.

Although the sensor proved unable to detect viscoelastic changes in a boundary lubricant layer it was possible to detect the formation of the layer and effects associated with it. The formation of thiol layers from solution and also by sliding of the dry sensor over a thiol multilayer were readily detected. The break-up of confined thin liquid layers was investigated. The response of the sensor to a macroscopic point contact was also studied.

# Table of Contents

# Sources of Materials

**Water** All water used in this work is ultra pure water which has been prepared by using the Millipore Milli-RO 60 system to produce single de-ionised water followed by the Millipore Super-Q system with ion-exchange, organic and 0.22 μm particle filters to produce 18 MΩ ultra pure water.

**Bovine Serum Albumin (BSA)** Sigma-Aldrich 9048-46-8

**Decane Thiol** 96% Aldrich 143-10-2

**Octadecane Thiol (ODT)** 98% Aldrich 2885-00-9

**Napthol Blue Black** 85% Sigma 1064-48-8

**Tween 20** BDH 43708 2Q

**Octanoate** 98% Aldrich 1984-06-1

**Oleate** 98% Aldrich 143-19-1

# 1 Introduction

Tribology is the study of mechanical interactions of two surfaces in relative motion and encompasses such processes as friction, wear and lubrication. A basic instrument used for investigating such interfacial phenomena is a tribometer.

A simplified form of this instrument is shown schematically in figure 1. A lightweight metal beam, B, supported at its centre by a frictionless pivot, P, is equipped with a pair of leaf springs at one end and a counter weight, C, at the other end. The surfaces under examination are the upper surface, F1, and the lower surface, F2. F1 is attached to the beam via the leaf springs, S1, S2, which are paired to confer mechanical rigidity and prevent unwanted torsional motion. F2 is attached to a motor driven platform, M, which can travel only in a direction perpendicular to the beam axis.

A force, N which acts normally to the plane defined by the friction surfaces can be accurately controlled by adjusting the position of the counter-weight so that the beam balances with the surfaces just in contact and then adding the weight W.

**(a) Side view**

B  Beam
P  Frictionless pivot
C  Counter-weight
M  Motor driven platform
W  Applied normal load
N  Normal force
F1 Upper friction surface
F2 Lower friction surface
G  Strain gauge
S1, S2 Leaf springs
D  Friction force
V  Platform motion

**(b) Top view**
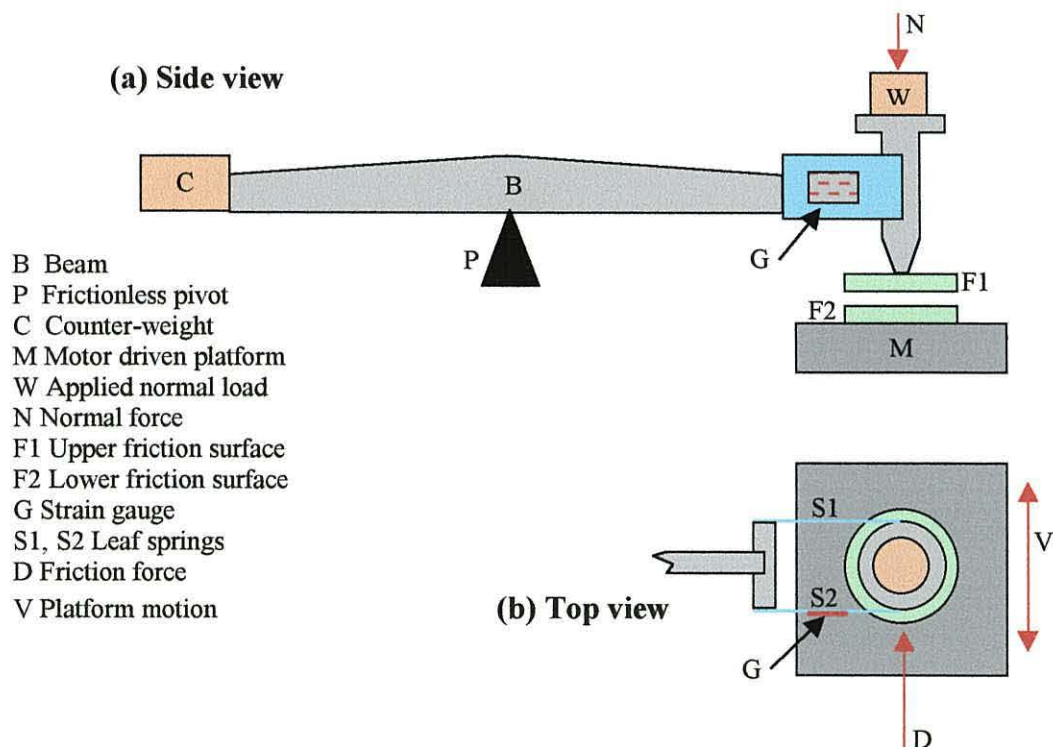
**Figure 1 Simple tribometer**

# 1 Introduction

As the platform moves, F1 is subjected to a lateral force D, figure 1b, the magnitude of which depends upon the friction between the two surfaces. D acts so as to bend the leaf springs and the bending is detected as an electrical output of a strain gauge, G, that is firmly attached to S2. For small deflections of the leaf spring the electrical output of the strain gauge is proportional to D and under this condition the deflection system is readily calibrated by measuring the electrical output when D is replaced by a known force which is directly applied. Measurement of W and D permits calculation of a coefficient of friction.

This basic technique was greatly refined by Tabor and Israelachvilli (Israelachvilli 1972) to yield information on interface interactions on the molecular scale. Using cleaved mica as the friction surfaces and restricting the contact area to about $10^{-10}$ m$^2$ they ensured that the contacting surfaces were atomically smooth. Using strain detectors of very high sensitivity it was possible to detect directly the forces involved in molecular interactions and to discern in some detail the role of adsorbed molecular species in boundary layer lubrication

While this and later variants of the surface force apparatus (SFA) have revealed a wealth of detail on molecular lubrication the friction surfaces, with the microscopic contact areas employed, necessarily posses a far higher degree of smoothness and structural perfection than can be achieved by using even the most highly polished surfaces in macroscopic contact. Thus there is a gap between the molecular detail on perfect surfaces provided by the SFA and the level of information obtainable on the best surfaces examined by a conventional tribometer. The quartz crystal sensor might contribute to filling the gap.

Quartz crystal plates electrically driven into mechanical resonance have been used as precise frequency standards for radio transmission since the 1930's, and in 1959 Sauerbrey showed that if a quartz plate is induced to oscillate at its resonance frequency in air and material is then added to the plate surface, the resonance frequency is reduced (Sauerbrey 1959). Since the resonance frequency of the plate could be typically 1 MHz and a frequency change of less than 1 Hz could be readily and accurately measured, Sauerbrey was able to demonstrate that a mass change as

small as 1 ng could be measured using this technique. This application of the quartz resonator was widely adopted and the device, particularly in the form of a thin so-called AT-cut crystal, became known as a quartz crystal microbalance (QCM) and is now used routinely to monitor and control the vacuum deposition of thin films.

At this stage the device could not operate as a free-running oscillator if it was mechanically loaded by immersion in a liquid, but during the 1980's circuits were developed which permitted the quartz crystal to resonate even when mechanically loaded with liquid. It quickly became apparent that mass detection was a special case of a wider capability. The device should be viewed as not just a resonator but as a source of shear waves generated at the mechanically oscillating crystal surface. The shear waves so formed propagate outwards from the surface into the liquid where they are absorbed. The liquid acts as a mechanical (viscoelastic) load on the crystal, and by measuring the change in both the electrical impedance and resonance frequency of the crystal, the viscoelastic properties of the liquid can be measured. Since in liquids the shear waves are generally absorbed within 2 to 3 μm of the crystal surface this technique can be used to examine the viscoelasticity of liquid films on surfaces. Fortunately when immersed in liquid the device maintains its sensitivity to molecular adsorption and thus can detect the formation of adsorbed monolayers. This technique thus offers the hope that molecular-scale processes that occur within 2 μm or so of the surface of macroscopic quartz crystal surfaces can be monitored.

To incorporate the quartz crystal sensor a tribometer of conventional design was constructed in which the friction surfaces (F1 and F2 in figure 1) were quartz crystals of nominally the same resonance frequency. The lower crystal was the shear wave sensor, its top surface acting as one friction surface while the lower surface of the upper crystal served as the other friction surface.

The main aim was to examine the feasibility of using the quartz crystal tribometer to study boundary layer lubrication but, due to its exploratory nature, the investigation has also touched on other related phenomena.

The basic theory of tribology is outlined in chapter 2 and is followed by a review of recent developments in the field.

# 1 Introduction

In chapter 3 following a general review of piezoelectric acoustic wave sensors attention is focused on thickness shear mode sensors; the type used in this investigation. A description of wave propagation and resonance conditions within the unloaded sensor is followed by an account of the response of the sensor to mechanical loading and propagation of shear waves within the load medium. Finally, based on this description, a mathematical model is presented which allows the response of the sensor to various forms of mechanical load to be predicted. This model is subsequently used to interpret data that is derived experimentally.

An account of the experimental techniques is presented in chapter 4. The arrangements for squeezing and shearing at the surfaces are described along with the techniques adopted for monitoring the formation of self-assembled molecular layer. The construction and operation of the quartz crystal tribometer is described and the design of the controlling and recording software is outlined.

Experimental results are presented in chapter 5. Some preliminary experiments were concerned with the behaviour of liquids confined between surfaces and the self-assembly of adsorbed layers was investigated. Before undertaking construction of the tribometer preliminary experiments were made to see if this approach held promise. The tribometer was then used to examine thin films in shear and this led to an investigation of the response of the quartz resonator to point-loading.

Chapter 6 discusses the major findings and in chapter 7 an attempt is made to assess the ability of the quartz sensor contribute to studies in tribology.

# 2 A Review of Developments in Tribology

Relative movement between contacting surfaces gives rise to frictional phenomena, thus an understanding of the nature of surfaces and what happens when surfaces come into contact underpins an understanding of friction.

## *2.1 The Nature of Surfaces*

In geometry a surface is defined as a two-dimensional boundary; in engineering, however, the situation is never so simple. Solid surfaces, even if they appear smooth to the eye or the finger, are usually rough on a microscopic scale. Moreover, material close to the surface may differ in a number of ways from the bulk material and the surface itself may carry contaminant layers. A metal, for example, will have a work-hardened surface layer several micrometers thick. This hardened layer is the result of smaller grain sizes and higher dislocation density and is caused by production processes and external forces applied in use. All metals apart from gold will have an oxide film above the hardened region. This is produced by the reaction of the metal with atmospheric oxygen. The oxide is covered by an adsorbed contaminant layer that consists mainly of water and oxygen molecules derived from the atmosphere. In industrial environments there may well be grease or oil films above this contaminant layer. Contaminated surfaces often have a low coefficient of friction initially until the grease or oil is worn away.

Most real surfaces are not regular but have surface asperities whose heights and slopes vary in a random way, although many machined surfaces, for example those cut with a lathe, do have some order which can be described in terms of roughness wavelengths. Typical engineering surfaces have asperities whose slopes are in the range five to ten degrees.

### 2.1.1 Surface Topography

Surface topography can be measured in a number of ways, for example, using a contact profilometer, an instrument which draws a sharp stylus across a surface and

records the vertical movement at regular sampling intervals. A computer may then be used to generate a statistical analysis of the data.

Early profilometers produced a single number output, the average roughness. This is defined as the arithmetic mean variation of the surface height from the mean height of the surface. The mean height of the surface is defined such that equal areas of the surface lie above and below it. Thus the average roughness, $R_a$, is given by

$$R_a = \frac{1}{L} \int_0^L |y(x)| \, dx \qquad (2.1)$$

where y is the height of the surface above the average height at a distance x along the profile under investigation and L is the length of the profile. A more practically useful measurement is the root mean square (r.m.s.) roughness, $R_q$, which is given by

$$R_q = \left[ \frac{1}{L} \int_0^L y^2(x) \, dx \right]^{\frac{1}{2}} \qquad (2.2)$$

Neither $R_a$ nor $R_q$ give any information about the shapes of the surface irregularities or any indication of the probabilities of finding surface heights within certain limits. A fuller description of the topography of the surface is given by the bearing area curve. The bearing area curve, introduced by Abbot and Firestone (Abbot et al 1933), is a plot of depth below a reference level parallel to a solid surface versus the percent
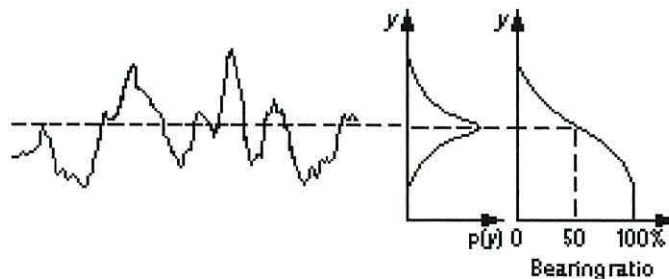


**Figure 2.1 Illustration of the derivation of the bearing area curve and height probability function p(y) from a surface profile** (Hutchings 1992)

bearing area intercepted by a horizontal line at that depth. Differentiating the bearing area curve gives the height probability function as shown in figure 2.1.

A few randomly rough surfaces, particularly ground surfaces, exhibit a normal height probability function and the bearing area curve is thus s-shaped. Many surfaces are not normal. For example, if a ground surface is polished the tips of the asperities will be removed and the normal distribution thereby distorted. A surface turned in a lathe is far from normal; the tips of the asperities are all approximately the same height and the troughs are also similar to each other in depth. In this case the bearing area curve approximates to a straight line.

Spatial variations in the surface can be specified by the root mean square slope and curvature. For a sample point on a profilometer trace the slope is defined as the height difference between that point and the next point divided by the sampling interval. The curvature is found by subtracting twice the height of the point from the sum of the heights of the two neighboring points and dividing by the square of the sampling interval.

The root mean square height, slope and curvature, while describing the shape of a surface, are dependent upon sample length and sampling interval. The reason for this is that variations in the surface with wavelengths greater than the sample length or shorter than the sampling interval are effectively filtered out of the profilometer trace. The curvature of the stylus will also filter out short wavelengths. The r.m.s. height is largely independent of sample length and interval, provided that the length is much greater than the interval, but slope and curvature are very sensitive to sampling interval and tend to increase without limit as the interval is made smaller and shorter wavelengths are included.

A recent development of the profilometer is the laser profilometer that has a optical (laser) stylus and scans an area rather than just a line. Since the laser profilometer does not make physical contact with a surface it is useful for investigating surfaces which are easily distorted or damaged.

More recently Scanning tunnelling microscopy (STM) and atomic force microscopy (AFM) have allowed surface topography to be examined on an atomic scale. In STM a sharp metal tip is brought within a few Ångstroms of the sample surface and a voltage is applied between the sample and the tip. The tip is scanned over the surface and at the same time the tunnelling current is kept constant by moving the tip perpendicular to the surface. This perpendicular displacement is used to create a height map of the surface. STM can only be used with surfaces of relatively high conductivity. In AFM a sharp tip mounted on a flexible cantilever is brought very close to the surface so that atomic forces between tip and surface cause the cantilever to bend. As the tip is moved across the surface it is displaced perpendicular to the surface in order to maintain the bending deflection of the cantilever and hence keep the force between tip and surface constant. In the same way as in the STM this perpendicular displacement is used to create a height map of the surface. The resolution obtained using AFM is generally slightly less than that obtained with STM but atomic resolution can sometimes be obtained (Persson 1998) and AFM has the advantage that it can be used with surfaces which are electrically insulating.

## 2.2 Contact of Surfaces

The fact that real surfaces are not simple two-dimensional interfaces means that the contact between surfaces, which gives rise to frictional phenomena, is correspondingly not simple.

### 2.2.1 Contact of Rough Surfaces

The interfacial friction between two contacting surfaces depends on the real area of contact, which is controlled by the surface topographies and the mechanical properties of the solids in contact. Examples for which the *apparent* area of contact is equal to the *real* area are rare. Mica can be cleaved to give atomically flat surfaces, and small asperities of very soft rubber can be completely flattened to give continuous contact. Apart from these examples, contacting surfaces are generally not smooth and the real area of contact will be a fraction of the apparent or nominal area, depending on the normal load and the microscopic topography of the surfaces.

### 2.2.2 Plastic Contact

When two rough surfaces approach each other a single asperity (or a few asperities) will touch first, making a single contact area known as a junction. For most materials the diameter of a junction will be small (~ 10 μm) and under a modest normal load the pressure on this junction is sufficient to cause a localised plastic deformation. As the junction is deformed the surfaces will approach more closely and additional asperities will come into contact. This process will continue until the real contact area is equal to the normal load divided by the penetration hardness of the material. If friction force is assumed to be the force required to shear cold welded junctions, then the friction force will be directly proportional to the real area. This simple model explains the law, described in section 2.3, that friction force is directly proportional to normal load.

For example, consider a steel cube of side 10 cm placed on a steel table. The weight of the cube and hence the normal load applied to its lower surface will be 100 N and the penetration hardness of steel is of the order $10^9$ N m$^{-2}$. This gives a real contact area of approximately 0.1 mm$^2$, only $10^{-5}$ of the apparent area. As the diameter of a junction is of the order 10 μm there would be around 1000 junctions formed at the interface of the cube and the table. Note that it is the normal load and not macroscopic shape that determines the real area of contact; if a piece of steel plate has the same weight as a steel ball then both will make the same contact area when placed on a horizontal surface.

The asperities of a rough surface are not easy to flatten by plastic deformation because their hardness corresponds to a contact pressure that is about a factor of three greater than the bulk yield stress (Quinn 1991). As the normal load on a specimen is increased, the real area of contact increases in proportion to the load. Once the contact area between the platen of a press and the specimen reaches about 1/3 of the apparent area the specimen will have reached its yield point.

The model of plastic contact appears to explain the first contact of two rough surfaces but real surfaces usually make contact more than once. Machine parts are expected to

give useful service over long time-scales and it seems unlikely that the same degree of irreversible deformation occurs each time between surfaces that are repeatedly brought into contact.

### 2.2.3 Elastic Contact

The Hertz equations (Hertz 1882) for spherical bodies show that, under simple elastic contact, the contact area is not directly proportional to load. However, it has been shown (Greenwood 1992) that, allowing for the distribution of asperity heights on a real surface, contact which is mainly elastic does in fact give a real area of contact which is directly proportional to load. The average size and contact pressure of the junctions remains constant because, as the surfaces approach, the growth in size and pressure of existing junctions is exactly balanced by the formation of new junctions with, initially, zero size and pressure. A very small fraction of the junctions will have a sufficiently high pressure to cause plastic deformation. This fraction is again constant because as an existing contact begins to yield plastically, many new elastic junctions are formed. Moreover, the interaction between the sub-surface deformation fields of adjacent asperities enhances their persistence at high loads (Childs 1973).

## *2.3 Classical Tribology*

Tribology is the study of interacting solid surfaces in relative motion. This diverse branch of science includes lubricants, lubrication, friction, wear and bearings. Tribology is involved in practically every aspect of life on Earth. Principles of tribology are employed in areas of science and technology as diverse as earthquake dynamics, human joints and the design of magnetic storage devices.

The study of tribology begins in prehistory with the use of friction and wear processes to shape stone tools and the striking of flint stones or rubbing of sticks to generate fire (Dowson 1998). In ancient times the value of lubricants was clearly appreciated. As early as 2400 BC some lubricant, possibly grease, oil or water, was used to reduce the friction of sledges used for the transportation of building blocks. The well-known painting from a grotto at El-Bershed, dated 1880 BC, shows an Egyptian pouring what is thought to be lubricant in front of a sledge drawing a large statue. Certainly a

chariot found in the Egyptian tomb of Yuaa and Thuiu and dating from about 1400 BC has traces of lubricant on the axle.

The first recorded scientific study of tribology was undertaken around 500 years ago when Leonardo da Vinci deduced the laws governing the sliding of rectangular blocks over flat surfaces, developed bearing materials and studied wear. Da Vinci's notebooks remained unpublished for hundreds of years and modern tribology began when the French physicist Guillaume Amontons rediscovered the laws of friction in the 17th century.

Amontons' conclusions now form two of the classical laws of friction. The first of these states that the friction force that resists sliding at an interface is proportional to the normal load which is squeezing the surfaces together. The constant of proportionality is known as the coefficient of friction and is defined as:

$$\mu = \frac{F}{N} \tag{2.3}$$

where F is the friction force at the interface and N is the normal load.

The second law states, somewhat counterintuitively, that the friction force does not depend upon the apparent area of contact. Amontons presented his findings to the Royal Academy in 1699 and met with some scepticism.

The third law is attributed to the 18th century French physicist Charles Augustin de Coulomb: the friction force is independent of the sliding velocity once motion starts. Coulomb investigated the influence of several factors upon friction; the nature of the friction surfaces, the extent of surface area, the normal pressure, the length of time that the surfaces remained in stationary contact and ambient conditions such as temperature and humidity. Coulomb considered the surface of a fibrous material, such as wood, to be covered by flexible, elastic fibres like the hairs on a brush. This view is very similar to the modern picture of sliding surfaces with grafted chain monolayers. Tomlinson explained the third classical law of friction in 1929 (Tomlinson 1929). Intuitively, one would expect friction force to rise with velocity; certainly it is well known that the drag force on a particle moving in a viscous medium increases with

velocity. Tomlinson showed that a velocity-independent friction force results if rapid processes occur somewhere in the system while the centre of mass of a block moves slowly relative to the substrate. In practice there are many materials that show a velocity functionality, particularly organic polymers (Ludema et al 1966) and boundary-lubricated surfaces (Tsukruk et al 1996) (Yoshizawa et al 1993a).

Bowden and Tabor (Bowden et al 1967) explained Amontons' observations around 1940: When surfaces such as metals come into contact with each other they touch at the tips of their asperities. The asperities deform plastically as discussed in section 2.2.2 until sufficient contact area to support the normal load is produced, with each asperity making contact over an area proportional to the load that it carries. Thus the real area of contact is generally much smaller than the apparent area and is directly proportional to the normal load. When the surfaces are clean the friction force is the force required to shear these contacts. This model explains the first two classical laws of friction. When there is an appreciable difference in hardness between the surfaces there is a tendency for the harder asperities to plough into the softer surface. In this case the friction force is made up of the sum of the shearing and ploughing components so that

$$F = F_a + F_p \qquad (2.4)$$

where $F_a$ is the contribution of shearing to the friction force and $F_P$ is the contribution of ploughing.

Advances in surface profilometry over the last two or three decades have provided a much more detailed view of the way in which surfaces deform when they are brought into contact. Using digital analysis of surface profiles, Greenwood and Williamson (Greenwood et al 1966) demonstrated that the distribution of asperity heights on many machined metal surfaces is essentially Gaussian. In the light of this finding these authors established a model of random surfaces consisting of asperities of identical radius whose heights had a Gaussian distribution. Contact between this model surface and a smooth, rigid plane was governed by the radius of curvature, r, the standard deviation of the asperity heights, σ, and the number of asperities per unit area. This

more realistic model of surface topography once again indicated that the real area of contact would be almost directly proportional to the applied load. Although their theory was derived for elastic contact, Greenwood and Williamson introduced a parameter known as the plasticity index, $\psi$, to allow the onset of plastic flow at asperities to be predicted. This is defined as

$$\psi = \frac{E^*}{H}\sqrt{\frac{\sigma}{r}}$$

and consists of two non-dimensional terms. The deformation properties are described by the ratio of the elastic to the plastic properties, $E^*/H$, where $E^*$ is the effective elastic modulus which depends on Young's moduli, $E_1$ and $E_2$, and on the Poisson's ratios, $v_1$ and $v_2$, for the materials of the asperity and the plane according to

$$E^* = \left(\frac{1-v_1^2}{E_1} + \frac{1-v_2^2}{E_2}\right)^{-1}$$

and H is the indentation hardness of the surface (a measure of the plastic yield stress of the asperities). The surface topography term is described by the ratio $\sigma/r$ – the quantity $(\sigma/r)^{1/2}$ is approximately equal to the average slope of the asperities. For values of $\psi$ much less than unity, asperity deformation is almost entirely elastic; on the other hand, if $\psi$ is significantly greater than unity there is a significant amount of plastic deformation.

When asperities deform plastically and sliding takes place, the shearing and ploughing components interact and slip-line theories (Childs 1992) have been introduced which incorporate the combined effects of both processes. The slip-line theory is based on describing the interfacial friction by a Tresca condition for which the frictional force is some function *m* of the bulk yield stress, where *m* is termed the friction factor. For modest values of the friction factor, shearing and ploughing can be treated additively. In general clean metal surfaces in contact will bond to each other, but in real systems oxide layers or other surface contaminants reduce the adhesion. Under these conditions, the two components of friction are not additive.

A relationship between adhesion and surface energy was discovered in the mid 1970s; it was observed that a sphere of rubber in contact with a flat surface spontaneously forms a circular contact whose diameter is governed by an equilibrium between the elastic energy stored in the rubber and the surface energy released at the interface. As tension is applied to the interface the diameter diminishes until an instability is reached which causes the surfaces to jump out of contact. Studies of this phenomenon have been presented by Johnson, Kendall and Roberts (Johnson et al 1971) and also by Derjaguin and his colleagues (Derjaguin et al 1975). Treating adhesion in terms of an energy balance explains the increase in effective adhesion strength of a junction due to viscoelastic hysteresis. There is now a solid body of work (Israelachvili 1992) on the effect of velocity, temperature, surface energy and hysteresis on the adhesion of elastomers and similar solids. These ideas also apply to the adhesion of metals, particularly at light loads. At higher loads it is necessary to account for plastic deformation.

Derjaguin went on to link friction to two processes: the force required to drag atoms of one surface over the other and a factor due to surface forces which increases with normal load. Thus

$$F = \mu(N + N_a) \tag{2.5}$$

where $N_a$ is the adhesive contribution to the normal load.

Although early experiments in friction mainly involved wooden surfaces, the industrial revolution brought with it an interest in metals and alloys. In the latter half of the last century tribology has been applied to a vast range of new materials. Briscoe and others have explained the frictional properties of polymers in terms of adhesion, shearing and ploughing (Briscoe 1992). Polymers exhibit a visco-elastic deformation process and their resistance to shear increases with contact pressure. Polymers are relatively poor thermal conductors and, therefore, frictional heating is likely to induce softening and surface melting. In some cases electronic charge on the surface can also contribute to adhesion and so dominate frictional behaviour (Tabor 1995). The

frictional properties of ceramics, mainly developed for high temperature applications, have also been studied recently (Tabor 1995).

Friction and especially wear are greatly reduced by the presence of a lubricant between the moving surfaces. In the ideal case sufficient lubricant is present to prevent contact between the surfaces.

### 2.3.1 Hydrodynamic Lubrication

In hydrodynamic or fluid lubrication the surfaces are completely separated by a film of lubricant, there is virtually no wear and the friction force arises solely from the viscosity of the lubricant. The friction coefficient of a hydrodynamically lubricated system is proportional to the viscosity of the lubricant and the speed of shearing and inversely proportional to the pressure applied to the surfaces (Bowden et al 1967). For a given system, lowering the viscosity of the lubricant lowers the viscous resistance to motion. There is, however, a limit in that as the viscosity is reduced the separation between the surfaces is also reduced. If the separation of the surfaces becomes sufficiently small, asperities may penetrate the film. For this reason the optimum lubricant has just sufficient viscosity to maintain an unbroken hydrodynamic film.

In many types of machines and mechanisms, particularly while stopping and starting, hydrodynamic lubrication breaks down due to extremes of pressure or temperature or low velocity of sliding. In this situation direct metallic contact between the friction surfaces, which would lead to increased wear and friction, can be very much reduced by the formation of a boundary layer of lubricant on the surfaces.

### 2.3.2 Boundary Layer Lubrication

Boundary films are formed by physical adsorption, chemical adsorption or chemical reaction, and behave very differently from the bulk hydrodynamic lubricant; the viscosity of a boundary lubricant film has very little effect on the friction, which is influenced by the nature of both the lubricant and the underlying surfaces.

When clean, unlubricated metal surfaces slide the oxide film or boundary layer can be worn away allowing metal-metal contact. Surface asperities weld together

momentarily and are broken apart to give wear particles. This adhesive wear is probably the main source of the friction force necessary to slide clean metal surfaces.

The transition from hydrodynamic to boundary lubrication can be very gradual, the wedge of lubricant separating the surfaces becoming thinner and the number of surface asperities penetrating the hydrodynamic film becoming greater. The main function of the boundary film is to reduce or eliminate metallic contact of the surfaces, thus reducing wear. Reducing friction is of secondary importance and for this the film itself must be easily sheared. Towards the end of the nineteenth century it became apparent that lubricant in layers close to the lubricated surfaces behaved differently from the bulk. The concept of boundary lubrication was introduced by Hardy in the early part of the twentieth century (Hardy 1936). He found that long chain organic molecules are very effective in reducing both wear and friction.

Fatty acids or long chain hydrocarbons with very polar end groups react with the solid surface to form a tightly held monolayer which is not removed even if the load is very high. The effectiveness of boundary layer lubrication depends on how strongly the molecule bonds to the metal surface.

The thickness of a boundary film has been shown to be of the order of one to two molecular layers (about 2 to 3 nm) and thus much less than the surface roughness (Bowden et al 1967). Since the layer is so thin, the addition of a very small quantity of a good boundary lubricant to a hydrodynamic lubricant can extend its protective properties when hydrodynamic lubrication breaks down. A number of properties affect the efficiency of a boundary lubricant.

### 2.3.2.1 Chain length

For paraffins the coefficient of friction falls with increasing chain length reaching a steady lowest value of about 0.05 (Bowden et al 1950). Fatty acids give similar results, but for a given chain length the fatty acid is a better lubricant than the corresponding hydrocarbon. For a fatty acid the coefficient of friction falls with increasing chain length, reaching a minimum when the chain length is 14 carbon atoms. The contact angle of a drop of methylene iodide increases and reaches a

maximum of about 70 degrees at the same chain length. This indicates that the monolayer has reached the most effective state of packing at this chain length (Bowden et al 1950).

The chain length affects the durability of the film (Bowden et al 1950). With fatty acids or amines of 18 carbons there is hardly any change to a layer after a slider is slid over the film 30 times. With shorter chains there is some wear of the film after repeated sliding and with chains of 8 carbon atoms there is a marked increase in friction after just 5 traversals. It is suggested that for chains of less than 12 carbon atoms the films are liquid-like and have poor durability, for chains of 12-15 carbon atoms the films resemble a plastic material with some durability but with longer chains the films have a more crystalline-like structure and high durability.

The higher melting point of longer chain materials also increases the temperatures at which they remain effective.

### 2.3.2.2 Temperature

Films frequently perform better when they are solid; for example, when a metal is lubricated by a non-reactive lubricant such as a paraffin, a reversible increase in friction and metallic transfer occurs at the bulk melting point of the lubricant. In this case, the occurrence of melting causes the adhesion between the molecules in the boundary film to be diminished and breakdown of the film takes place. When the lubricant reacts with the surface, for example fatty acid on steel, the increase in friction and transfer occurs at a much higher temperature and is less severe (Bowden et al 1950). The initial increase occurs at the softening point of the soap but the film continues to provide some protection because the molecules are still attached to the surface. The film does not completely break down until the temperature is high enough to cause the molecules to desorb from the metal surface.

In practice there are a few complications to this model. The boundary film is not a solid of fixed physical properties but a rheological material whose properties depend on temperature, pressure and rate of shear. It has been shown that the breakdown temperature is reduced when the normal load is increased (Matveevsky 1956). It has

also been shown that for moderate sliding speeds the breakdown temperature increases with the speed (Fein et al 1959).

*2.3.2.3 Metallic Transfer*

Studies using radioactive tracers and autoradiographic techniques show three important characteristics of the metallic transfer in boundary lubricated systems (Rabinowicz et al 1951). Firstly, the transfer is in the form of small particles indicating that the lubricant film is pierced at isolated points. Secondly, boundary lubricants are much more effective at reducing metallic transfer than they are at reducing friction. An effective lubricant may reduce metallic transfer by a factor of 100,000 or more while friction is reduced by only a factor of around 20. The third observation is that in reducing the amount of metallic contact it is the size of the transfer particles rather than the number that is affected. While the amount of metallic transfer is reduced by a factor of 100,000 the number of transfer particles may be reduced by a factor of 3 or 4. The fact that metallic transfer is reduced so significantly indicates that the friction of a boundary lubricated system arises mainly from shearing of the film itself rather than the underlying metal.

Interestingly, if hard and soft surfaces are compared it would be expected that the area of contact and hence the amount of boundary film being sheared should be much smaller in the case of the harder material. The smaller contact area should result in lower friction but in fact the friction in the two cases is roughly the same. A possible reason for this is that the shear strength of the film is proportional to the pressure to which it is subjected, so that a reduced area of contact is compensated by an increase in shear strength (Bridgman 1946)(Boyd et al 1945).

*2.3.2.4 Boundary Lubrication of Polymers*

Most of the work on boundary lubrication has concerned the lubrication of metals. There is, however, considerable interest in boundary lubrication of polymers, particularly in the context of textile technology (Bowden et al 1950). Generally the effect of boundary lubrication is less marked for polymers than for metals because the

polymer surface is not very different from the surface of a boundary film (Pascoe 1954).

## *2.4 Recent Developments*

In the late 1980s a number of new techniques were developed for investigating friction at smaller time and length scales. In addition, advances in the theoretical understanding of interactions at a molecular level and in computer technology have allowed more realistic molecular dynamics simulations of friction surfaces.

Understanding friction at small length scales (microtribology) is important in the drive for ever smaller micromechanisms. In magnetic recording devices, for example, recording head sliders with a mass of around 1 mg are required to work within 10 nm of the magnetic substrate (Kaneko et al 1996). The substrate must have a surface roughness of less than one nanometer and the lubricant film must be about one molecule thick. The mechanism manipulating the recording head must operate with an accuracy of just a few nm and exhibit virtually zero wear.

The main drive in this field, however, is the need to understand the relationship between microscopic processes and macroscopic observations. Macroscopic friction is the result of a combination of the macroscopic properties of the surface, such as roughness, with processes which take place on the atomic scale. Even if we can perfectly characterise a sliding interface we cannot accurately predict the friction that will occur. By devising experiments which operate at ever smaller distances and shorter times our understanding of these processes is greatly enhanced. At most interfaces contact occurs at numerous asperities and therefore single asperity contacts are of interest. Atomic scale friction can differ significantly from that observed on the macroscopic scale (Krim 1996b). Friction or tribology studied in well defined geometrics on the nanometer scale is known as nanotribology.

The difficulty in obtaining an atomic scale understanding of the mechanics of friction resides in the great complexity and variety of phenomena involved. During sliding, contact switches from one asperity to another, and asperity deformation can be followed by irreversible adhesion, chemical reaction, wear, chipping and fracture.

Experiments in nanotribology have given insight into these processes which usually occur in inaccessible buried interfaces.

### 2.4.1 Molecular Scale Friction

The study of friction on a molecular scale was first made possible in the 1960s through the development of the so-called surface force apparatus (SFA) by Tabor and Israelachvilli (Tabor et al 1969)(Israelachvili et al 1972). This instrument has been employed to study both static and dynamic properties of molecularly thin films sandwiched between molecularly smooth surfaces. The instrument consists of two crossed cylinders of atomically smooth mica; where the cylinders touch they make a very well defined small circular contact. The (very small) frictional forces developed across the contact are determined from spring displacements.

*2.4.1.1 Friction and Adhesion*

Bowden and Tabor (Bowden et al 1967) explained Amontons' law by showing that the real area of contact between rough surfaces is proportional to normal load. It follows that friction is proportional to real contact area and it was presumed that friction is a result of adhesive bonding at these contact points.

The SFA confirmed the deduction that friction is proportional to the true contact area (Israelachvili et al 1973) and subsequently established the link between friction and adhesion; friction does not correlate with the strength of the adhesive bond between the surfaces but rather is connected with the adhesive "irreversibility" i.e. the difference between the process of sticking and unsticking of two surfaces (Yoshizawa 1993a).

*2.4.1.2 Thin liquid films*

The force acting between two surfaces separated by a liquid film is a function of the surface separation. This force can be attractive, repulsive, oscillatory or more complex (Bhushan 1995b). The function is strongly dependant upon the structure of both the liquid molecules and the confining surfaces; for example, two crystalline surfaces whose separation is close to a small multiple of the molecular diameter may induce a

liquid film to solidify (Israelachvili et al 1990). The influence of the confining surfaces can cause the properties of the liquid molecules to be very different from those of the bulk; the freezing point may be higher or lower and molecular relaxation times can be very much longer (Granick 1991).

*2.4.1.3 Shear induced ordering transitions*

Both experiments with the SFA (Yoshizawa et al 1993b) and computer simulations (Diestler et al 1993) have shown that sliding surfaces can induce different types of ordered structure in thin liquid films and transitions between different states of order may give rise to stick-slip friction. The type of structure induced depends upon factors such as temperature or velocity. In general solid-like films give rise to stick-slip motion while liquid-like films give rise to low friction viscous-like smooth sliding. Between the liquid-like and solid-like states, amorphous-like films tend to produce high friction due to molecular entanglements and interdigitations (Bhushan 1995b). These states are not intrinsic properties of a shearing film but depend on temperature, pressure, applied load and the sliding velocity. The latter is not necessarily the same as the driving velocity but in general a more solid-like film is formed at higher velocities.

**2.4.2 Molecular Dynamics Simulations**

Advances in understanding of interatomic interactions coupled with the development of new methods of computer simulation have allowed modeling at higher spatial resolution and smaller time scales (Landman et al 1993). In these large-scale molecular dynamics simulations, Newtonian laws of motion are employed to calculate the trajectories of thousands of atoms with nanometer length and femtosecond time scales. These theoretical approaches guide the interpretation of experimental data, the design of new experiments and the prediction of new phenomena.

Simulations reveal differences between the behaviour of interfaces compared to that of bulk material and have been used to study atomic scale adhesion, interfacial wetting and surface damage (Landman et al 1990). Ductile contacts have been

observed in metals and brittle fracture in other materials (Landman et al 1992b). Atomic scale stick-slip friction has been observed (Landman et al 1992a).

Molecular dynamics simulations of interfacial films are used to investigate the relationship between the response of model lubricants and their physical and molecular characteristics. For example, simulations have shown a reduction in the friction of diamond films when long chain hydrocarbons are chemisorbed onto the surface (Harrison et al 1993). Phase transitions in compressed or sheared lubricant films have been observed together with stick-slip type friction as films melt and solidify (Thompson et al 1990)(Robbins et al 1991).

### 2.4.3 Atomic Scale Microscopy

The Scanning Tunnelling Microscope (STM) (Binnig et al 1982), developed in 1981, allows imaging of electrically conducting surfaces at atomic resolution, and has been used for imaging clean surfaces and lubricant molecules.

The development of the Atomic Force Microscope (AFM) (Binnig 1986) has made it possible not only to examine surfaces with atomic resolution but also, by using the sharp AFM tip as an ideal asperity, to investigate adhesion, friction, wear and lubrication at the atomic scale (Meyer 1990). The AFM can detect forces as small as a piconewton.

The AFM has been used to measure surface roughness on length scales from nanometers to micrometers. As the topography of most engineering surfaces is fractal, most commonly measured roughness parameters are scale-dependent (1995).

In the 1980s McClelland derived a simple model for wear-free friction based on vibrations of atomic lattices (McClelland et al 1992). Atoms close to the surface are set in motion by the sliding of atoms in the opposing surface. In this way mechanical energy is converted to sound and heat. Solids have distinct resonant frequencies and the amount of phonon energy absorbed depends upon which frequencies are excited. This model offers the possibility that very small solids with fewer resonant

frequencies might exhibit nearly frictionless sliding. The development of the AFM allowed McClelland and Mate to measure friction atom by atom (Mate et al 1987).

In the late 1980s the Friction Force Microscope (FFM) (Mate et al 1987) had been developed and, in ultra-high vacuum, allowed the study of a diamond tip with a contact area less than 20 atoms in extent (Meyer 1990). In this situation the friction force did not depend on the normal load, and the shear stress required to maintain sliding turned out to be about $10^9$ N m$^{-2}$ (roughly the same as the force required to fracture steel). Clearly, even when the atomic nature of a sliding contact is completely known it is still not possible to predict the friction force.

The friction force map of freshly cleaved highly ordered pyrolytic graphite has been found to have the same periodicity as the atomic scale topography but the peaks in friction are displaced and have a different shape relative to the peaks of topography (Ruan et al 1994). Local variations in the microscale friction of scratched surfaces have been found to be significant and appear to depend on the local slope rather than the surface height distribution (Ruan et al 1994)(Bhushan et al 1995a).

Directionality is occasionally observed in macroscopic friction but is more common in microscale friction because some surfaces have asymmetric asperities and surface finishing processes preferentially deposit material on one side of the asperities and, on the atomic scale, because crystalline surfaces are not isotropic.

The microscale coefficient of friction is often much smaller than that of the macroscale because the indentation hardness and modulii of elasticity are much greater for small contact areas and low loads; moreover at the macroscale trapped wear particles plough into the surfaces, adding an extra component to the friction force (Bhushan et al 1995). At higher loads, the microscale coefficient of friction increases towards values comparable with macroscale measurements (Bhushan et al 1995). It is likely that microcomponents sliding under light loads should exhibit very low friction and virtually zero wear.

*2.4.3.1 Scratching, wear and indentation*

Using the AFM tip as a model asperity, the effect of contact and shearing of a single asperity system can be investigated (Bhushan et al 1995). The AFM can also be used for machining and fabricating nano components (Bhushan et al 1995).

The manner in which surface materials are removed has been studied (Bhushan et al 1994). Microwear develops as repetitive shearing takes place. Wear is initiated at microscratches and thus scratch-free surfaces are very resistant to wear.

The surface hardness and modulus of elasticity can be measured on micro and pico scales and their spatial variation can be mapped (Bhushan et al 1995b). This technique can be used to evaluate surface modifications, thus the transfer of nano-particles or even single molecules can be detected (Ruan et al 1993).

*2.4.3.2 Atomic Scale friction regimes*

The friction and adhesion produced by a single asperity can be related to atomic structure. Four distinct friction regimes have been detected at the atomic scale and, while experiments have been devised which operate in one of the regimes, most practical systems involve a mixture of effects occurring at the same time.

*1. Wearless friction regime* In this regime there is no damage to the surfaces and no permanent structural modification. Energy is dissipated by phonon or electron excitation mechanisms. Using an AFM tip as a single asperity, an atomic scale stick-slip motion was observed as the tip 'ratcheted' over the lattice atoms of the substrate (Salmeron 1998). The contact area was estimated to contain tens or hundreds of atoms due to elastic deformation and yet the periodicity of the stick-slip motion was one lattice constant. This suggests that tip and/or surface atoms are distorted into registration with the lattice. The stored elastic energy is dissipated as lattice vibrations and the energy of these vibrations is redistributed into a spectrum of lower frequencies through anharmonic interactions that couple the normal modes of the system and end up as heat and sound waves. In this wearless regime it has been found that Amontons' law does not hold and instead friction is proportional to the contact area (Carpick 1996). Johnson, Kendall and

Roberts' model (Johnson et al 1971) which relates contact area to both load and interfacial energy gives a very good fit to the experimental data.

*2. Viscoelastic Regime* In this regime molecules at the interface are displaced or deformed but return to their original configuration on a timescale comparable with the sliding time. After a recovery time the surface is undamaged. Viscoelastic effects are most easily observed in self assembled monolayers (SAMs). Studies of alkylsilane and long chain alcohol or fatty acid monolayers using the SFA have shown that loads down to 20 MPa produce large numbers of gauche distortions in the terminal end groups (Du et al 1995). The last C-C bond of the alkane chain lies nearly parallel to the surface when under load, giving a compression of about 0.1 nm in the chain. This distortion disappears when the load is removed. Chain tilting, deeper molecular distortion and even a reversible displacement of entire molecules at high loads have been observed to be strongly related to film packing density and the strength of intermolecular forces in the layer (Lio et al 1997)(Xiao 1996). AFM studies using a sharp tip have shown the periodicity of alkanethiol layers at low loads; when the load was increased the periodicity of the underlying gold lattice was observed and when the load was reduced the film recovered and the periodicity of the film was again observed (Liu et al 1994). Blunt tips of radius over 100 nm failed to displace molecules because the surrounding film could not accommodate all the molecules which would be displaced. In this situation the thiol layer supports the tip at loads well in excess of the plastic deformation limit of the gold substrate (Salmeron et al 1995).

*3. Atomic-scale Wear Regime* Irreversible displacement or dislodging of surface atoms leads to the formation of defect vacancies and interstitials near the surface. Foreign atoms such as oxygen or carbon can become incorporated into the surface (Salmeron 1998). As this damage is limited to a few layers very near the surface it is difficult to detect without atomic scale resolution and hence it is often confused with the wearless regime. In layered materials such as mica, layer-by-layer wear has been observed (Hu et al 1995). An AFM tip has been shown to produce a 10 Å deep hole in mica in a single scan at sufficiently high pressure, corresponding to

one layer of mica. At lower loads wear occurred only after several scans and at lower loads still, no wear was observed after many scans. It is possible the point defects created at moderate loads anneal or diffuse away from the contact area unless they are produced at a sufficiently high rate.

*4. Deep Damage Regime* In this regime massive atomic displacements and lattice distortions are produced which extend into the bulk of the sample, creating dislocations, plastic deformation and eventual detachment of debris particles (Salmeron 1998).

*2.4.3.3 Boundary Lubrication*

AFM and FFM have been used to study Langmuir Blodgett films and SAMs (Lio et al 1997) (Meyer et al 1992). SAMs are more important in boundary lubrication. Atomic-scale microscopy can be used to determine the thickness of a monolayer and its response to a single asperity contact and shearing. The macroscopic observation that friction increases when chain length decreases is also observed at the nanoscale (Salmeron 1998). At sufficiently low loads friction curves are convex due to the influence of elastic deformation on contact area. As the load increases, the curves flatten and at some point become concave, with a rapid increase in friction due to removal of lubricant molecules from the contact region. This transition occurs at lower loads for shorter chains (Salmeron 1998). This dependence on chain length is due to varying packing density. The stability of the chains arises from the van der Waals interactions between them (Salmeron 1998).

**2.4.4 Quartz Crystal Shear Wave Generator**

The extreme acceleration generated on the surface of a quartz crystal shear wave sensor makes it suitable for measuring slip between the surface and layers of condensed gas a few atoms thick (Kanazawa 1997). The operation of the quartz crystal is described in chapter 3. Krim and co-workers condensed single atom thick layers of various materials onto the gold or silver electrodes of AT-cut quartz crystals (Krim et al 1988). These films reduced the frequency and the vibrational amplitude of the crystals, providing a measure of the extent to which the films track the movement

of the electrode surface. The quartz crystal shear wave sensor operates on a timescale sufficiently short to allow investigation of the velocity dependence of atomic scale friction. In 1989 it was found, surprisingly, that friction forces for liquid krypton films were about 5 times higher than those for solid films (Krim 1996a). This result was explained by Robbins and co-workers using computer simulation (Smith et al 1996). These authors showed that liquid krypton atoms, being more mobile than atoms in solid krypton, could 'get stuck' more easily in the gaps between the atoms of the solid gold electrode. (This situation is very different from that of lubrication where it is the liquid film that is being sheared not the interface.) It was found that when the film was made two atoms thick instead of one, the friction increased by 27% (Daly et al 1996). This is attributed to the fact that the two layer system has more modes of lattice vibration and can thus absorb more phonon energy (Krim 1996a).

In 1999 Laschitsch and Johannsmann reported the application of quartz crystal resonators for friction measurements in the MHz region (Laschitsch 1999). The surface of a crystal was approached with a small sphere and the resonant frequency and Q factor measured as a function of the sphere-crystal distance. Once elastic contact was established, the resulting shifts in frequency and Q were attributed to an increased stiffness of the resonating system. Strongly different behaviour was observed between high friction metal-metal interfaces and low friction fluoropolymer interfaces. For high friction interfaces, an excess dissipation of energy was observed which was attributed to frictional processes in the contact zone.

### 2.4.5 Re-writing the rules

Theoretical and experimental studies of nanotribology have extended and, in some cases, fundamentally altered the picture that had developed from macroscale studies.

Recent progress in nanotribology clearly demonstrates that the laws of macroscopic friction do not hold at the atomic scale. The laws can be written more generally:-

- Friction force depends on the relative ease of sticking and unsticking two surfaces i.e. friction is proportional to the degree of irreversibility of the normal force rather than its magnitude.

- Friction force is directly proportional to the *real* area of contact. (This is also true for large contacts in cases where the nominal area of contact is equal to the real value).

- Friction force is directly proportional to the sliding speed of the interface at the true contact points, provided that the surfaces are not allowed to heat and the sliding speed remains well below the speed of sound so that lattice vibrations can dissipate energy.

- The discrepancy between the microscopic and macroscopic laws is largely explained by the fact that the true or real contact area between macroscopic surfaces is usually proportional to the normal load, whilst in the case of microscopic contacts the loading is also a function of adhesion.

AFM investigations of scratching, wear and indentation provide useful insight into the failure mechanisms of bulk materials.

The future development of micromechanical devices is likely to draw more on nanotribology because of the difference in frictional behaviour of small components compared to larger ones.

# 3 Theory of Piezoelectric Acoustic Wave Sensors

Acoustic wave devices can be made in such a way that the wave propagation within the device is affected by external conditions such as the adsorption of material onto the device or immersion in a viscous fluid. Piezoelectric acoustic devices are particularly attractive as sensors because the electrical outputs of the device respond to changes in the mechanical inputs, moreover they can exhibit high sensitivity, low signal to noise ratio, are of small physical size and are low in fabrication costs.

## 3.1 The Piezoelectric Effect

The piezoelectric effect is the electric polarisation that occurs as a result of mechanical strain in certain types of crystalline solid. When the structure of a crystal is not centrosymmetric the application of a mechanical strain changes the distribution of charge on the atoms and bonds comprising the crystal in such a way that a net electric polarisation of the crystal results. The magnitude of the polarisation is proportional to the strain and its sign depends upon the strain direction.

Crystals exhibiting this direct piezoelectric effect also exhibit the converse piezoelectric effect whereby the application of an electric field produces a mechanical strain in the crystal. Thus mechanical strain in piezoelectric crystals occurs as a result of either mechanical stress or an electrical field and electric polarisation occurs as a result of either an electric field or mechanical stress. This coupling between electrical and mechanical effects allows a piezoelectric crystal to act as a transducer.

Of the 32 recognised classes of crystals 20 exhibit the piezoelectric effect but very few of these crystals are actually useful. Quartz provides the highest efficiency in combination of mechanical, electrical, chemical and thermal properties required for making piezoelectric sensors.

Other applications of piezoelectricity make use of poly-crystalline ceramics instead of crystals. Ceramics have the advantage that they can be manufactured in almost any required shape or size. Piezoelectric properties can then be induced in the ceramic by poling, that is by the application of a d. c. electric field. During the process of poling

the mechanical and electric axes of the ceramic can be precisely orientated in relation to the shape of the ceramic. A particularly useful piezoelectric ceramic is lead zirconate titanate (PZT) and variations of this ceramic are used in applications as diverse as ultrasonic cleaning, delay lines and sensors.

## 3.2 Surface Wave Sensors

An acoustic wave sensor will have a high sensitivity to surface perturbations if there is a concentration of acoustic energy at its surface. (Ballantine et al 1997) Surface wave sensors, in which acoustic waves are propagated along the surface, can be divided into three types.

### 3.2.1 Surface Acoustic Wave (SAW) Devices

In 1885 Lord Rayleigh (Rayleigh 1885) discovered a mode of acoustic wave propagation which is confined to the stress-free boundary imposed at the surface of an isotropic solid. In this mode, known as a surface acoustic wave (SAW) mode, coupled compression waves and shear waves propagate together along the surface. The amplitude of the wave decays rapidly with distance into the bulk and the surface acts as a wave-guide with most of the wave energy being contained within one wavelength of the surface. At shorter wavelengths the acoustic energy is confined more closely to the surface and sensitivity to surface perturbations is increased.

In SAW devices the waves are generated by lithographically printed interdigital electrodes on the surface of a piezoelectric crystal (White 1970). These electrodes form a transducer that operates most efficiently when the SAW wavelength matches the transducer periodicity.

The surface-normal displacement component makes the SAW unsuitable for liquid sensing applications because this component generates compression waves in the fluid; this dissipated power leads to excessive attenuation of the wave.

### 3.2.2 Acoustic Plate Mode (APM) Devices

Acoustic Plate Mode (APM) devices are a class of sensors which utilise a shear horizontal acoustic plate mode (SH-APM) in which particle displacement occurs

predominantly parallel to the surface of the device and normal to the direction of propagation. These devices were developed for sensing in liquids since the absence of a surface-normal displacement allows the acoustic wave to propagate without dissipating excessive energy into the liquid.

APM devices are fabricated on thin single-crystal quartz which acts as a waveguide. At a resonance, acoustic energy is confined between the upper and lower surfaces of the crystal with displacement maxima at both surfaces. This makes both surfaces equally sensitive to surface perturbations.

Acoustic waves are excited and detected by lithographically patterned interdigital electrodes on one side of the plate. In order to prevent mode interference APM devices are operated in a single mode by using a measurement circuit with a bandwidth that is less than the frequency separation between modes. The transducers are most efficient when the electrode periodicity matches the wavelength of the excited mode. Surface features perturb the wave velocity, and hence the frequency, of each mode.

Mode propagation characteristics are affected by a number of interactions including surface mass accumulation, viscous entraining of liquid and acousto-electric coupling between evanescent plate mode electric fields and the liquid. Acousto-electric coupling is due to the layer of bound charge generated at the surface of the device which couples to ions and dipoles in the liquid.

### 3.2.3 Flexural Plate-Wave (FPW) Devices

In a flexural plate-wave (FPW) device an acoustic wave is excited in a membrane that is only a few micrometers in thickness. Like other acoustic sensors, the FPW can sense phenomena that cause its phase velocity to change. However, in contrast, the FPW can be dimensioned so that its phase velocity is lower than that of most liquids. The FPW device functions well in a liquid environment because, when the device is in contact with liquid, a slow mode of propagation exists in which no energy is radiated from the plate.

Since the plate is so thin, the mass per unit area is increased significantly by the adsorption of material onto the plate from either liquid or vapour phases. This mass adsorption can be detected by its effect of decreasing the phase velocity. The opposite effect, an increase in phase velocity, occurs when tension in the plate is increased either by strain in the frame surrounding the plate or by a differential gas pressure across it.

Another unique feature of the FPW device is that the amplitudes of the displacements associated with the waves are large compared to waves of the same power in other sensors. Normal displacements of up to 100 nm can occur when an acoustic wave of a few milliwatts propagates through a plate a few micrometers thick. This large-amplitude motion can be used to produce useful kinetic effects such as the transport of granular solids or the pumping and mixing of fluids. In this way the FPW device can function as both a sensor and an actuator.

## *3.3 Thickness Shear Mode (TSM) Sensors*

A thickness shear mode (TSM) sensor typically consists of a thin disk of quartz with circular gold electrodes patterned on both sides as illustrated in figure 3.1. Flags are provided for electrical connection to the electrodes. The orientation of the disk with respect to the crystalline orientation of the quartz is chosen so that the application of a voltage between these electrodes results in a shear deformation in a direction parallel to the electrodes. The direction in which shear deformation takes place is denoted as the X-direction.
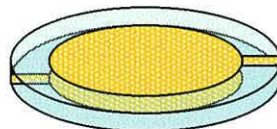


**Figure 3.1 Thickness shear mode (TSM) resonator consisting of a thin disk of quartz with circular gold electrodes on both faces.**
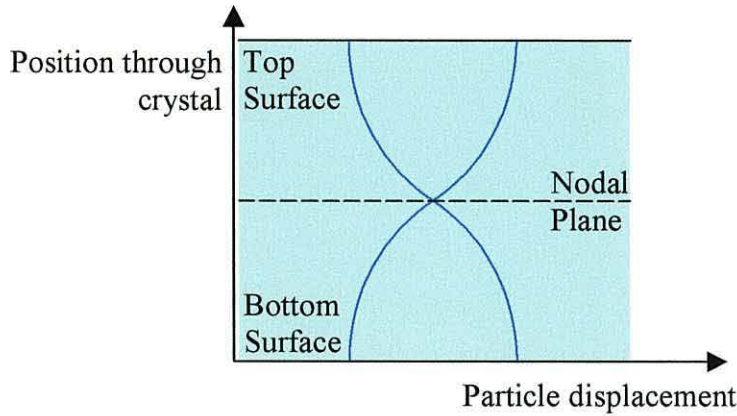
**Figure 3.2 The fundamental thickness shear resonance condition
in a quartz crystal excited by surface electrodes.**

The applied electric field is confined to the volume where the two electrodes overlap, this is the mechanically active volume of the crystal surface. It is in this region that acoustic waves are generated and it is this region that is sensitive to acoustic loads on the surfaces in contact with the gold electrodes. The connecting strips of the two electrodes are positioned opposite to each other (figure 3.1), this allows electrical connections to be made to the crystal without their contributing to the acoustically active volume. The mechanical mountings of the crystals and, if necessary any liquid seals, are confined to the edge of the crystal to minimise their impact on the active volume. Where only one face is to be used for sensing, the other face is maintained in air which has negligible acoustic load.

When an alternating voltage is applied between the electrodes of a TSM resonator in air shear waves of opposite polarities are generated at the two faces. These waves propagate normally away from the faces and the mechanical displacement in the crystal is a superposition of these waves. When a wave propagates from the top face to the bottom it undergoes a phase shift of $l_q\omega/v_q$ where $l_q$ is the thickness of the crystal, $\omega$ is the angular frequency of the waves and $v_q$ is the velocity of shear waves in quartz. The wave is reflected from the bottom face with a phase shift due to reflection of $\pi$ and propagates from the bottom face to the top with a phase shift of $l_q\omega/v_q$. The wave is then reflected from the top face with a phase shift of $\pi$ having undergone a total round trip phase shift of $2l_q\omega/v_q + 2\pi$. Figure 3.2 shows the

fundamental resonance condition where the incident and return waves are coherent with each other giving constructive interference. The maximum particle displacement occurs at the surfaces and a nodal plane in which there is no displacement occurs midway between the two surfaces. Other resonances occur when the round trip phase shift is an integer multiple of $2\pi$, thus the frequency of a resonance is given by

$$f_M = \frac{M v_q}{2 l_q} \tag{3.1}$$

where M is the integer mode number. An alternate description of a resonance is that the thickness of the crystal must be an integer number of half wavelengths, i.e.

$$l_q = \frac{M \lambda}{2}$$

Since only odd harmonics produce surface displacement, M must always be an odd number.

The shear wave velocity in quartz is equal to $\sqrt{\mu_q / \rho_q}$ where $\mu_q$ is the shear stiffness and $\rho_q$ the mass density of quartz. As thickness, density and shear stiffness are all functions of temperature, it follows that the resonance frequency of a quartz TSM resonator is also a function of temperature. A useful property of quartz is that it is possible to arrange for the effects of temperature-induced changes in these three
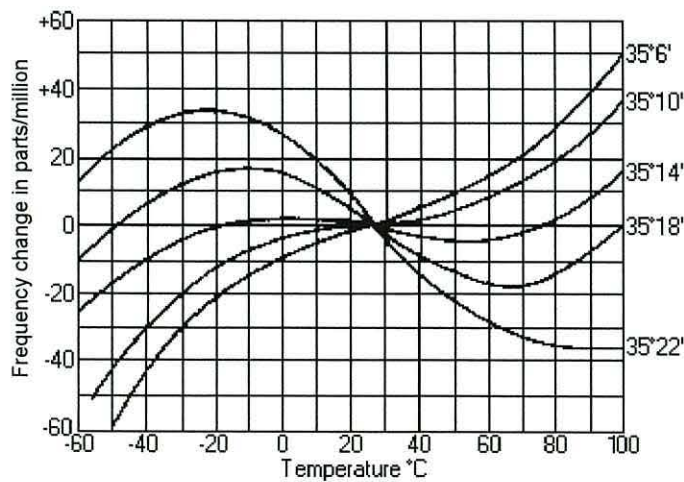


**Figure 3.3 Frequency-temperature curves for AT-cut crystals with various angles of cut.** (Bottom 1982)

parameters to approximately cancel each other out giving a stable frequency over a useful temperature range. This is achieved by cutting quartz plates at certain angles to the crystal axis (Bottom 1982). The AT-cut has a very small temperature dependence around room temperature as illustrated in figure 3.3.

The fundamental resonance frequency of the quartz crystal can be found experimentally by incorporating the device into the feedback path of an oscillator which will then oscillate at the fundamental resonance. The resonant frequency can also be found by using an impedance analyser to find the frequency at which the electrical impedance is at a minimum. Material in contact with the surface becomes part of the mechanical resonating system forming an acoustic load that can be detected by its effect on the electrical resonance.

The first use of the TSM as a sensor was as a microbalance in vacuo to measure metal deposition rates (Sauerbrey 1959). More recently the TSM has been shown to operate in contact with liquids (Numura et al 1980), (Konash et al 1980) enabling its use as a liquid phase microbalance and, with the electrode that is in contact with the liquid doubling as one electrode of an electrochemical cell, as an electrochemical microbalance (Bruckenstein et al 1985). It has now been shown that the sensors can be used in a more sophisticated way to measure the visco-elastic properties of a material (Barnes et al 1992), (Johannsmann et al 1992).

This description of the resonance assumes an infinite plate of quartz, excited by electrodes of zero mass. In a finite plate the wave motion is not uniform but, for a disc-shaped plate resonator, varies across the surface with a maximum at the centre of the circular electrodes

### 3.3.1 Resonance of a Finite Crystal

The fundamental thickness shear resonance of an infinite planar crystal excited by electrodes of zero mass is dependant only upon the thickness of the crystal and the shear wave propagation velocity as described in equation 3.1. When excited by electrodes of finite mass the effect of the electrode mass will be to lower the resonance frequency. When the electrodes are of finite extent the confinement of the resonance will have the effect of raising the resonance frequency. Thus the
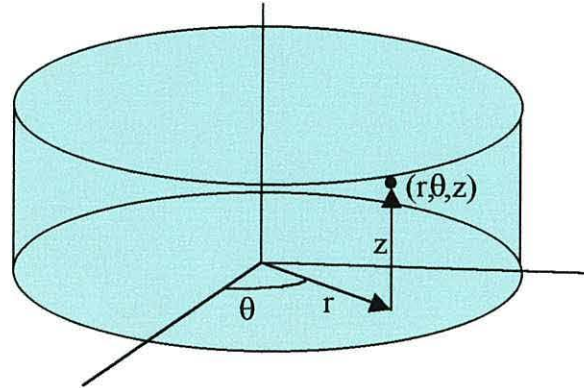
**Figure 3.4 Defining a point within the resonator using the cylindrical coordinate system**

resonance will have the effect of raising the resonance frequency. Thus the fundamental resonance frequency of a crystal with finite electrodes will be different from that given by equation 3.1. Finite electrodes will also produce a non-uniform sensitivity across the surface of the sensor.

The real crystal with circular electrodes can be considered as a cylindrical resonator with height equal to the thickness of the crystal and radius equal to that of the electrode. The radius is ill-defined because of the edge effects of the electric field and because the flags of the electrodes distort the cylindrical geometry, however the cylinder is a good approximation. Waves in this system are described using the cylindrical co-ordinate system illustrated in figure 3.4 and the wave equation can be written as

$$\frac{1}{r}\frac{\partial}{\partial r}\left(r\frac{\partial U}{\partial r}\right)+\frac{1}{r^2}\frac{\partial^2 U}{\partial\theta^2}+\frac{\partial^2 U}{\partial z^2}+\left(\frac{2\pi}{\lambda}\right)^2 U = 0 \qquad (3.2)$$

where U is the wave intensity and $\lambda$ the wave length in an unbounded medium. The geometry of the electrodes sets the boundaries of the resonator to r=R, z=0 and z=$l_q$ where R is the radius of the electrode and $l_q$ is the thickness of the quartz. Assuming the crystal to be isotropic it can be shown that the solution to equation 3.2 can be written as the product of the functions of independent variables thus

$$U = R(r)\Theta(\theta)Z(z)$$

By substituting into the wave equation it is possible to show that $\Theta(\theta)$ and $Z(z)$ are harmonic functions and that $R(r)$ is a Bessel function. Specifically

$$U = J_n(kr)\cos(\alpha\theta)\cos\left(\frac{\beta\pi z}{l_q}\right)$$

where $k$, $\alpha$ and $\beta$ are constants determined by the boundary conditions. In the thickness shear modes of interest a node exists at the centre and anti-nodes at each surface so $\beta=1$. Since $\cos(\alpha\theta)$ must be of period $2\pi$, $\alpha$ must be integral or zero. If $\alpha$ is zero then U does not depend on $\theta$ and is uniform at any given r. The wave intensity at the plane surface of the resonator is thus given by

$$U_S = J_n(kr) \tag{3.3}$$

The Bessel function of integer order is oscillatory in nature. It has been shown (Lamont 1942) that modes of oscillation for cylindrical resonators exist at frequencies given by

$$f_{Mnm} = \frac{v_q}{2}\left[\left(\frac{M}{l_q}\right)^2 + \left(\frac{k_{nm}}{\pi}\right)^2\right]^{\frac{1}{2}} \tag{3.4}$$

where $k_{nm}R$ is the $m^{th}$ root of the $n^{th}$ order Bessel function $J_n(kR) = 0$ and M is the integral mode number as in equation 3.1. In the case of an infinite planar crystal $R \to \infty$ and $k_{nm} \to 0$ and the above equation reduces to equation 3.1.

The non-uniform motion of the crystal surface gives rise to a non-uniform sensitivity across the surface. The sensitivity of a TSM sensor to a point load is a function of the position on the surface of the resonator. Cumpson and Seah showed that the mass sensitivity function, that is the sensitivity to a mass load at a point on the surface, is proportional to the square of the particle velocity at that point (Cumpson et al 1990). Where the acoustic load under investigation is a uniform film an averaged sensitivity can be used. In the case of a point load or a non-uniform film the sensitivity function must be taken into account.

### 3.3.2 Compression Waves

A finite AT-cut crystal does not operate as a simple shear wave generator but generates a significant longitudinal wave component as well. These longitudinal waves arise from three sources; (i) flexural modes in the crystal which are coupled to the shear wave modes (Mindlin 1951), (ii) the non-uniform surface velocity of the shear wave component (Martin et al 1989a) and (iii) a mode conversion of the shear waves which arises if the crystal axis is not normal to the crystal face (Shutilov 1988).

Unlike shear waves, which have a decay length of about 0.25 μm in water, longitudinal waves can propagate over long distances in liquids and can be reflected from boundaries to form standing waves. These standing waves introduce an additional load on the sensor. Studies have shown that when a glass plate parallel to the sensor surface is moved relative to the surface (Martin et al 1989a), (Lin et al 1995) or when a water-air boundary that is parallel to the sensor moves because of drainage or evaporation (Reddy et al 1998) the response of the sensor is periodic with respect to the sensor-reflector separation. The periodicity has been found to be equal to half the wavelength of the longitudinal waves in the liquid under investigation thus confirming its origin.

The total mechanical load, $\overline{Z}_L$, measured by a TSM resonator under liquid is thus: -

$$\overline{Z}_L = \overline{Z}_S + \overline{Z}_P$$

where $\overline{Z}_S$ is the shear wave acoustic impedance at the sensor surface and $\overline{Z}_P$ is the impedance due to the longitudinal pressure waves. The acoustic impedance of the shear wave is defined as the ratio of shear stress to particle velocity. The acoustic impedance of the longitudinal wave is defined as the ratio of compressive stress to particle velocity. The over-bars signify that these are complex quantities. Both components affect the electrical response of the resonator being transformed by the same piezoelectric coupling factor, $\Phi$.

It is important to consider the effect of the longitudinal waves when designing TSM sensor experiments in liquids, especially when the time-scale of the experiment is such that evaporation of the liquid may cause significant changes in liquid depth, or

when low frequency mechanical vibrations perturb the liquid surface. If the longitudinal wave component is not taken into account then it will appear as noise and drift in the measurements. In many cases the response of the sensor to the longitudinal standing waves may be significantly larger than the shear wave effect being studied.

The cyclic changes arising from changing standing wave patterns may be eliminated either by arranging for the sensor to be a fixed distance away from a reflecting surface, for example the wall of the container if the sensor is mounted perpendicular to the liquid surface (Reddy et al 1998), or by fixing a conical or rounded 'spoiler' above the sensor surface in order to scatter the longitudinal waves and prevent standing wave patterns from being set up.

### 3.3.3 The TSM Sensor Under Acoustic Loads

The behaviour of the TSM sensor with an acoustic load was originally described by Mason (Mason 1948) in terms of an acoustic-electrical transformer. Figure 3.5 illustrates an equivalent circuit derived by Johannsmann (Johannsmann et al 1992) for a TSM resonator where one face is in air and the other is in contact with an acoustic load $Z_L$. The left hand side of the circuit represents the electrical connection to the electrodes and the electrical capacitance, $C_0$, of the device. The right hand side of the
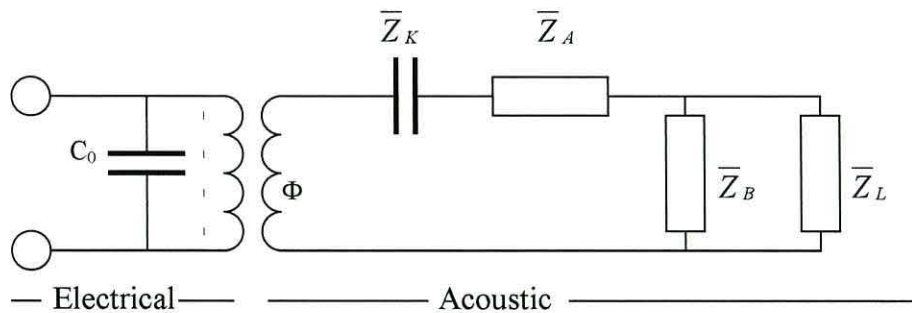


$C_0$ Electrical capacitance
$\Phi$ Electro-acoustic transformer ratio
$\overline{Z}_K, \overline{Z}_A, \overline{Z}_B$ Acoustic impedances of the crystal
$\overline{Z}_L$ Acoustic load applied to the sensor

**Figure 3.5 The Electro-acoustic Equivalent Circuit of a Thickness Shear Mode Resonator**

circuit represents the mechanical properties of the device and the acoustic load. The components on the mechanical side of the circuit are all acoustic impedances. The piezoelectric effect is represented by the acoustic-electrical transformer. For a resonator of thickness $l_q$, with an active area A and a piezoelectric coefficient e, the transformer ratio is $1{:}\Phi$, where

$$\Phi = \frac{A\,e}{l_q} \tag{3.5}$$

This can be thought of as the ratio of shear stress to voltage or electric current to particle velocity. The acoustic impedances of the circuit elements in figure 3.5 are given by

$$\overline{Z}_k = \frac{i\,4\Phi^2}{\omega\,C_0}$$

$$\overline{Z}_A = -2i\,Z_q\,\cot\omega l_q/2v_q$$

$$\overline{Z}_B = 2i\,Z_q\,\tan\omega l_q/2v_q$$

where $Z_q$ is the characteristic impedance of the resonator, given by $Z_q = A\rho_q v_q$ and $\omega$ is the angular frequency, given by $\omega = 2\pi f$.

The acoustic load is made up of a real component and an imaginary component.

$$\overline{Z}_L = R_L + i\,X_L$$

Equation 3.1 defines the fundamental resonance of the sensor as $f_0 = v_q/2l_q$. At frequencies close to this resonance when $f - f_0 = \Delta f \ll f_0$ the following approximations can be made

$$\cot\omega l_q/2v = -\tan\frac{2\pi\,\Delta f\,l_q}{2v} \cong -\frac{\pi}{2}\frac{\Delta f}{f_0}$$

$$\tan\omega l_q/2v \cong \frac{2}{\pi}\frac{f_0}{\Delta f}$$

The cot term, and hence $Z_A$, is small while the tan term, and hence $Z_B$ is large. $Z_B$ can be neglected as it is expected to be much larger than $Z_L$. Away from the resonance $Z_B$ becomes much smaller and it is then $Z_L$ which may be neglected.

A series mechanical resonance is found at a frequency f, near to $f_0$, when the reactive component of the mechanical impedance equals zero. This condition can be expressed as

$$\frac{2\Phi^2}{\pi f C_0} + \frac{\pi Z_q \Delta f}{f_0} + X_L = 0 \tag{3.6}$$

If there is no acoustic load and the sensor operates entirely in air, resonance will occur at a frequency $f_0'$ where

$$\frac{2\Phi^2}{\pi f_0' C_0} + \frac{\pi Z_q \Delta f_0}{f_0} = 0$$

and $\Delta f_0 = f_0' - f_0$. Replacing $f_0'$ with $f_0$ in the first term, since $\Delta f_0 \ll f_0'$ gives the approximation

$$f_0' = f_0 - \frac{2\Phi^2}{\pi^2 Z_q C_0}$$

The frequency $f_0'$ is the resonance frequency of an unloaded sensor, it is reduced from $f_0$ by the piezoelectric coupling which modifies the wave velocity in the crystal. This result can be used to simplify equation 3.6 to

$$\frac{\pi Z_q \Delta f}{f_0} + X_L = 0$$

thus the frequency shift due to the acoustic load is given by

$$\Delta f = -\frac{f_0 X_L}{\pi Z_q} \tag{3.7}$$

Since the reactive component of the mechanical impedance equals zero at the mechanical resonance all that remains of the mechanical impedance is the resistive component of the acoustic load $R_L$. When this is transferred to the electrical side of

the circuit using the transformer ratio $\Phi$ the electrical impedance of the sensor at resonance is given by

$$\overline{Z}_e = \frac{A R_L}{4\Phi^2 + i 2\pi f C_0 s R_L}$$

This can also be expressed in terms of the modulus $|Z_e|$ and phase $\phi_e$

$$|Z_e| = \frac{A R_L}{4\Phi^2}\cos\phi_e \tag{3.8}$$

Thus via equations 3.7 and 3.8 the frequency and electrical impedance of the fundamental series resonance of the TSM sensor can be used to derive the acoustic load.

### 3.3.4 Shear Wave Propagation

*3.3.4.1 In bulk materials*

The propagation of a shear wave with an angular frequency $\omega$ into a viscoelastic material in contact with the surface of the sensor is described by a complex shear wave velocity, $\overline{v}$, given by

$$\frac{1}{\overline{v}} = \frac{1}{v} - \frac{i\alpha}{\omega} \tag{3.9}$$

where $v$ is the real shear wave velocity and $\alpha$ is an attenuation coefficient in the material. A characteristic acoustic impedance of a bulk material with a density $\rho$ is given by

$$\overline{Z} = \rho \overline{v} \tag{3.10}$$

The properties of the material may also be expressed as a viscoelastic shear modulus, $\overline{G} = G' + iG''$, where $G'$ is the rigidity modulus representing elastic storage of acoustic energy in the material and $G''$ is the loss modulus which represents viscous loss of acoustic energy. The shear modulus of a material is related to the characteristic impedance by

$$\overline{Z} = \sqrt{\rho \overline{G}}$$ (3.11)

*3.3.4.2 In a finite layer*

When the acoustic load in contact with the sensor is a finite layer, shear waves can be reflected from both surfaces of the layer and it becomes part of the resonating system. The acoustic load upon the sensor depends not only upon the bulk viscoelastic properties of the material but also upon the thickness of the layer. The acoustic impedance of a layer of thickness $l_L$ is given by

$$\overline{Z}_L = \overline{Z} \tanh\left(\alpha_L + \frac{i\omega}{v_L}\right) l_L$$ (3.12)

assuming that shear waves do not propagate beyond the layer. This is the case where the layer is bounded at its outermost surface by air. When the shear wave propagates beyond the layer into a different material account must be taken of its properties.

*3.3.4.3 In multiple layers*

The acoustic impedance measured by the sensor is affected by all layers into which the shear wave propagates. A layer n of thickness $l_n$ and density $\rho_n$ which is bounded by a layer n+1 at its outermost surface (i.e. The surface furthest from the sensor) has an impedance at its innermost surface which is given (Barnes et al 1992) by

$$\overline{Z}_n^i = \overline{Z}_n \frac{\overline{Z}_{n+1}^i + \overline{Z}_n \tanh(\theta_n l_n)}{\overline{Z}_n + \overline{Z}_{n+1}^i \tanh(\theta_n l_n)}$$ (3.13)

where $\theta_n = \alpha_n + i\omega/v_n$. The impedance of a system comprising multiple layers can be derived by repeatedly applying this equation.

### 3.3.5 Types of Acoustic Load

*3.3.5.1 Elastic Material*

In a material with a small loss modulus and small shear wave attenuation coefficient the wave propagates readily. The imaginary part of the complex shear wave velocity (equation 3.9) is very small and the velocity is well approximated by its real part. The acoustic load of such a material on the sensor is given by

$$\overline{Z}_L = i X_L = i \rho_L v_L \tan \frac{\omega l_L}{v_L} \qquad (3.14)$$

Because $v = \sqrt{G'/\rho}$ the load can be cyclic as the layer thickness, density or rigidity modulus changes. If the layer is thin or $G'/\rho_L$ is large the tan term can be approximated by $\omega l_L/v_L$, the load becomes $X_L = \rho_L \omega l_L$ and the frequency shift due to this load by

$$\Delta f_s = -\frac{2f_0^2 \rho_L l_L}{Z_q} \qquad (3.15)$$

This is the Sauerbrey microbalance equation (Sauerbrey 1959), the product $\rho_L l_L$ is the mass per unit area of the layer.

### 3.3.5.2 Bulk Viscoelastic Material

If a layer has sufficient thickness that the product $\alpha_L l_L$ is greater than 3 then the term $\tanh i\omega l_L/v_L$ is approximately unity. In this case the measured acoustic impedance of the layer is approximately equal to the characteristic acoustic impedance of the bulk material. The elastic storage and viscous loss moduli of the layer are given by

$$G' = (R_L^2 - X_L^2)/\rho_L \qquad (3.16)$$

$$G'' = 2 R_L X_L/\rho_L \qquad (3.17)$$

### 3.3.5.3 Viscous Newtonian Fluid

In the case of a bulk viscous fluid there is no elastic storage and the real and imaginary components of the acoustic load are equal. The viscosity can be found by

$$\eta = \frac{2X_L^2}{\rho \omega}$$

The frequency shift due to this load is given by

$$\Delta f_s = -\frac{f_0^{3/2} \rho}{Z_q \alpha} \qquad (3.18)$$

## 3 Theory of Operation of Acoustic Wave Sensors

*3.3.5.4 Layer bounded by two quartz crystals*

The shear wave sensor can be used to probe the viscoelastic properties of a confined liquid film in which the quartz crystal sensor forms one confining surface and an identical crystal that is not electrically connected into the circuit forms the second. If the thickness of the crystals are identical then the second crystal forms a matching load and does not contribute to the acoustic load detected by the sensor. The thickness, $l_q$ of each crystal is half the wavelength at resonance, i.e.

$$l_q = \frac{v_q \pi}{\omega}$$

and thus from equation 3.14 $\overline{Z}_L$ is zero.

The thickness of the matching crystal does not have to match precisely that of the sensor, its acoustic impedance will be small and constant and the acoustic impedance determined by the sensor arises almost entirely from the confined visco-elastic layer between the two crystals. This means that, while the layer under investigation is physically confined, the confining surface is not part of the acoustic system and the layer sensed on its own as if it were bounded by air.

*3.3.5.5 Non-uniform Films*

When the deposited material is not uniform or does not cover the whole of the sensor surface the response of the sensor depends upon the position of the deposited material on the surface as described in section 3.3.1. In the case when the sensor acts as a simple microbalance the shift in frequency can be expressed as:

$$\Delta f = \int_0^{2\pi} \int_0^R S(r,\theta) m(r,\theta) \, dr \, d\theta \qquad (3.19)$$

where $m(r,\theta)$ is the mass distribution, $S(r,\theta)$ the mass sensitivity, R the radius of the sensor and integration is over the crystal surface. The sensitivity has been shown (Cumpson et al 1990) to be proportional to the square of the particle velocity at the resonator surface. Other studies (Martin et al 1989b), (Hillier et al 1992) have shown that the sensitivity can be approximated by a Gaussian function of r, the radial distance from the centre of the electrodes. This function does not drop to zero at the

edge of the active area but fringes onto the unplated part of the crystal. The fringing is reduced if one face of the sensor is convex (Cumpson et al 1990)and is increased if the sensor is operated in a more viscous medium.

### 3.3.5 Modelling the Acoustic System

In the interpretation of experimental data and the evaluation of the acoustic model considerable use has been made of computer-aided computation and mathematical analysis. Specifically the MathCad (MathSoft Inc.) program has been used to produce models that predict the behaviour of the resonator under acoustic loads. Several MathCad worksheets are included in the appendix and referred to in the appropriate sections.

A typical worksheet modelling the matching crystal situation described in section 3.3.5.4 is given below to illustrate the essential features. In this worksheet the resonance frequency and impedance is determined when a quartz crystal layer of variable thickness is in good acoustic contact with an AT-cut quartz crystal sensor of 10 MHz nominal resonance frequency. The parameters of the resonator and the matching quartz crystal layer are defined in figure 3.6. Values for these properties are as close as possible to those of the actual sensors and layers used in the experiments so that the results can be compared directly. The layer and sensor density and shear wave velocity are identical in this case. The properties are to be investigated over a range of layer thicknesses and an array is defined to do this. The first item in the array is set to zero to model the response of the unloaded sensor.

An array of frequencies is then chosen (figure 3.7) over which the impedances will be determined. A series of impedance values are then generated as outlined in figure 3.8, for each layer thickness.

A series of impedance curves are generated, one for each value of layer thickness. The items ZCo, $\Phi$, Zk, ZA and ZB refer to components in the model described in section 3.3.3 (figure 3.5), these values do not depend upon the layer thickness as they are properties of the resonator itself. The acoustic impedance of the layer, ZL, depends upon both the frequency and the layer thickness. Hence ZL has both f and l as

subscripts in order to generate a matrix of values for varying frequency and layer thickness while the others have only f as a subscript. The four acoustic impedances are combined, transformed to the electrical side of the circuit and combined with the electrical capacitance to give a total impedance for the whole sensor.

The resulting impedances, in logarithmic form, are shown as functions of frequency in figure 3.9. From these plots the minimum impedance (Zmin) is found for each layer thickness and the value of the impedance and the corresponding frequency (Fzmin)

---

**Resonator Parameters**

This section defines the characteristics of the thickness shear mode resonator.

| | |
|---|---|
| Thickness | $lq := 1.66 \cdot 10^{-4} \cdot m$ |
| Effective Electrode Area | $A := 2.8 \cdot 10^{-5} \cdot m^2$ |
| Permittivity of Quartz | $\varepsilon := 40.71 \cdot 10^{-12} \cdot farad \cdot m^{-1}$ |
| Crystal Capacitance Co | $Co := \dfrac{A \cdot \varepsilon}{lq}$ |
| Density of Quartz | $\rho q := 2650 kg \cdot m^{-3}$ |
| Shear Wave Velocity in Quartz | $vq := 3320 m \cdot s^{-1}$ |
| Characteristic Impedance | $Zq := \rho q \cdot vq$ |
| Piezoelectric Coefficient | $e := 9.65 \cdot 10^{-2} \cdot coul \cdot m^{-2}$ |
| Fundamental Resonance fo | $fo := \dfrac{vq}{2 \cdot lq}$     $\omega o := 2 \cdot \pi \cdot fo$ |

**Layer Parameters**

This section defines the characteristics of the second layer and generates an array of thickness values at which the model will be evaluated.

| | |
|---|---|
| Density | $\rho 2 := \rho q$ |
| Shear Wave Velocity | $v2 := vq$ |
| Attenuation | $\alpha := 0$ |
| Thickness (array) | $l := 1, 2 .. 200$ |
| | $l2_l := (0.998 + (0.00002 l)) \cdot 1.6651 0^{-4} \cdot m$ |
| Set first element to zero (unloaded sensor) | $l2_1 := 0$ |

**Figure 3.6 Parameters of the quartz crystal resonator and matching crystal**

determined, figure 3.10. Experimentally the quartz crystal oscillator is expected to track the frequency of minimum impedance. The program in figure 3.10 simulates this.

Finally plots of resonance frequency and minimum impedance are shown in figure 3.11. From these it is possible to deduce the best matching crystal conditions as in figure 3.12. It will be seen that the best condition has no effect on the resonance frequency of the unloaded sensor crystal. Zmin, which is the resistive component of the acoustic load (see section 3.3.3) increases from 3 to approximately 4.7 ohm as a result of the optimum thickness of the matching crystal load.

| | |
|---|---|
| **Frequency range** | $f\_lower := 9.960 \cdot 10^6 \cdot Hz$ |
| | $f\_upper := 10.00 \cdot 10^6 \cdot Hz$ |
| **Resolution** | $res := 100 \cdot Hz$ |
| **index** | $f := 1, 2 .. \dfrac{f\_upper - f\_lower}{res}$ |
| **Frequency array** | $\omega_f := 2 \cdot \pi \cdot (f\_lower + f \cdot res)$ |

**Figure 3.7 Generation of frequency array for impedance modelling**

| | |
|---|---|
| Electrical Capacitance | $ZCo_f := \dfrac{1}{j \cdot \omega_f \cdot Co}$ |
| Transformer Ratio | $\Phi := \dfrac{A \cdot e}{lq}$ |
| Acoustic Impedances | $Zk_f := j \cdot \dfrac{4 \cdot \Phi^2}{\omega_f \cdot Co}$ |
| | $ZA_f := -2j \cdot A \cdot Zq \cdot \cot\left(\dfrac{\omega_f \cdot lq}{2 \cdot vq}\right)$ |
| | $ZB_f := 2j \cdot A \cdot Zq \cdot \tan\left(\dfrac{\omega_f \cdot lq}{2 \cdot vq}\right)$ |
| Layer Impedance | $ZL_{f,1} := A \cdot \rho 2 \cdot v2 \cdot \tanh\left(\dfrac{j \cdot \omega_f}{vq} \cdot l2_1\right)$ |
| Total acoustic Impedance | $Zac_{f,1} := Zk_f + ZA_f + \dfrac{ZB_f \cdot ZL_{f,1}}{ZB_f + ZL_{f,1}}$ |
| Transformed to electrical | $Ztrans_{f,1} := \dfrac{Zac_{f,1}}{4 \cdot \Phi^2}$ |
| Total electrical Impedance | $Z_{f,1} := \dfrac{ZCo_f \cdot Ztrans_{f,1}}{ZCo_f + Ztrans_{f,1}}$ |

**Figure 3.8 Impedance calculations for each layer thickness given in figure 3.6 and frequency range, figure 3.7**

$$AZ_{f,1} := \log\left(\left|Z_{f,1}\cdot mho\right|\right) \qquad AF_f := \frac{\omega_f}{2\cdot\pi\cdot10^6}$$

**Impedance Curves**

$AZ_{f,1}$

$AZ_{f,90}$

$AZ_{f,109}$

$AZ_{f,130}$

Log of Impedance

$AF_f$

Frequency (MHz)

Unloaded
0.16647 mm
0.16653 mm
0.16660 mm
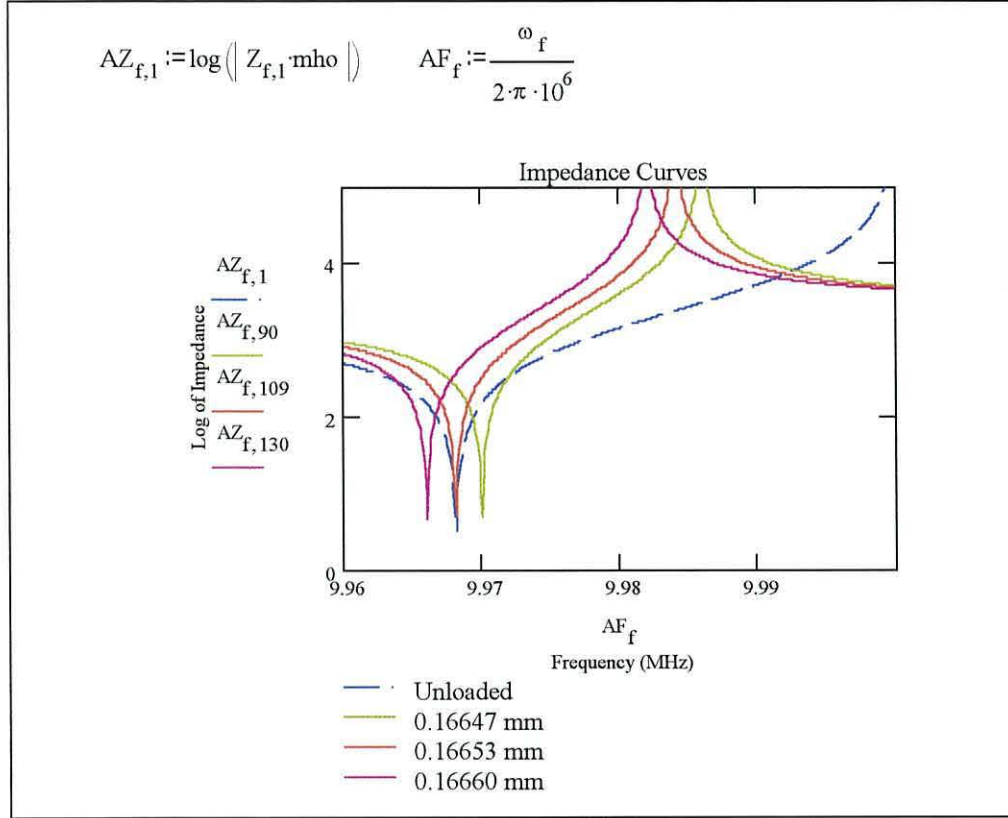
**Figure 3.9 Impedance as a function of frequency for three different thicknesses of matching crystal and for zero thickness (unloaded sensor)**

$$minima(M) := \begin{vmatrix} j \leftarrow 1 \\ a \leftarrow min(M) \\ for \ i \in 1..\,rows(M) \\ \quad minima \leftarrow i \ if \ M_i = a \\ minima \end{vmatrix}$$

$$mins(M) := \begin{vmatrix} for \ i \in 1..\,cols(M) \\ \quad for \ j \in 1..\,rows(M) \\ \quad\quad A_j \leftarrow M_{j,i} \\ \quad mins_i \leftarrow minima(A) \\ mins \end{vmatrix}$$

$$idx := mins(AZ) \qquad Fzmin_1 := \frac{\omega_{(idx_1)}}{2\cdot\pi} \qquad Zmin_1 := \left|Z_{(idx_1),1}\right|$$
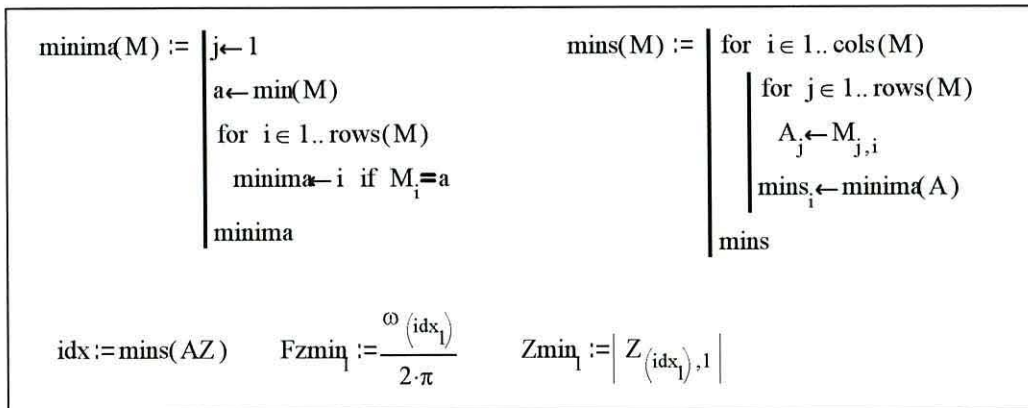
**Figure 3.10 Programs for locating the value of minimum impedance, Zmin, and corresponding frequency, Fzmin.**
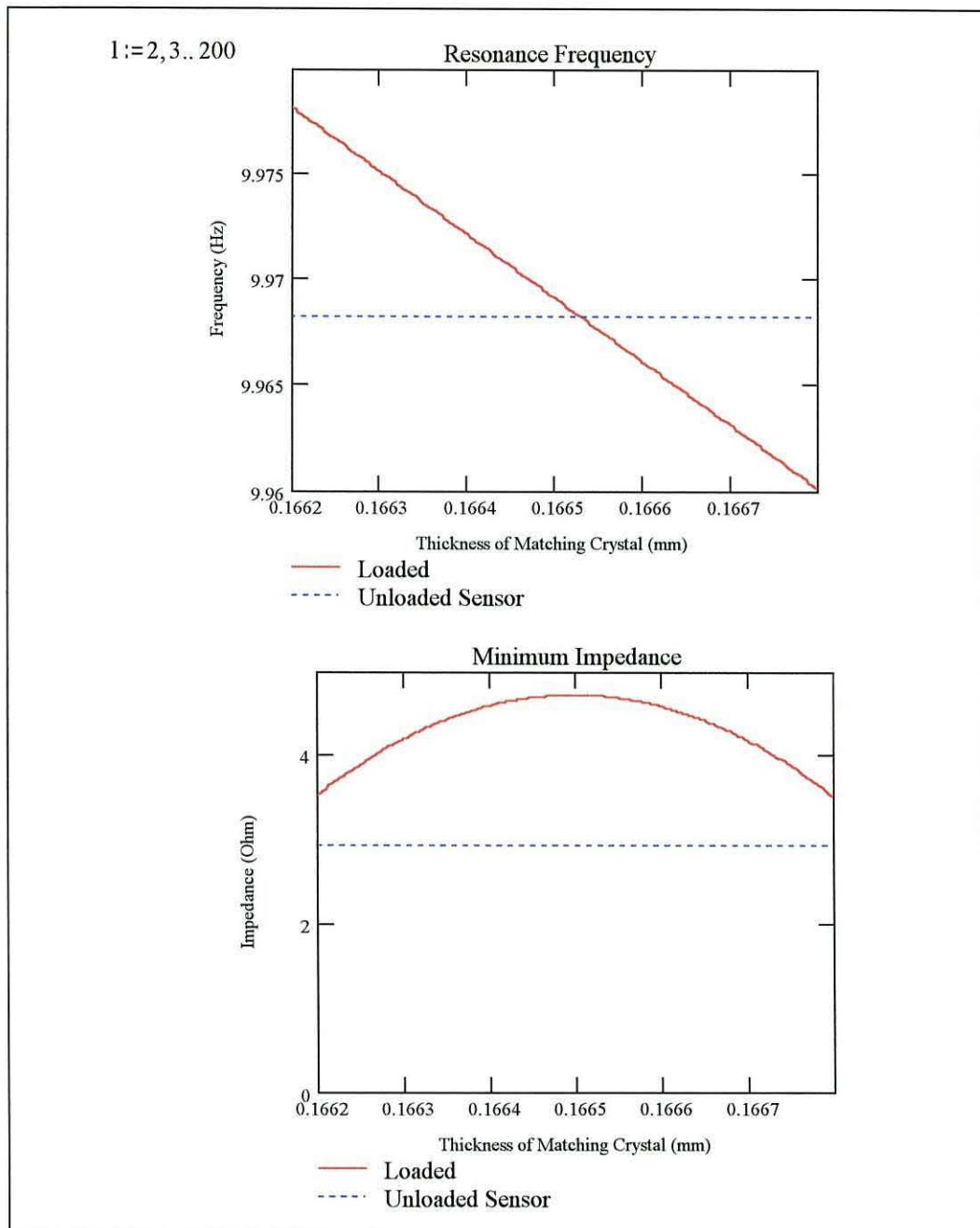
**Figure 3.11 Resonance frequency and minimum impedance as functions of the thickness of the matching crystal**

| | |
|---|---|
| Resonance Frequency of Unloaded sensor | $\text{Fzmin}_1 = 9.968 \cdot 10^6 \ \text{Hz}$ |
| Impedance of Unloaded sensor at resonance | $\text{Zmin}_1 = 2.916 \ \Omega$ |
| Resonant Frequency with best matching crystal. | $\text{Fzmin}_{109} = 9.9682 \cdot 10^6 \ \text{Hz}$ |
| Impedance at resonance with best matching crystal | $\text{Zmin}_{109} = 4.702 \ \Omega$ |
| Thickness of best matching crystal. | $\text{l2}_{109} = 1.6653 \cdot 10^{-4} \ \text{m}$ |

**Figure 3.12 Best matching crystal thickness deduced from figure 3.11**

# 4 Experimental Techniques

The exploratory nature of this project has placed a strong emphasis on the development of experimental techniques which utilise the quartz shear wave sensor to study the thin layers associated with interfacial lubrication and the development of an efficient means of recording the data.

## *4.1 The Measurement System*

Figure 4.1 shows a block diagram of the system employed to measure the parameters of the quartz sensor.

### 4.1.1 The Principle of Measurement

The resonant frequency of the quartz sensor is measured by connecting the sensor into the feedback path of a driving oscillator. The circuit oscillates at the frequency at which the sensor has least impedance; that is the series resonant frequency of the sensor. When an acoustic load changes the resonant frequency, the oscillator tracks the resonance so that at any instant the output frequency of the oscillator is equal to the series resonant frequency of the sensor. This output is measured by a frequency counter connected to a desktop computer.

There is a small error in the output frequency caused by stray capacitances in the circuit which are added to the sensor impedance but as this capacitance is small and remains constant for both the loaded and unloaded cases its effects can be neglected.
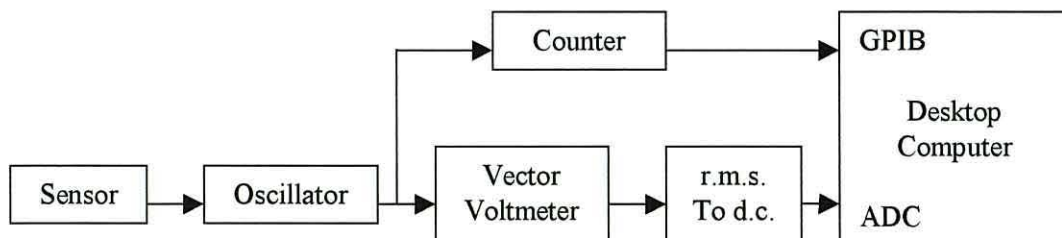


**Figure 4.1 The Quartz Sensor Measurement System**

In order to derive the impedance of the sensor at its series resonance frequency it is necessary to measure the electrical current flowing through it, the voltage across it and the phase difference between the voltage and current. Oscillators have been developed which provide voltage and current outputs and a vector voltmeter is used to measure the amplitude of these signals and the phase difference. Two of the vector voltmeter outputs are in the form of alternating current (a.c.) signals which must be converted first to direct current (d.c.) and then into digital signals which can be read by the computer. The computer applies a correction to the phase measurement and then a scaling factor is applied to give a value in radians. The voltage and current measurements do not need to be scaled because their scaling factors are equal and are thus cancelled out in the calculations. The real and imaginary parts of the electrical impedance are then calculated according to the equations: -

$$\text{Real} = R \frac{V}{I} \text{Cos}\, \phi - R \qquad\qquad (4.1)$$

$$\text{Imag} = -R \frac{V}{I} \text{Sin}\, \phi \qquad\qquad (4.2)$$

where V and I are the voltage and current signals, $\phi$ is the corrected phase signal and R is the value of the current sensing resistor. The value of R and the phase correction were found by calibrating the oscillator using crystals whose impedance had been measured with an impedance analyser (Hewlett Packard, HP4194A). Three different crystals were used in this calibration; a commercial metal-cased crystal, a crystal in a mounting cell made of poly-tetraflouroethylene (PTFE) and a crystal in the PTFE cell under water. The voltage, current and phase outputs of the oscillator were measured for each of the three sensors and these values were used to derive the calibration.

### 4.1.2 The Oscillator

Many oscillators have been developed which use quartz crystals as frequency standards or timing devices. In such applications the mechanical load on the crystal is minimised, usually by lightly suspending the crystal in a sealed metal can which is filled with an inert gas.
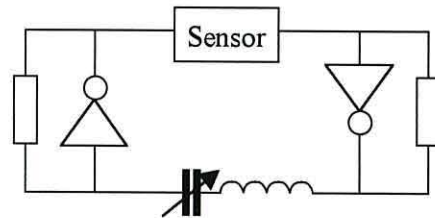
**Figure 4.2 The TTL Quartz Crystal Oscillator**

In sensing applications, however, the crystal is often required to operate with one or both faces in contact with a liquid, which imparts a significant acoustic load. Such conditions reduce the mechanical efficiency of the sensor so that conventional circuits cannot sustain oscillation and the device fails. A number of circuits have been developed to overcome this limitation and the three employed in this work are described below.

*4.1.2.1 The TTL Oscillator*

The so-called TTL oscillator is one of the earliest successful oscillators developed for operating with sensors immersed in liquid (Brukenstein 1985). The circuit is shown schematically in figure 4.2. Two transistor-transistor logic (TTL) inverters, operating in a quasi-linear mode, provide the amplification element of the oscillator. The two electrodes of the sensor are connected to the output of the first inverter and the input of the second. The output of the second inverter is connected to the input of the first by a simple filter network, which ensures that the circuit can only resonate in the region of 10 MHz where the fundamental series resonant frequency of the sensor is expected. This prevents the circuit from locking on to any other resonance.

The circuit is powered by a dedicated power supply based upon a solid state mains to 5 V d.c. converter (RS Components) This delivers a stable 5 V output at currents up to 200 mA.

This circuit was chosen for its ability to drive a sensor with one face in contact with liquid (the other being in air) but in the present application two modifications have proved to be necessary. The TTL integrated circuit was replaced by a low power Schottky device (SN74LS04N) as it gave a more stable output. Increasing the value of

the resistors in the circuit (figure 4.2) from 680 to 1500 ohm improved the stability and reliability of the circuit.

This circuit did, however, have some disadvantages; it had to be carefully tuned to produce a stable output, was very susceptible to electrical interference and had to be carefully shielded. Most importantly, it measured only the resonant frequency, giving no information about the impedance of the sensor.

In order to derive the full mechanical parameters of the sensor both the frequency shift from the unloaded state and the impedance must be measured as described in section 4.1.1.

*4.1.2.2 The Gain Controlled Oscillator*

A local company (Industrial Development Bangor) designed and constructed an oscillator, which provides voltage and current outputs and thus permits measurement of the sensor's impedance. The schematic of this circuit is shown in figure 4.3 and the full circuit diagram appears in the appendix. The circuit employs an automatic gain controlled amplifier (Elantec, EL4452C) to maintain a constant voltage at one electrode of the sensor. The other electrode is connected to ground through a sensing resistor. The voltage applied to the sensor and that developed across the sensing
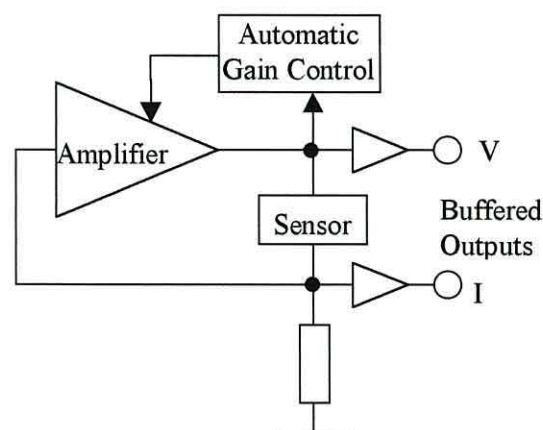


**Figure 4.3 The Gain Controlled Quartz Crystal Oscillator**

resistor are provided as buffered outputs from the circuit. These two outputs are used to derive the impedance of the sensor using equations 4.1 and 4.2.

The oscillator was designed to operate from a $\pm$ 12 volt power supply but, on testing, proved far more stable when operated from a $\pm$ 9.5 volt supply. This was supplied by a bench power supply (Farnell TOPS3D).

During the course of this work, it became apparent that, by operating the device at a constant current, oscillation could be more easily sustained under heavy loads. Accordingly, the gain controlled oscillator circuit was adapted to constant current operation.

*4.1.3.3 The Constant Current Oscillator*

The gain controlled oscillator circuit maintained the applied voltage constant and allowed the current signal, which is the feedback signal to the input of the amplifier, to decrease with increasing load. The circuit ceases to maintain oscillation once the current signal drops below a certain threshold.

In order to use the sensors with higher loads, the circuit was altered so that the automatic gain control keeps the current signal constant and allows the applied voltage to increase with increasing load. Figure 4.4 shows a schematic diagram of the adapted



**Figure 4.4 The Constant Current Quartz Crystal Oscillator**

circuit. Care must be taken with this arrangement that the output of the amplifier does not saturate and thus affect the linearity of the circuit. A 10 dB attenuator was used in line with the voltage output to prevent the signal becoming great enough to saturate the input of the vector voltmeter. The attenuator was calibrated by connecting the vector voltmeter to a signal generator, measuring the output voltage at 10 MHz, then connecting the attenuator between the instruments and repeating the measurement. This measurement was repeated for signal generator outputs from 50 to 450 mV in 50 mV steps and the mean response for the attenuator was calculated.

This circuit is capable of driving a sensor with both faces under liquid. This can be of great advantage in studies of surface adsorption since it avoids the need to seal one face of the sensor, simplifying experiment construction and doubling the sensitivity of the sensor.

### 4.1.3 The Frequency Counter

The output signal of the oscillator is measured by a frequency counter (Racal Dana, Model: 1990) which is able to give the frequency of the signal to a resolution of seven digits with a one second gate time. The accuracy of the instrument in this mode is $\pm 1$ Hz. The counter is connected to the desktop computer by a general purpose instrument bus (GPIB) interface that allows the computer to remotely control the instrument and to record the measured frequency at predetermined intervals.

### 4.1.4 The Vector Voltmeter

The buffered voltage and current outputs from the oscillator circuit are measured by a vector voltmeter (Hewlett Packard HP8405A). This instrument acts as a radio frequency voltmeter and phase meter. Measuring the amplitude of the voltage and current signals and the phase difference between them enables the complex impedance of the sensor to be calculated. The output from the phase meter and replicas of the input signals at a frequency of 20 kHz are provided via connectors at the rear of the instrument. In order to record these signals they must be converted to a digital form

that the computer can read. Accordingly, the 20 kHz signals are first converted to d.c. using an r.m.s. to d.c. converter.

### 4.1.5 The Root mean square to d.c. Converter

Root mean square (r.m.s.) to d.c. conversion has been achieved using integrated circuits (Analog Devices, AD536AJQ). Each integrated circuit (i.c.) is capable of computing the true r.m.s. value for one channel at an accuracy of $\pm 5$ mV $\pm 0.5\%$ of the reading. The i.c. is laser-trimmed at the wafer level for input and output offset, positive and negative wave form symmetry (d.c. reversal error), and full-scale accuracy at 7 V r.m.s.. As a result, no external trims are required to achieve the rated accuracy of the unit. The only external component required by the i.c. is a capacitor that sets the averaging time and thus determines the amount of ripple on the output signal. The i.c. can operate from single or dual supplies and in this application shares the $\pm 9.5$ volt power supply with the oscillator bringing the total current drawn to 68 mA, which is well within the power supply's 1 A capability.

The d.c. output is directly proportional to the a.c. input up to 5 kHz, at 20 kHz there will be some dependence upon frequency. This can be neglected because both channels, operating at the same frequency, will be subject to the same scaling error which will be eliminated as one measurement is divided by the other in the calculation of the impedance of the sensor. The two d.c. signals along with the phasemeter output are converted into a digital form using an analogue to digital converter (ADC) in order to be read by the computer.

### 4.1.6 The Analogue to Digital Converter

A self contained high-accuracy analogue to digital converter (Pico Technologies, ADC-16) is connected to the desktop computer. This device provides 8 measurement channels at a resolution of 16 bits. It is connected to the serial port of the computer and thus has the advantage of not occupying an expansion slot in the computer. The sampling rate depends on the applied voltage but the worst-case conversion time is 657 ms which is shorter than the gate time of the frequency counter.

### 4.1.7 The Mains Power Supply

Particular attention had to be paid to the quality of the mains power supply. Both the oscillator and frequency counter were very susceptible to mains borne noise. It was observed that switching mains loads such as other laboratory equipment on or off caused several false triggers of the counter and resulted in a frequency output a few hertz above the true value. Two measures were used to overcome this problem.

The mains supply was connected to a constant voltage transformer (Advance Industrial Electronics CVN 750/A Volstat) designed to maintain a constant output voltage of 240 volts with an input that can range between 190 and 260 volts. In addition a mains conditioner (Micropac CT150) was used to further clean the output of the Volstat transformer. The combination of these two measures produced a quality of mains supply which was more than adequate for the instruments.

### 4.1.8 The Controlled Temperature Enclosure

Quartz crystals are sensitive to temperature and experiments which continue overnight are affected by a variation in the temperature of the laboratory. To minimise changes in temperature a temperature-controlled enclosure was built consisting of an acrylic resin box large enough to hold the oscillator, the quartz crystal cell, a thermocouple and a light bulb. A temperature controller (Comark 2501) was used to measure the response of the thermocouple and produced a square wave signal with a duty cycle inversely proportional to the temperature. This signal was amplified and used to power a light bulb which acted as a heat source. As the temperature falls the duty cycle increases keeping the light bulb on longer and heating the enclosure. In this way the temperature can be kept constant to within 0.5 °C.
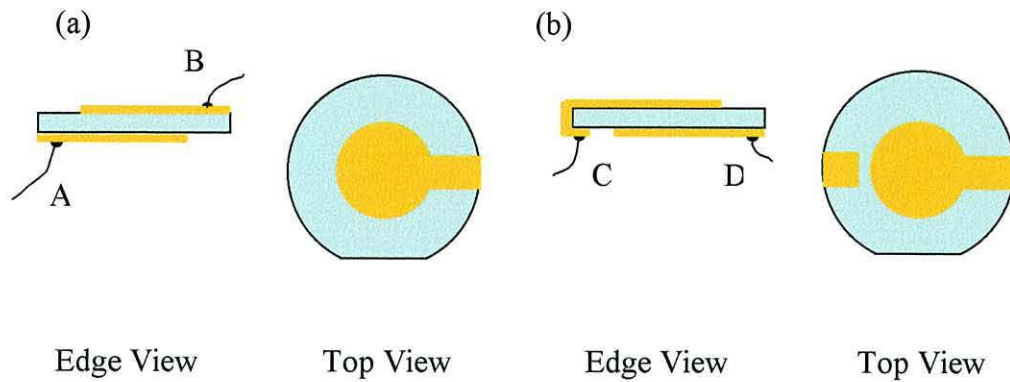
**Figure 4.5 The Quartz Crystal Sensor** (not to scale)

(a) Standard keyhole-shaped electrodes, electrical connections made to tabs A and B.
(b) Wrap-around electrodes, electrical connections made to tabs C and D leaving the top face unencumbered.

## *4.2 The Experimental Apparatus*

### 4.2.1 The Quartz Crystal

The sensors used in this work are 10 MHz AT-cut quartz crystals (IQD Ltd) which are circular and have a diameter of 8.25 mm and a thickness of 0.16 mm. One edge is slightly flattened to indicate the X-direction of the crystal (figure 4.5). Because of the small size and the fragility of the crystals great care must be taken when manipulating them. For this reason all hardware was designed with ease of handling in mind.

Electrodes were vacuum-deposited onto both sides of sensor through molybdenum foil masks. The acoustically active area of the crystal is defined by the region where the electrodes overlap producing the required electric field, this is where the shear waves are generated and where the sensor is most sensitive. Each electrode consists of a layer of gold 1000 $\square$ thick deposited over a 50 $\square$ layer of chromium. The chromium is interposed between the gold and the quartz because gold does not adhere well to quartz.

Electrical connections were made to gold tabs (A and B, figure 4.5a) which form a part of each electrode. In early experiments gold wire, 25 μm in diameter, was bonded to the tab by ultrasonic welding. Investigation showed that the best bonds were achieved

by placing the sensor on a heated stage at 130°C and applying ultrasonic power for 200 ms. The power output of the welding machine (Westbond, 7400B) was set to an optimum setting but the bonding process remained unreliable with several attempts being required to produce a good bond. Although excellent electrically the bonds were of limited mechanical strength and easily damaged. The bonding process proved too time-consuming and later experimental designs used silver conductive paint (RS Components) to fix the connections to the sensor. This proved to be easier and more reliable.

In tribology experiments it is essential that the electrode which acts as a friction surface be unencumbered by the electrical connection. Evaporation of gold onto the edge of the sensor allows the electrical connection to be extended from one face to the other of the crystal as illustrated in figure 4.5b. Both connections can now be made on the bottom face of the crystal (points C and D in figure 4.5b) leaving the top face unencumbered.

### 4.2.2 The Quartz Sensor Cells

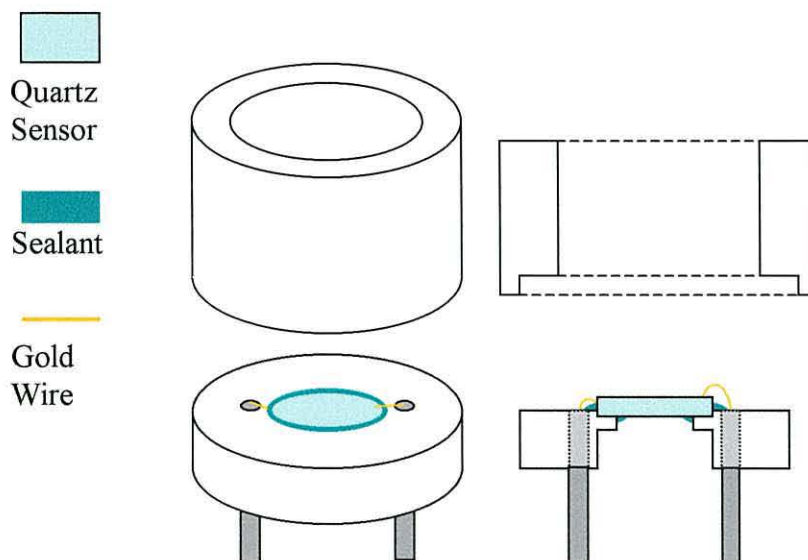During the course of this work a number of cells have been developed for mounting



**Figure 4.6 Cell for mounting the quartz sensor**

the sensor. The example shown in figure 4.6 displays the essential features of all of them. The cells are made of PTFE since it is chemically inert and is easy to clean. The sensors are required to operate with one face in contact with liquid and one in contact with air. This is achieved by sealing the edge of the sensor with a silicone rubber compound (RS Components). The compound causes an acoustic load on the sensor and must therefore be kept to the minimum necessary to produce a good seal and confined to the edges of the sensor.

At first the cell employed long lengths of 25 μm gold wire which proved to be too vulnerable for service. An improved cell, illustrated in figure 4.7, was designed where connection to the oscillator is made by 2 mm plugs and only short pieces of gold wire are needed from the sensor to the top of the plugs making the assembly process much easier. These cells can be fitted to either a large cylinder or a small tray in order to contain the fluids used in an experiment. When the sensor is under significant depth of liquid a compression wave spoiler must be used otherwise small changes in the depth of liquid change the compression wave resonance and affect the shear wave measurements as described in section 3.3.2.

The quartz sensor tribometer placed new demands upon the cell design. The sensor had to stand proud of the cell so that the sealant would not affect the friction measurements and the cell had to be driven by a motor in one direction. The cell shown
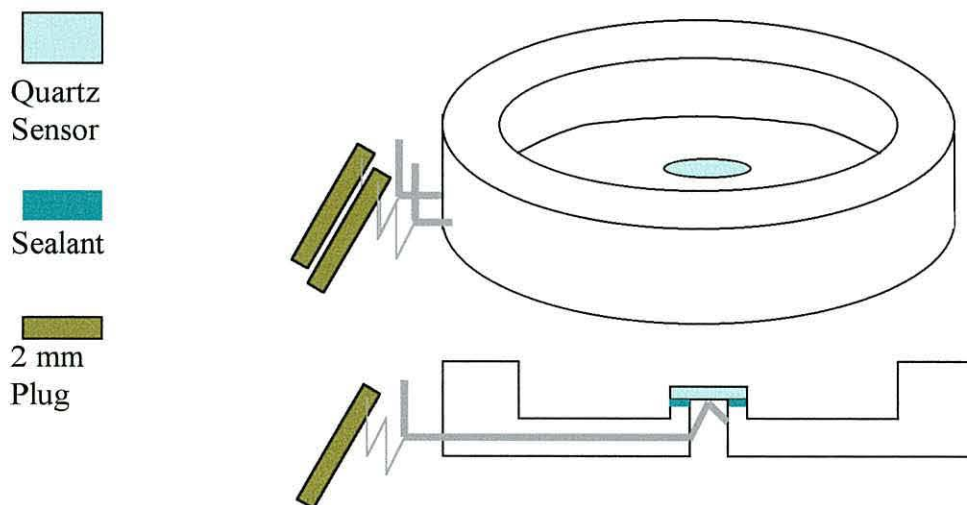


Quartz
Sensor

Sealant

2 mm
Plug

**Figure 4.7 Sensor cell for use with tribometer**

in figure 4.7 was designed for use with the tribometer and was in the form of a tray, thus allowing friction experiments to take place under liquid. A tray of equal volume was placed under the cell in order to catch any liquid and protect the expensive moving stage should the sealant around the sensor fail. A two-part epoxy adhesive (Araldite) replaced the silicone rubber compound as the sealant because it is stiffer and easier to apply. Connection to the sensor electrodes was made by two steel wires which passed through the base of the cell from its outer edge to its centre where they came close to the electrodes. Silver conductive paint was used to bridge the small gap to make the final connection. At the outer end the wires were soldered to light-weight coiled copper wires which were connected to the oscillator with 2 mm plugs. Electrical interference was minimised by placing the oscillator as close to the cell as possible.

### 4.2.3 The Quartz Sensor Tribometer

The quartz sensor tribometer combines the function of a tribometer with a quartz crystal shear wave sensor. A schematic diagram of the instrument is shown in figure 4.8. The tribometer consists of a light aluminium alloy beam, B, supported on a frictionless pivot, P. On one end of the beam there is an adjustable counter-weight, C, on the other a friction probe. The friction probe, shown in figure 4.9, is mounted on two parallel leaf springs which allow it to move freely in a direction parallel to the

B Beam
P Frictionless pivot
C Counter-weight
M Applied weight
Q Matching crystal
S Sensor cell (Figure 4.7)

Motorised stage

Micrometer
controlled platform
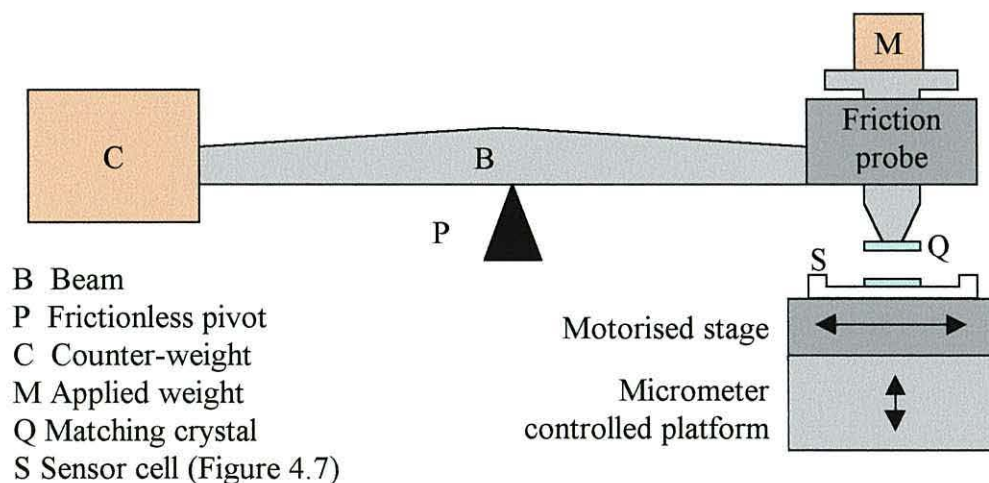
**Figure 4.8 The quartz sensor tribometer**
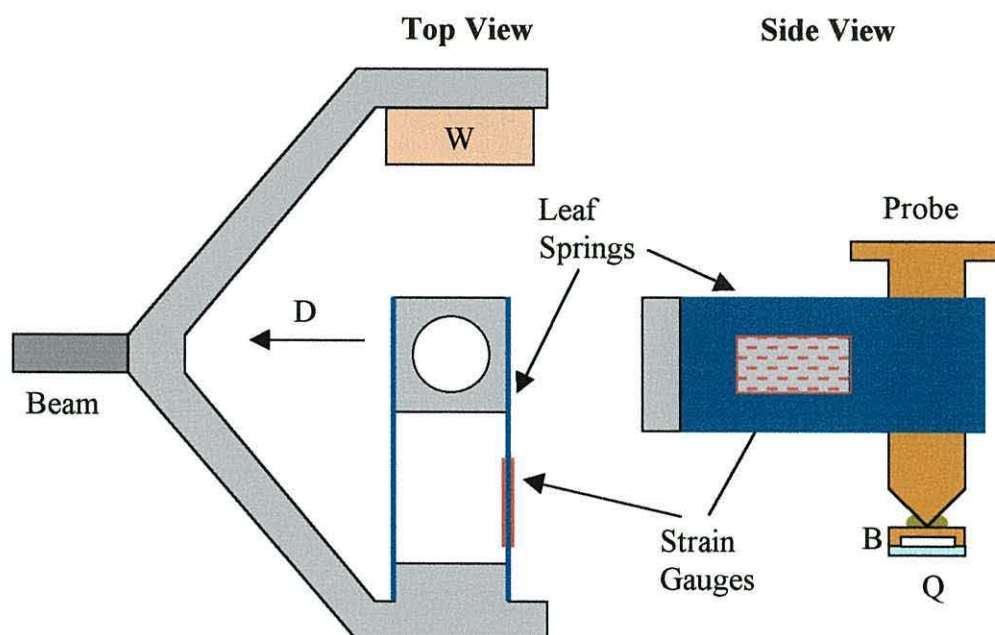
**Figure 4.9 The Friction Probe**

W Counter-weight          Q Matching quartz crystal
D Direction of travel     B Brass cup, secured by epoxy adhesive

longest axis of the beam. A matching crystal is fixed to the end of the friction probe and makes contact with the quartz crystal sensor to form the friction interface.

The tribometer used in this work is based upon a machine in use at Unilever Research Port Sunlight. In this design the lower friction surface is a quartz shear wave sensor which enables shear wave data to be collected simultaneously with friction data.

In addition to monitoring changes in the viscoelastic properties of the sheared layer, the quartz crystal tribometer provides three important facilities. Firstly, the substrate can be moved over precisely defined distances at precisely controlled speeds. Secondly, the normal force acting upon the friction probe can be precisely controlled and, thirdly, the resulting friction force acting upon the friction probe can be accurately measured thus permitting the friction coefficient for the two surfaces to be calculated. The static friction coefficient can be observed by operating at low speed.

*Sensor Cell*

In order to allow the friction surfaces to be immersed in liquid the sensor is sealed into the PTFE cell described in section 4.2.2 and the sensor electrodes are connected to the gain controlled oscillator by fine copper wires that do not significantly impede the movement of the mechanical system.

*Motorised Stage*

Movement of the quartz sensor is achieved by bolting the PTFE tray to a motorised stage (Phisik Instrumente M125.11) which has a travel of about 50 mm and can move at speeds up to 1 mm s$^{-1}$. It is equipped with a digital encoder to permit feedback control with a positional resolution of 8.5 nm. The stage is linked to a controlling microcomputer by a dedicated interface board (Phisik Instrumente, C842). This permits simultaneous measurement of the quartz sensor parameters and the friction force to be made while the probe is operating at a specified position or velocity. The motorised stage is mounted on a micrometer controlled platform which allows it to be raised or lowered manually in order to bring the friction surfaces into contact.

*Beam*

Control of the normal force is achieved using a beam made of aluminium with slots machined out to minimise its weight. The arm is mounted on a 8 mm diameter flexural pivot (Allied Bendix Aerospace) with a torsional spring rate of 0.235 Kg cm rad$^{-1}$ and a load capacity of 6.35 Kg. Using this type of pivot makes the machine structurally robust and therefore easier to use than other types of low-friction pivots such as knife edges. The weight of the beam and friction probe have been kept within the load capacity of the flexural pivot and the angle through which the beam is allowed to move is restricted by adjustable stops which are also used to immobilise the beam while an experiment is prepared. The friction probe is mounted on one end of the arm and the counter weight, C in figure 4.8, on the other.

*The Friction Probe*

The friction probe, illustrated in figure 4.9, is attached to the arm by two leaf springs which are made of shim steel. The springs are rigid in the normal direction but are bent in the direction of motion by the friction force. Strain gauges are glued to the front and back of one spring. The stiffness of the spring is found by experiment and, along with the measured strain in the spring, is used to calculate the friction force. In order to minimise mechanical interference connections to the strain gauges are made by means of very fine (125 μm diameter) copper wire.

*Strain Gauges*

The strain gauges are wired in a full bridge configuration with the four cells made up by two dual strain gauges glued opposite each other on the front and back surfaces of one spring. A Transducer amplifier (Fylde Electronic Laboratories Ltd, FE-379-TA) provides a stabilised d.c. power supply to the bridge and measures the output. The ADC is used to interface the amplifier to the computer. The output is calibrated in the following manner.

With the beam level the amplifier is set to zero using its auto-zero function. The beam is now carefully removed from its mounting and clamped upright, in this position the weight of the friction probe puts a strain on the leaf springs and the output of the strain gauge is measured. Weights are added to the friction probe up to 20 g in steps of 2 g. The output of the strain gauge is measured at each step and plotted against weight. The experiment is repeated four times and the results are averaged to give a scaling factor for subsequent measurements.

*Operating Method*

To ensure that the applied force operates exactly normally to the friction surface the counter-weight C, in figure 4.8 is carefully adjusted so that the arm balances. The quartz sensor is then raised by the micrometer controlled platform until it is just in contact with the probe. A normal force is then applied by placing a known weight, M in figure 4.8, on the friction probe. The substrate is now moved backwards or forwards

at a constant speed in the direction of motion labelled D in figure 4.9. The consequent displacement of the leaf springs is measured and used to calculate the friction force developed at the interface.

## *4.3 The Software*

Because much of this work is concerned with the way in which the output of the quartz crystal sensor changes with time, it was essential to develop software which enabled efficient recording of the measurements. The computer is interfaced with the frequency counter using a general purpose instrument bus (GPIB) interface and the analogue-to-digital converter using the built-in serial interface (RS232). The software performs two functions; it initialises the instruments and records the measured data for off-line analysis. When the tribometer was constructed new software was developed which enabled the computer to control the motorised stage and to record the output of the strain gauge along with the quartz sensor measurements.

### 4.3.1 The QBASIC Program

At the outset of this work a program for recording frequency data existed which had been written in the Microsoft QBASIC programming language. This program took measurements from the frequency counter at specified time intervals. The time at which each measurement was taken and the recorded frequency were stored on the computer hard disk. This program was used as a basis for the software but a number of shortcomings were dealt with in order to make the most efficient use of the data available.

The first shortcoming to be addressed was the precision of the stored data. The program treated the frequency data as QBASIC single precision floating point data. This meant that only six digits were recorded, the last having a significance of 10 Hz. The output of the frequency counter has a resolution of 1 Hz and changing the data type to double precision floating point allowed the full measurement to be recorded.

Since it is unsatisfactory to leave an experiment for long periods without monitoring its progress a simple graph plotting routine was added to the program. This displayed a

trace of the frequency against time and updated every time a measurement was made; rescaling the axis when necessary to keep data on the computer screen.

Functionality was added for initialising the analogue to digital converter and thus measuring the vector voltmeter output. The magnitude and phase angle of the sensor impedance are derived from these measurements using equations 4.1 and 4.2. The resonance frequency, sensor impedance and the phase angle of the impedance are stored in three separate files and filename extensions FRQ, ZMN and PHS are appended to the filename specified by the user to distinguish them. Each file contains two columns, the first being the time of each measurement in seconds and the second the measurement parameter.

The QBASIC program is interpreted from BASIC code as it runs making very inefficient use of the computer. Only very low level graphics instructions are available so that a large amount of code was required to achieve the real time plotting. These two undesirable features made it necessary to use a more advanced programming language to further develop the software and Microsoft Visual Basic was adopted for this purpose.

### 4.3.2 The Visual Basic Program

The Visual Basic programming language was employed because, being similar to QBASIC, it was possible to re-use much of the QBASIC code. Visual Basic has a number of advantages, particularly that the program is compiled rather than interpreted and thus operates much faster. The Visual Basic programming environment gives access to many higher level instructions which make writing and understanding the code easier. The environment also provides access to Microsoft Windows controls such as text boxes and command buttons which can be used to make the user interface of the software more sophisticated and easier to use.

The code was split into modules in order to make it easier to extend and maintain. Portions of code were grouped together according to their function. One core module, known as the main module, controlled the main functions of the whole program.
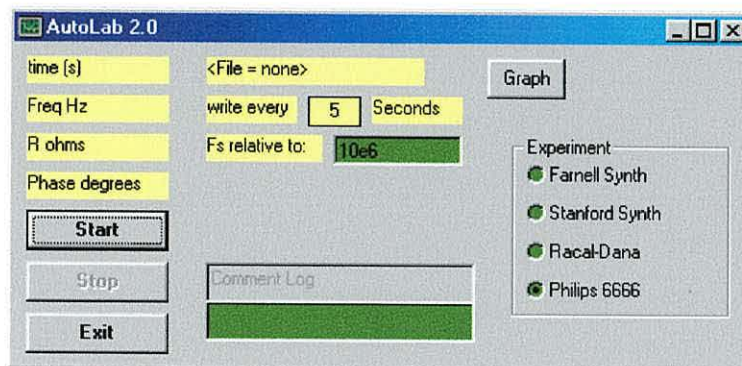
**Figure 4.10 Main Panel of Visual Basic Program**

*Main Module*

The main module includes the main panel, illustrated in figure 4.10, which the operator uses to control the software. The radio buttons on the right hand side of this panel are used to select between different sets of experimental equipment. The controls in the centre are all user inputs. The label at the top gives the name of the file to which data is written. The text box below it contains the time interval between measurements, this can be changed during an experiment by typing a new value into the box. The text box below this allows the user to enter a reference frequency which is subtracted from the absolute frequency measurements. This means that the difference between the reference frequency and the absolute frequency measurement is recorded. Typing zero in this box causes the absolute frequency to be recorded. The text box at the bottom of the panel facilitates the recording of comments during an experiment. When a comment is typed in the box it is written to a log file along with the time. When the data is analysed off-line these comments can help to interpret features in the data.

Each time a measurement is made the four labels in the top left of the panel are updated to show the time and the value each parameter.

Four command buttons appear on the panel. The button labelled "Graph" displays a plot of the data which is updated in real time. The buttons in the bottom left start and stop measurements and exit the program. The "Stop" button is disabled while the program is idle but enabled once data taking starts. The "Start" and "Exit" buttons are disabled during data taking and enabled again once it is stopped.

An outline of the algorithm by which data is recorded is shown in figure 4.11 and a complete listing of the code appears in the appendix. The program begins by initialising the instruments and then taking the first set of frequency and impedance data. The variable `No_of_points` is set to the value 1 (its use becomes apparent later in the listing). The variable `Start_time` is set to the value of the computers internal clock, the value of this variable is subtracted from the time of the measurements so that the time recorded with the data is the time since recording started. The program goes through the `While` loop once for each measurement, the loop begins by subtracting the value of `Start_time` from the value of the computers clock to give the time since the beginning of the experiment. The value of each measured parameter is divided by the value of the variable `No_of_points` and the results are output to the labels on the main panel, the files on the hard disk and the real time graphs.

```
Set up instruments and take first set of
measurements
No_of_points = 1

Start_time = Now()

─While(Stop button has not been clicked)

      Record_time = Now() - Start_time
      Divide each parameter by No_of_points

      Display data on labels
      Write data to disk
      Display data on graphs

      Next_record_time = Time_interval + Now()

      Set all parameters to zero
       No_of_points = 0

      ┌Do
            Add a measurement to each parameter
            No_of_points = No_of_points + 1
      └Loop While (Next_record_time > Now() )

─Wend
```

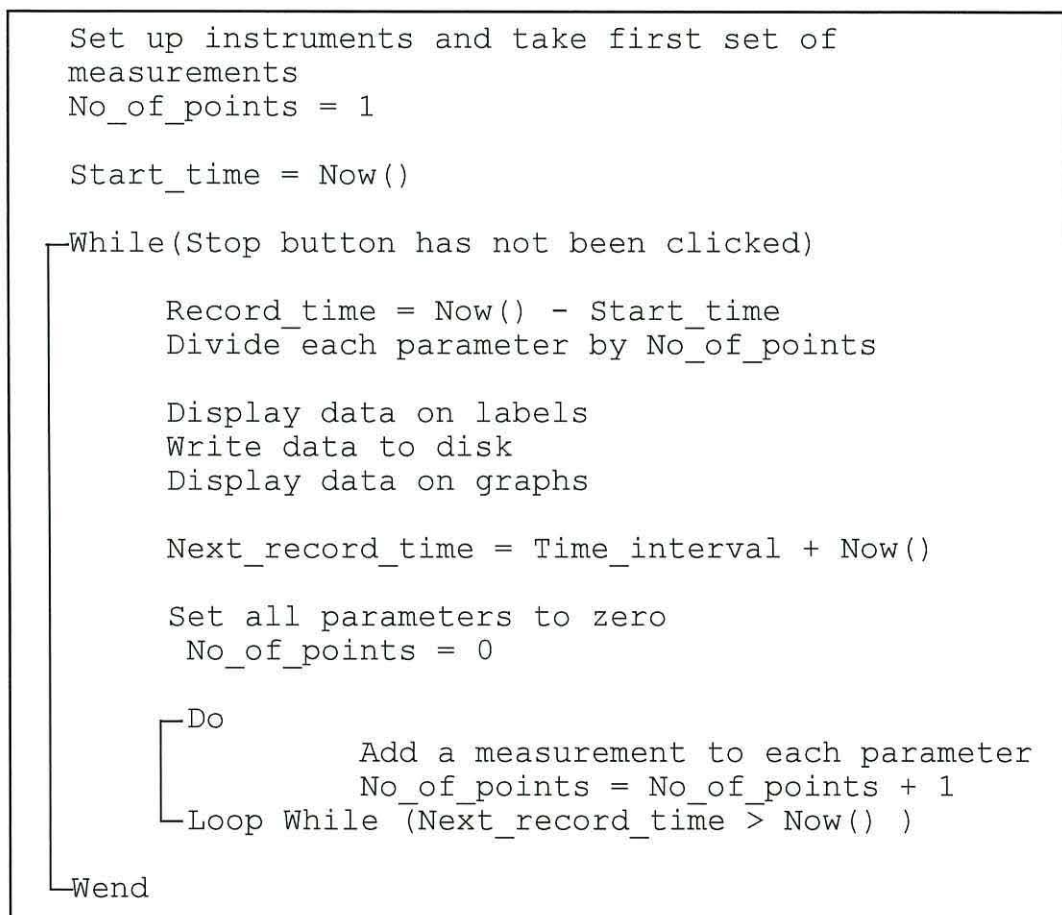**Figure 4.11 Outline of the Visual Basic program algorithm**

Immediately after the data is output the time at which the next measurements must be recorded, `Next_record_time`, is calculated by adding the specified time interval to the current value of the computer's clock. All measured parameters and the variable `No_of_points` are now set to zero and the program goes into the `Do` loop.

In programming a `Do` loop differs from a `While` loop in that the test which determines whether to repeat the loop or continue with the rest of the program is situated after the body of the loop. When executing a `While` loop it is possible that the test will prove false the first time it is tried and, if this is the case, the program will continue without ever executing the instructions in the body of the loop. With a `Do` loop the instructions in the loop are executed at least once before the test is made. In the case of this algorithm the first time the instructions in the `Do` loop are executed a measurement is made, the results are added to the parameter (which started as zero) and the value 1 is added to `No_of_points` (which also started as zero). The program now checks to see if the time interval for the next measurement is complete; if it is then the `Do` loop terminates and control passes to the top of the `While` loop. If the time interval is not complete then control passes back to the top of the `Do` loop and the instructions in the loop are repeated, each parameter is now equal to the sum of the two measurements and `No_of_points` is equal to 2. The program continues to execute the `Do` loop until the time interval is complete. When time is up control passes to the top of the while loop where each parameter is divided by `No_of_points` to give an average of the measurements taken during that time interval. This means that where the time interval between measurements is large enough the computer takes more than one measurement and records an average. The longer the time interval the more measurements are taken and averaged for each point. Conversely, if the time interval is shorter than the time it takes to complete a measurement, the computer will complete the measurement anyway even though the recorded time intervals will be longer than specified.

*File Module*

This module includes a panel which is displayed when the computer's mouse is clicked over the file name label on the main panel. The panel displays lists of disk drives, directories and files in order to assist the user in selecting a file name. If the user chooses a file which already exists, the program asks the user for confirmation before deleting the old file. Once the file name has been chosen the panel is hidden. This module also contains the code which writes the data to the file.

*Real Time Plotting*

The panel associated with this module is displayed when the "Graph" button on the main panel is clicked and is hidden by clicking the button labelled "Close". This panel is illustrated in figure 4.12. Three graphs are plotted, one displaying the frequency and the other two displaying the magnitude and phase angle of the impedance. The three icons to the left of the "Close" button are used to select which of the three graphs appears in the main window of the panel. Four text boxes at the edges of the window
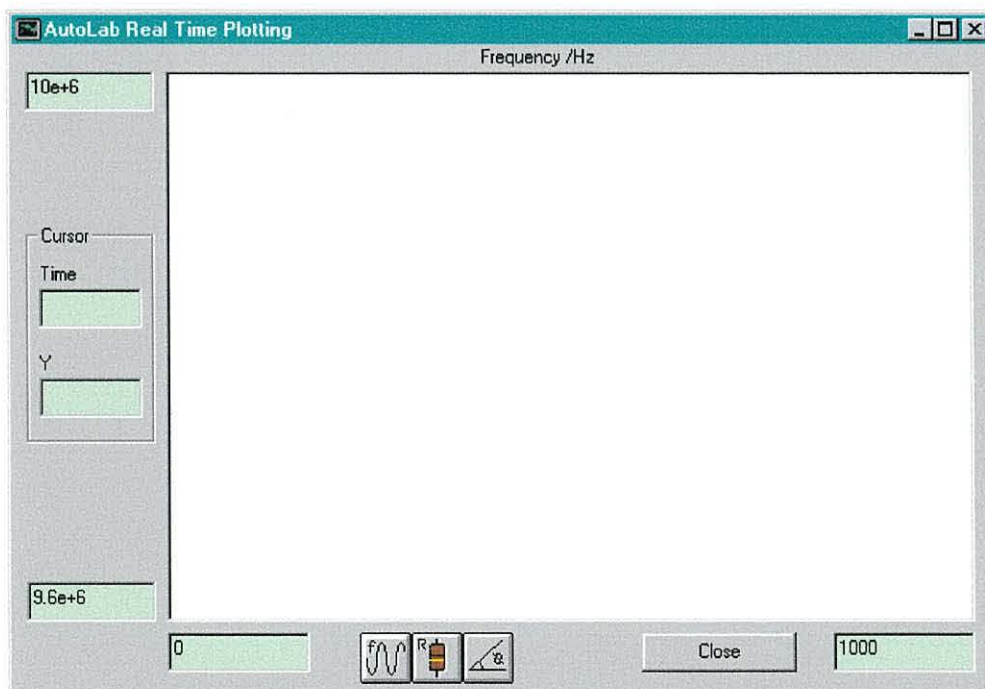


**Figure 4.12 Real time graph plotting module**

give the limits of the axis. Typing new values into these boxes causes the graph to be rescaled, the boxes on the y-axis only rescale the graph being viewed while the boxes on the time axis rescale all three graphs. When the mouse pointer is moved over the main window it changes into a crosshair and its co-ordinates are displayed on the left hand side of the window.

*Measurement Module*

This module contains the code which actually performs the measurements. As well as the sensor parameters the air temperature in the laboratory can be measured using a chart recorder output from the temperature controller which is connected to a spare input of the analogue to digital converter.

The first time a measurement is required the instruments are set to the correct mode and resolution before the measurement is taken. The method of acquiring the measurement varies according to the set of experimental equipment which is selected on the main panel (figure 4.10). The "Racal Dana" option refers to the system described in section 4.1. The "Philips 6666" option refers to a duplicate of this system which differs only in the use of an alternative model of frequency counter. The model must be selected because the two use different GPIB commands and the program must use the appropriate set for each instrument.

Two other modules connected with the measurement module contain code which provides access to software drivers for the GPIB interface and the analogue to digital converter. The GPIB interface and the analogue to digital converter are both supplied with drivers in the Windows dynamically linked library format which contain routines for interfacing the instruments. The main program does not contain these routines but instead contains links to the library files from which individual routines are loaded by the Windows system when they are required. These driver files provide faster and more efficient access to the instruments.

### 4.3.3 The HP VEE Program

When the tribometer was designed a copy of HP-VEE 3.0, a rapid development programming environment was kindly donated by Hewlett Packard. This system is produced specifically for instrumentation applications and is easy to interface to instruments. A program is built up by drawing flow charts on the computer display rather than writing lines of code. Programming constructs, instruments and displays are all represented as boxes and the movement of data between them by lines.

A modular approach is facilitated by grouping several boxes together into one single box which is known as a user object. A user object can in turn contain other user objects and in this way a set of basic building block modules can be developed. These modules can be quickly rearranged as new experiments and operating procedures are
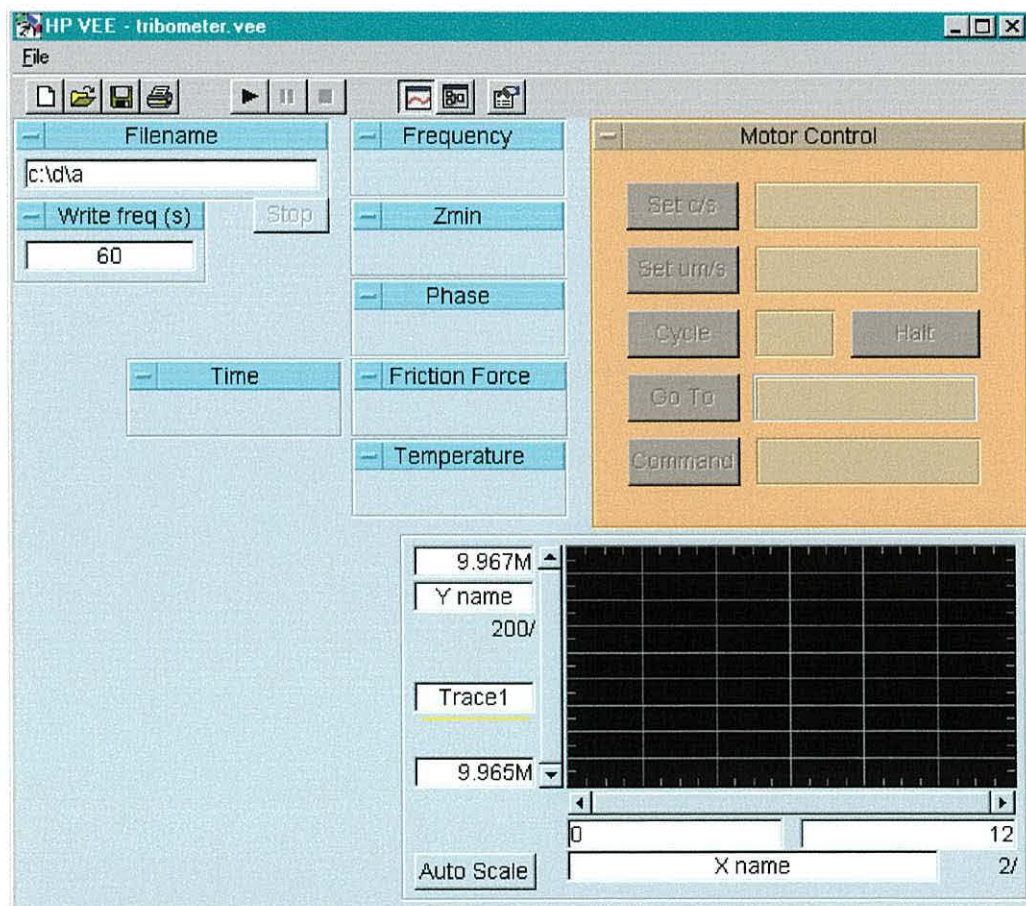


**Figure 4.13 HP-VEE program for controlling the tribometer**

developed for the instrument. Taking advantage of this fact, the program that was developed for control of the tribometer was changed a number of times as different experiments were carried out. The most useful variant is described here.

The panel view as seen by the user is illustrated in figure 4.13. At the top left of the panel are two text boxes, the top one enables the user to specify a file name for recording data and the second box specifies the time interval between measurements. Each time a measurement is taken displays in the centre of the panel are updated to show the measured parameters and the time of the measurement. A graphical display of the recorded frequency is also provided. To the right of the panel is the motor control module. This provides the user with functions to set the velocity of the stage, to move the stage to a specified position at the specified velocity and to continually move the stage backwards and forwards a specified distance around a predefined zero point.

*Measurement Program*

An outline of the measurement program is illustrated in figure 4.14. The program begins by importing the Windows dynamic link library required for interfacing the
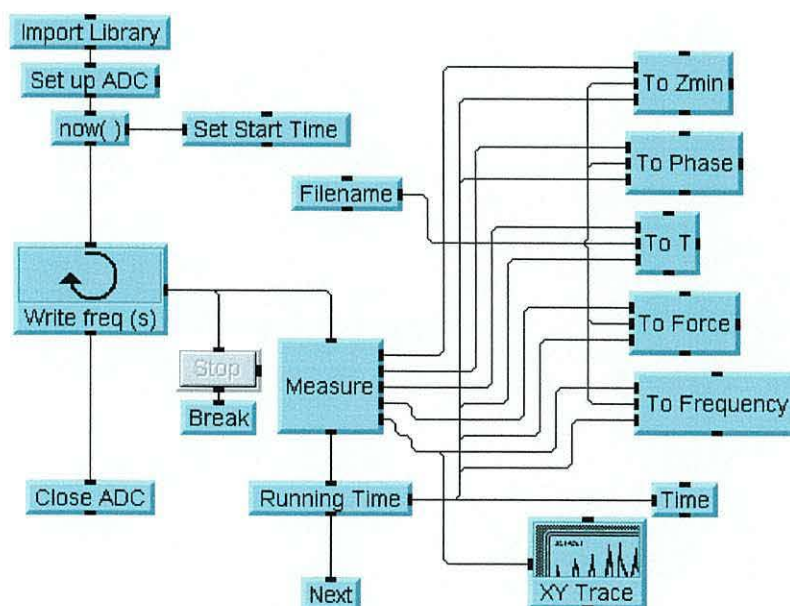


**Figure 4.14 Outline of the HP-VEE program**

analogue-to-digital converter (ADC) which it then initialises. Next the value of the computers internal clock is recorded as the start time so that the time since the experiment started can be calculated for each measurement. The next item is an object which triggers the thread attached to its right hand terminal at regular intervals until the break is executed. This object appears on the panel view as the text box in which the specified time interval is entered. The break object is executed when the stop button is pressed, until then the measure object is executed at the specified intervals. The measure object is a user object which contains the code used to obtain data from the instruments. After the measurement is taken the running time object calculates the time since the experiment began. The data, filename and time are all passed to five output objects which each output one of the parameters to the displays on the panel and the files on the hard disk.

*Modules in the Measurement Program*

Figure 4.15 illustrates the three most important user objects in the measurement program. The measure object is the object which obtains data from the instruments and, where necessary, converts the data into the required parameters. The first item in the object module sends a request for data to the frequency counter. The second item acquires data from the analogue to digital converter, the sensor impedance is calculated as described in section 4.1.1 and the output of the strain gauge amplifier is
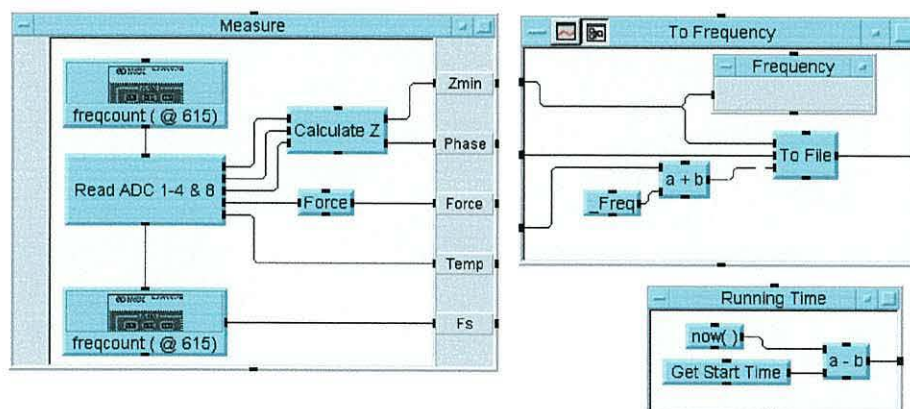


**Figure 4.15 Contents of key objects in the HP-VEE Program**

scaled according to the calibration described in section 4.2.3. The final item receives the data from the frequency counter that the first item requested.

The running time module calculates the time since the experiment started by subtracting the start time from the current value of the computers clock. The output object contains a display which appears on the main panel, a to file object is also included which appends the time and measurement parameter to a file on the hard disk. In the case of the to frequency object the string "_Freq" is added to the end of the filename, the other output objects contain similar strings so that five separate files are created each containing one of the five parameters.

*The Motor Control Panel*

The motor control panel appears in the top right of the main panel view in figure 4.13. This panel provides functionality for setting the speed of the motorised stage in either micrometers per second (um/s) or encoder counts per second (c/s). The stage can be directed to cycle backwards and forwards continuously at the specified speed around a home position or sent to a given position. The panel also provides the facility for the user to enter certain low level command strings into instructions for the controller

The HP-VEE program accesses the motor controller using a Windows dynamic link library file which is supplied with the controller. This library file contains a function which translates low level command strings into instructions for the controller.

# 5 Experimental Results

## *5.1 Free Fall Experiments*

The onset of boundary lubrication occurs when the liquid layer between the surfaces breaks down or is compressed to a layer only a few molecules thick. In the following experiments a liquid sample is placed between two surfaces, the lower surface is fixed while the upper surface is free to fall compressing the liquid. This process is referred to as free fall. The experiments were designed to see if the quartz sensor could detect this process.

### 5.1.1 Shear Wave Studies

The sensor crystal, S in figure 5.1, is mounted in a cell, P, made of PTFE and is sealed around its edges so that the lower face of the sensor is maintained in air. The liquid sample, L, covers the top face of the sensor and a second crystal, C, is placed on top of the sensor in order to squeeze the sample. Crystal C is not electrically connected but is identical to the sensor crystal and thus forms a matched acoustic load. A 1 g weight, W, is placed on top of the second crystal and provides the normal load that squeezes the liquid sample. A small spacer placed between the weight and the crystal maintains an air gap over the active region of the top crystal so that the weight itself does not directly contribute to the acoustic load. A measured volume of the liquid sample is delivered by a micropipette; a liquid droplet of 4 µl produces an even layer with thickness of around 75 µm between the surfaces of the quartz crystals. It is essential

W Weight
C  Matching Crystal
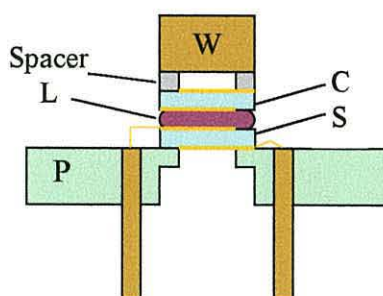L  Liquid Sample
S  Quartz Sensor
P  Mounting Cell



**Figure 5.1 Arrangement of a free fall experiment using a quartz sensor as the lower surface**

that the crystal surfaces be as clean as possible before an experiment. This is achieved by wiping them with cotton buds soaked in iso-propanol and then rinsing with iso-propanol.

The free fall process was first investigated using ultra-pure water as the liquid sample. A typical result is shown in figure 5.2, this follows a well-defined pattern. At point A a volume of 4 µl of water was placed on a dry uncovered sensor, the series resonant frequency drops in response to this acoustic load. At point B, the top crystal, washer and weight were positioned, the frequency dropped further to about 2.5 kHz below that of a dry crystal as the top crystal squeezes the water droplet and causes it to spread over the whole sensor surface. After a few minutes the frequency began to return to the value expected for a dry crystal, following a curve which proved to be characteristic of all these experiments. At point C, the frequency was within a few hertz of point A and, when the top crystal was lifted, the surfaces were observed to be dry. This observation supports the theory described in section 3.3.4 that a second crystal of thickness close to that of the sensor has an acoustic load of nearly zero. It is also possible, however, that the two crystals are separated by dust particles, liquid droplets or asperities of the gold surface in such a way that even when the liquid layer
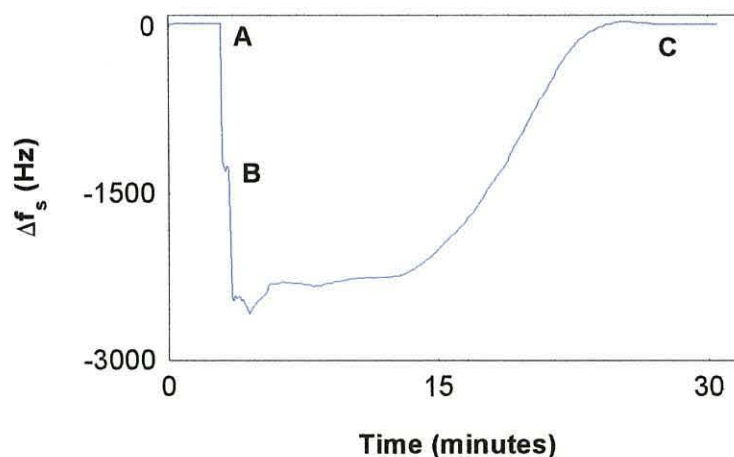


**Figure 5.2 Shear response to free fall in water**

A Water sample placed on sensor, B Matching crystal in place,
C End of free fall.

has thinned to nothing there is very little propagation of the shear wave to the top crystal.

Having established the pattern with water, a sample of a commercial lubricant, supplied by Unilever Research, was examined. Results from this, illustrated in figure 5.3, differ from those of water in two ways. The lower part of the curve had oscillations superimposed upon it. These oscillations increased in magnitude until, after one particularly large downward spike, the curve became smooth. Oscillations of this type

(a)



(b)
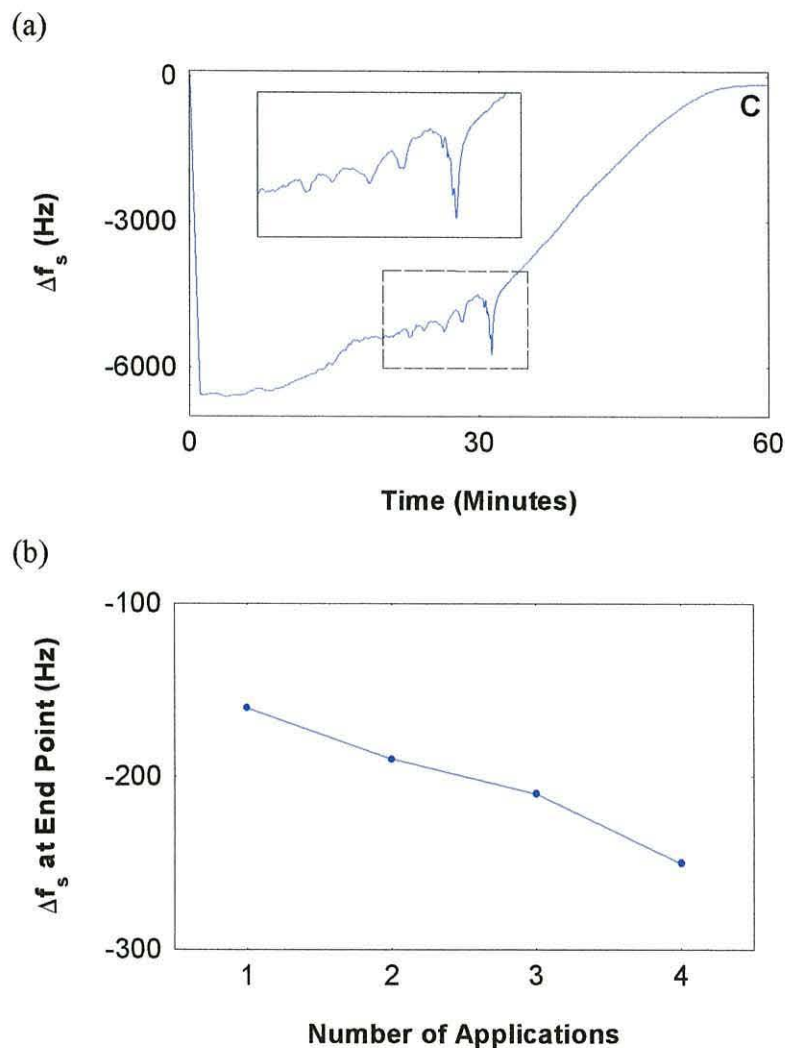


**Figure 5.3 Shear response to free fall in lubricant**

(a) Shear wave record for compression of the lubricant.
    Insert: Close up of oscillations on the curve.
(b) The end points, C, of successive experiments

have been shown to result from the presence of compression waves (Reddy 1998). Compression waves, described in section 3.3.2, are generated by the crystal and propagated through the acoustic load. They are efficiently reflected at the load-air boundary and return to impinge on the sensor giving rise to an additional acoustic load. Changes in the total path length for compression waves give rise to an oscillatory change in acoustic load with a period which corresponds to the time taken for the path length to change by $\lambda/2$ where $\lambda$ is the wavelength of the compression wave. Thus knowing the wavelength of compression waves, we can infer the speed of descent of the top crystal from the measurement of the period of oscillation. The speed of compression waves in water is 1496.7 ms$^{-1}$ so, at 10 MHz the wavelength is 146.3 $\mu$m. The resonance should go through repetitive cycles as the distance between the crystals goes through successive half wavelengths. The number of oscillations observed in figure 5.3a implies that the top crystal falls through a distance of not less than 350 $\mu$m. Experiments using an AFM and a laser profilometer, however, indicated much less movement, furthermore the 4 $\mu$l drop of liquid gives an initial layer thickness of no more than 75 $\mu$m. Thus the oscillations are unlikely to be the result of compression waves and a more realistic interpretation is that they are due to shear wave resonances. The shear wave propagation velocity in water is 15 m s$^{-1}$ so, assuming the same velocity in the lubricant, the wavelength at 10 MHz is 1.47 $\mu$m. Dividing the half wavelength by the average period of an oscillation gives a rate of descent for the top crystal of $1.0 \times 10^{-8}$ m s$^{-1}$.

As the application of lubricant was repeated, each endpoint, while close to that expected for air loading, was a few hertz lower than the previous one. The end points for four successive applications are illustrated in figure 5.3b. It appears likely that a residual layer of the lubricant was adsorbed on the crystal surface and that this layer is extended with each application. The first of the endpoints represents a mass loading of $1.41 \times 10^{-5}$ kg m$^{-2}$, since nothing is known about the molecular mass and packing density of the lubricant molecules it is not possible to say how many layers this corresponds to. At the end of the fourth application the mass loading is $2.20 \times 10^{-5}$ kg m$^{-2}$.

## 5 Results

In order to validate the results of these experiments it is necessary to show that the shear waves generated by the sensor do not affect the process. To this end a switch was installed in the DC power supply to the oscillator. The oscillator was switched off for five to fifteen minute intervals during the compression of a water layer. No frequency information was obtained during the time that the oscillator was switched off but it is clear from the points that are collected during the times that the oscillator was running that the frequency followed the curve that has proven typical of all these experiments. This leads to the conclusion that the thinning of a liquid layer is not affected by the presence of the shear waves.

These experiments show what happens to the shear wave parameters during the thinning of a liquid layer but give no real indication of the thickness of the layer. In order to completely understand the process taking place it was necessary to monitor the movement of the top crystal over the course of an experiment.

### 5.1.2 Movement of Top Crystal

The following experiments were designed to examine the movement of the top crystal.
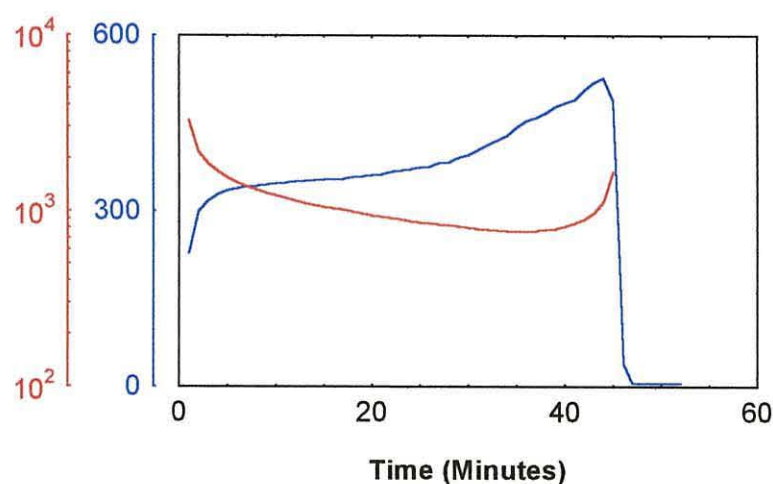


**Figure 5.4 Dielectric properties of thin layer of water when compressed**

———— Capacitance (pF)          ———— Impedance (ohm)

*5.1.2.1 Dielectric Studies*

If the liquid layer is assumed to have a uniform thickness which decreases as it is compressed then the gold surfaces that bound the layer will form a capacitor whose value increases as the separation of the crystals decreases. Compression of a layer between two crystals was carried out without the oscillator but using a component analyser (Wayne Kerr 6425) to measure the dielectric properties of the layer. The analyser was connected to the two electrodes that form interfaces with the liquid sample and applied a 1 volt, 100 kHz signal to this layer. The analyser models the layer as a capacitor and resistor in parallel and displays appropriate values for each component.

A typical result for a water layer is illustrated in figure 5.4. The capacitance rose steadily up to 527 pF and then fell abruptly to 5.08 pF. The capacitance then remained constant for about 5 minutes after which the crystals were separated and observed to be dry. If the final situation is assumed to be an air capacitor with microscopic particles or asperities supporting the top plate but not contributing to the dielectric layer, then the separation of the crystals must be 67.1 μm. If the situation before the abrupt drop is taken to be that of a water capacitor then the distance between the crystals must have fallen from 120.5 μm at the start to 52.0 μm just before the abrupt drop, a total



**Time (Minutes)**

**Figure 5.5 Dielectric properties of a lubricant layer during free fall**

———— Capacitance (pF)          ———— Impedance (ohm)

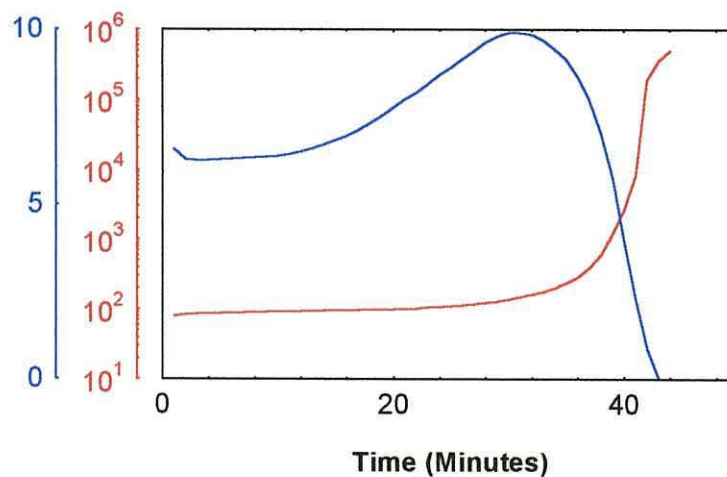distance of 68.5 µm at an average rate of descent of $2.6 \times 10^{-8}$ m s$^{-1}$. This implies that the separation of the crystals was greater after they had dried out than it was when the water layer was at its thinnest. At the time no explanation could be found for this result.

A typical result for the lubricant is illustrated in figure 5.5. This exhibited the same rise in capacitance as in the case for water but the subsequent drop is much slower. From the shape of the curve it appears that the compression of lubricant layers follows the same pattern as that for water. It is not possible to convert the results for the lubricant into absolute distances as the permittivity of the lubricant is not known. The final separation after the lubricant has dried out can, however, be calculated, it is 25.4 µm.

*5.1.2.2 The Atomic Force Microscope (AFM)*

The atomic force microscope is a device which is capable of accurately following surface topography. This could make it a powerful instrument for detecting minute movements of the top crystal. In the AFM is a very sharp stylus mounted on a flexible cantilever. A laser beam is reflected off the cantilever onto a split photo detector. A control circuit minimises the difference signal from the photo detector by driving a piezoelectric platform that raises or lowers the sample being probed. The piezo-drive is mounted upon a micrometer drive, which the operator uses as a coarse adjustment to bring the sample into the correct range for the control circuit and piezo-drive.

A shear wave sensor with gold electrodes was mounted on the sample chuck of the
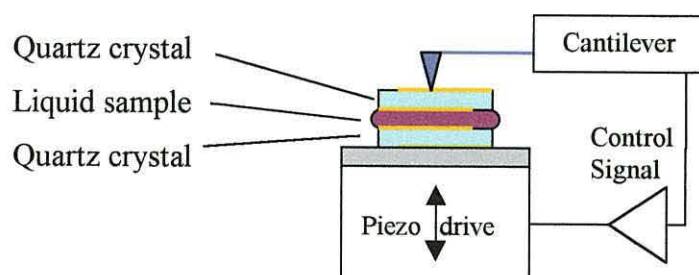


**Figure 5.6 Experimental arrangement using the atomic force microscope to measure changes in the thickness of thin liquid layers**

AFM using a sticky pad. A 2 μl sample of the lubricant was dropped onto the centre of the sensor and a matching crystal placed on top as illustrated in figure 5.6. Space did not permit attachment of an oscillator to measure shear wave data but the experimental set up was as close as possible to that of the shear wave experiments so that the data obtained could be compared to typical shear wave data.

An attempt was made to measure the control signal applied to the piezo-drive. As the lubricant layer thins the top crystal should recede away from the stylus and the voltage of the control signal would increase as the sample chuck was driven upwards in order to maintain contact between the stylus and the surface. This method of observation proved impractical because the piezo-drive had insufficient range.

A practical means of measurement was to drive the sample chuck upward using the micrometer drive until the AFM's software display indicated that the sample was at the maximum working height. As the top crystal falls toward the sensor the piezo-drive compensates going from one limit to the other. The time taken for this to occur is recorded along with the distance through which the micrometer must be moved to take the sample from the minimum working height back to the maximum. These two measurements were used to derive the speed at which the top crystal is falling. The measurements were plotted and extrapolated to give an estimate of the initial speed.
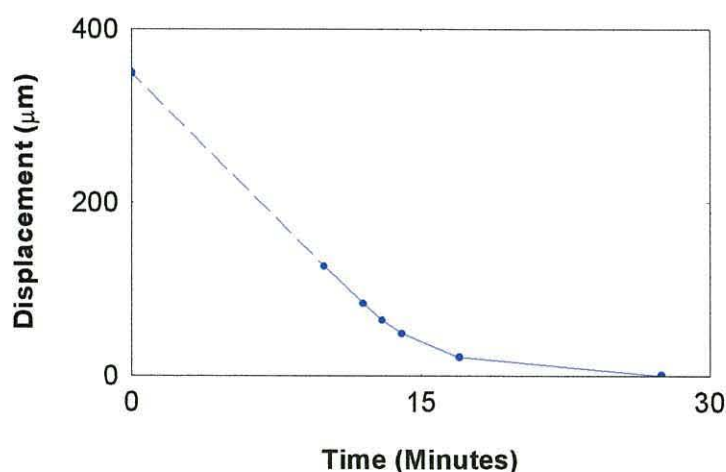


**Figure 5.7 Movement of top crystal measured using the AFM**

The curve was then integrated to give an estimate of the distance moved, illustrated in figure 5.7. The movement settles to a final rate of descent of $3.45 \times 10^{-8}$ m s$^{-1}$, at this rate the total distance covered would be 57.7 $\mu$m. There were a number of problems with this measurement. It took nine minutes from assembling the experiment to the first measurement and the movement during this time is unknown. A source of error is that it took time to move the micrometer when taking the sample from the minimum to the maximum working height and movement of the top crystal during this time results in an exaggerated reading. Once the movement appeared to be complete the experiment was left unattended and during this time the stylus tip was damaged by some force driving it into the surface. At that time there was no explanation for this event.

*5.1.2.3 The Laser Profilometer*

As part of the collaboration with Unilever Research use was made of the laser profilometer at their laboratories in Port Sunlight. This instrument is similar to the AFM in that it accurately follows surface topography, however the laser profilometer makes no contact with the surface but instead uses a laser stylus (Rodenstock RM600) as an optical follower to probe the surface. An auto-focus mechanism keeps the stylus



**Figure 5.8 Simultaneous measurement of the movement of the top crystal measured with a laser stylus and the corresponding change in resonance frequency**

————— movement ($\mu$m)          ————— $\Delta f_s$ (Hz)
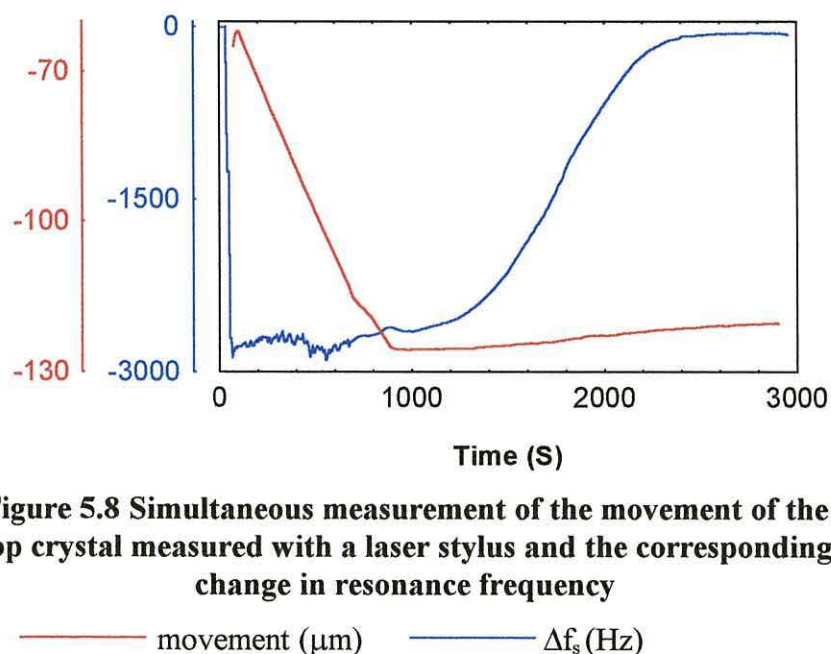
focused on the surface and a voltage output is provided that is proportional to the distance between the laser source and the surface.

The experiment was set up with the sensor connected to an oscillator and the laser stylus focused on a selected point close to the centre of the top crystal. The calibrated voltage output from the stylus was recorded throughout the experiment so that a simultaneous measurement was made of the shear wave parameters and the movement of the top crystal. The results illustrated in figure 5.8 show that most of the descent of the top crystal was over before the series resonant frequency of the sensor began to rise. As the frequency follows the typical curve the top crystal actually rises. The descent covers a total distance of 63.5 $\mu$m at a rate of $6.3 \times 10^{-8}$ m s$^{-1}$, this was followed by a rise of 5.3 $\mu$m.

The rise revealed by the profilometer validates the results of the dielectric studies and explains the damage to the AFM tip. The reason for this rise is that the liquid film breaks up leaving small micro-droplets that are able to lift and support the top crystal.

### 5.1.3 Optical Microscope Studies

In order to examine directly the departure of liquid from between the quartz surfaces, an experiment was designed where the processes taking place in the film could be visually observed. The crystals were replaced by 10 mm glass cover slips and the film was formed by 10 $\mu$l of water loaded with approximately 1 mg of napthol blue black dye per 25 cm$^3$ of water. The experiment was set up on the stage of a stereo microscope (Nikon) with the zoom adjusted so that the cover slips filled the whole field of view.

Observation of the film in this way shows that it is unstable, after a few minutes the film begins to break up at one edge. This edge then develops into a boundary between the liquid film and air which sweeps across the surface of the glass. The boundary approximates to a straight line at right angles to its direction of motion, curving forward slightly at either end. Small dust particles are swept along by the boundary. When the boundary moves over an irregularity such as a larger dust particle or a chip in the glass it is first stretched and, as the whole boundary continues across the surface
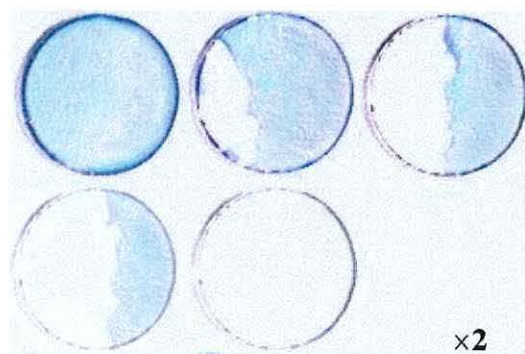
**Figure 5.9 Stages in the break-up of the liquid film (dyed blue)
between glass discs**

in the glass it is first stretched and, as the whole boundary continues across the surface this point is necked and then finally breaks leaving a small water droplet surrounding the irregularity. Once the boundary reaches the opposite side of the cover slip the sensor is seen to be completely dry apart from a few microdroplets left clinging to irregularities.

A video camera was then used to produce a permanent record of the process. The cover slips were placed on a piece of white paper with a light source above. Three different films were used in the video record: water, the lubricant and a 0.025% solution of Tween-20™ in water. All three films were dyed with the napthol blue black. Figure 5.9 shows a series of stills from the record of the gradual retreat of the lubricant film.

In order to correlate the break up of the film with shear wave measurements an experiment was devised to image the process by using a quartz sensor as the lower surface, a glass cover slip as the top surface and 4 µl of water coloured with the dye as the liquid sample. It was observed that as the water/air boundary moves across the surface of the sensor the shear wave response changed from water loading to air loading. The rate of movement of the film boundary was measured by using the microscope with a calibrated graticule in the eyepiece and timing the advance of the boundary across the graticule scale. These results make it possible to compare the film coverage with the shear wave data.

Although the acoustic load presented by the water film is constant across the surface of the sensor, the sensitivity of the sensor follows an approximately Gaussian profile with the greatest sensitivity being in the centre. Thus when a load only acts on part of the sensor surface account must be taken of this variation in sensitivity. This is done by integrating the sensitivity function over the area covered by the water film. If we make the simplifying assumption that the air/liquid boundary is a straight line, the calculated change in the load, $\Delta L$, for a partial water film is given by:

$$\Delta L = \int_d^2 \int_{-2}^2 L_{max} e^{-a(x^2+y^2)} dx\, dy$$

where d is the fraction of the radius of the electrode over which the film boundary has moved, $L_{max}$ is the acoustic load presented by a complete film and a is the Gaussian coefficient which defines the width of the sensitivity function. The expected change in load is shown in figure 5.10 superimposed over the measured data showing a good fit. This shows that the response of the partially covered sensor can be modelled by integrating the sensitivity function over the covered area of the crystal.
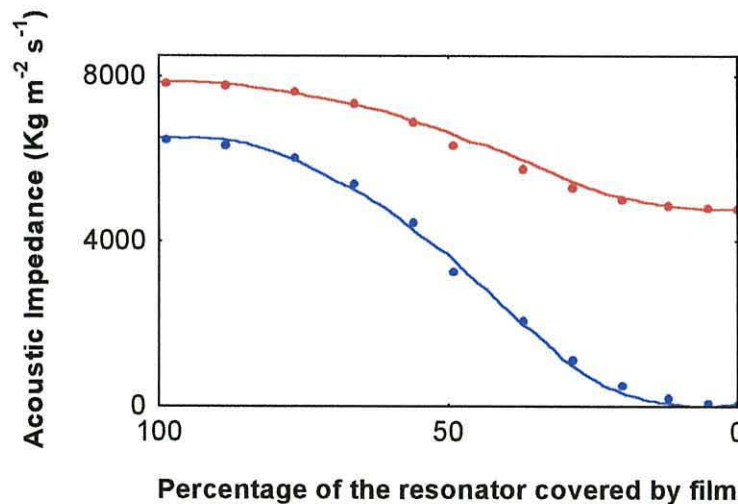


**Figure 5.10 Effect of film coverage on shear wave response**

―――― Measured R     ―――― Measured X
•  Calculated R     •  Calculated X

Having shown that these films are unstable it was necessary to confirm the stability of a confined film surrounded by liquid instead of air. A plastic tube was fitted to the cover slip that maintains air above the glass. The tube is open at the top so that the film can be viewed with the microscope and is weighted around the outside in order to compress the film. The shear wave sensor was mounted in a trough and totally immersed in dyed water. The film did not break up but proved to be stable.

### 5.1.4 Micro drive Studies

The aim of these experiments was to investigate the response of the shear wave sensor to an accurately defined change in the thickness of a water layer. The sensor is set up in a similar manner to the earlier experiments except that the matching crystal is no longer free to move but is fixed to a piezo-drive as illustrated in figure 5.11. This consists of a piezoelectric tube, T, (Unilator Technical Ceramics, PZT 5H) with electrodes inside and out, when a positive voltage is applied to the outside electrode the tube shrinks by 6.96 µm per volt. Coarse adjustment is achieved using a micrometer screw drive that has a sensitivity of about 0.5 µm per rotation. The micrometer drive has some backlash and the operator's hand introduces vibration into the system, therefore the micrometer is used only for coarse adjustments and the piezo drive is used to change the layer thickness while the shear wave parameters are



T  Piezoelectric tube
C  Matching crystal
L  Liquid sample
S  Quartz sensor
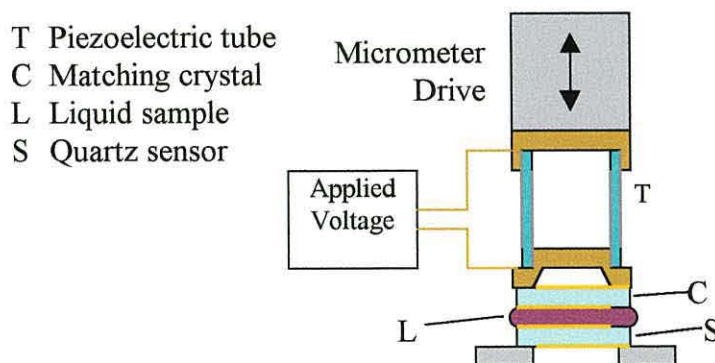
**Figure 5.11 The Microdrive Apparatus**

recorded.

The connections to the piezo drive and the sensor are made by fine wires allowing the apparatus to be mounted so as to reduce vibration. Low frequency vibrations are damped out by placing the apparatus on a concrete block that is suspended from three elastic cords. Higher frequencies are removed by suspending the sensor and drive assembly with tense steel wires.

This experiment proved to be very susceptible to drift and noise. The results show that as the separation is reduced by 2.5 $\mu$m the frequency rises by 400 Hz following the s-shaped curve illustrated in figure 5.12 Note that the distance here is not the absolute separation, which is not known accurately, but the relative movement of the surfaces. It seems likely that this effect is due to microdroplets being squeezed and thus spreading out to contact an increased area of the sensor surface. This result provides further evidence that the film is unstable rather than giving any information on the effect of film thickness.

## 5.2 Adsorption

Adsorbed surfactant molecules on friction surfaces play an important role in the mechanism of boundary layer lubrication (Bowden 1950). Adsorption was observed in section 5.1.1 as the commercial lubricant was repeatedly applied to the sensor, and so
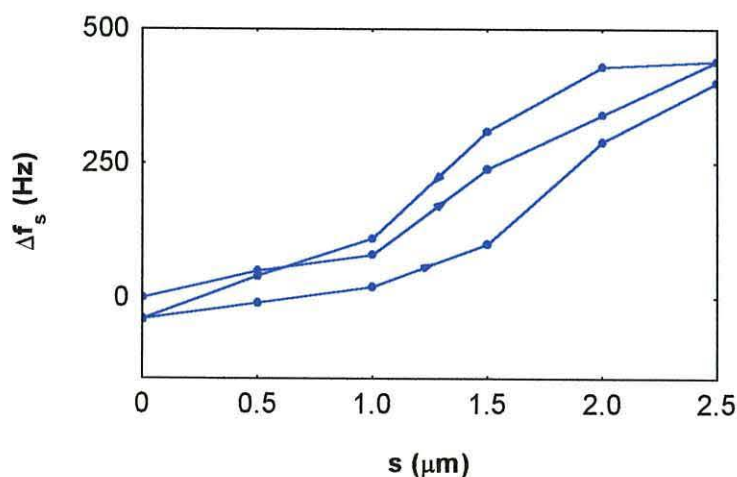


**Figure 5.12 Dependence of resonance frequency on crystal separation, s.**

it was decided to examine adsorption briefly by the relatively simple technique of estimating the contact angle of the lubricant liquid.

### 5.2.1 Contact Angle Studies

The presence of adsorbed layers can be detected by their effect on the contact angle of a liquid droplet on the surface (Robinson 1989)(Bain 1988). When a liquid droplet is placed on a solid surface its shape depends on the surface energies associated with the interfaces between the three phases. The contact angle between the droplet and the surface, $\theta$, is defined by the Young equation.

$$\gamma_{SV} - \gamma_{SL} - \gamma \cos \theta = 0$$

where $\gamma_{SV}$, $\gamma_{SL}$ and $\gamma$ are the surfaces energies of the solid-vapour, solid-liquid and liquid-vapour interfaces respectively. Thus measurement of a liquid contact angle offers a simple means of gauging the hydrophobicity of a surface. The presence of adsorbed material on the gold surface has the effect of changing the hydrophobicity and consequently the contact angle.

When clean, the gold electrodes of the quartz sensors are hydrophobic and a droplet of 10 ml of water made a contact angle which was judged to be about 70 degrees. A droplet of 10 ml of the lubricant dropped onto a clean gold surface formed a bead with the same contact angle as water. Over the course of a few minutes this bead spread across the surface until it had a final contact angle of about 30 degrees. The lubricant was left to evaporate and, once the surface had dried, a droplet of 10 ml of water was applied to the surface. This time the water droplet immediately spread out to cover the same area as the lubricant had occupied and had the same contact angle of about 30 degrees. Over a few minutes the water droplet spread out further and covered the whole electrode surface, this occurred because the water droplet was able to pick up and re-deposit the excess surfactant, which had been left on the surface after the lubricant had evaporated.

One of the samples of lubricant provided by Unilever contains sufficient acetic acid to lower its pH from 6.4 to 3.4. The acetic acid inhibits the adsorption of surfactant and when a droplet of this sample was dropped onto a clean surface it did not spread out as

the other lubricant sample did but formed a bead with a contact angle only slightly lower than that of water, about 60 degrees. When this bead had evaporated it left a visible ring on the surface where the edge of the bead had been, when water was dropped onto the surface it immediately flowed to this ring suggesting that the ring was made up of excess surfactant left behind when the lubricant evaporated.

In both cases the surface could be cleaned either by rinsing in water or wiping which a wipe soaked in iso-propanol. Once cleaned the surface has the same contact angle with water as a fresh surface thus proving the effectiveness of the cleaning procedure.

### 5.2.2 Shear Wave Impedance of Adsorbed Layers

The quartz crystal sensor is able to detect very small loads on its surface and can be used to study the adsorption of thin layers from a solution (Auge 1994). The effect of the adsorption of surfactant molecules on the shear wave response of a sensor is much smaller than that caused by the transition from air to water loading so experiments were designed that enabled the process of adsorption onto the gold electrodes to be observed in isolation.

A tube was fitted to the sensor cell so that a column of liquid could be maintained above the sensor. In this configuration a column of ultra-pure water above the sensor caused a cyclic variation in the response as illustrated in figure 5.13. This is due to the presence of the compression waves, described in section 3.3.2, which are strongly reflected from the water-air boundary. As the water evaporates the compression wave path length is reduced and the additional load on the sensor goes through cycles as the path length goes through half wavelengths. To remove this effect a glass rod with a rounded end was fixed in a clamp so that its end was immersed in the liquid above the sensor, this has the effect of scattering the compression waves. The system is still sensitive to mechanical vibration and care must be taken during these measurements.
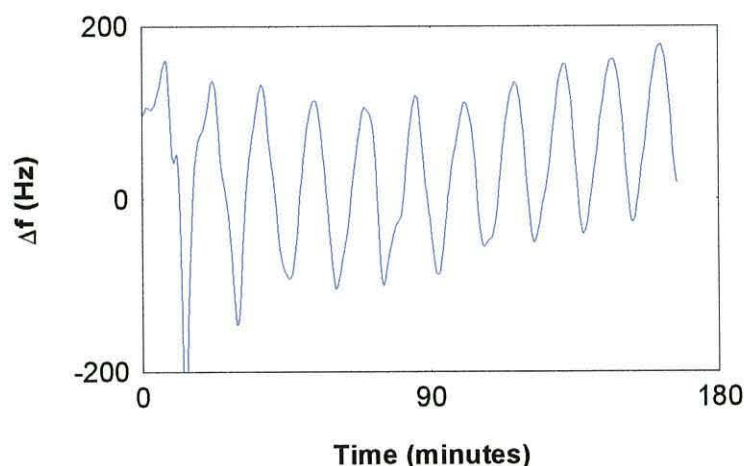
**Figure 5.13 Oscillatory change in resonance frequency due to reduction in liquid thickness by evaporation**

The ability of the sensor to detect adsorption was first tested using bovine serum albumin (BSA) because it was expected to have a large effect. The measurements were started with 1 ml of pure water in the sensor cell and a glass rod as a compression wave spoiler. After a few minutes 1 ml of water containing 50 mg of BSA was added to the water already in the cell and mixed well. The results illustrated in figure 5.14 show an abrupt step down in frequency which is due to the step change in liquid viscosity, this is followed by the adsorption curve. When good reproducible results were obtained for BSA the experiment was repeated using two thiols of different molecular weights. Thiols are chosen because they readily self-assemble onto gold forming a classical boundary lubricant.

Adsorption of octadecane thiol, ODT, and decane thiol were more difficult to measure due to the problem of finding a solvent which did not dissolve the silicone rubber sealant but readily dissolved the thiol. Ethanol was chosen as it did not damage the sealant significantly over the time-scales of these experiments and could be made to dissolve octadecane thiol if sonication was used to help break up the particles. The effect of the thiol adsorption was hard to separate from noise and temperature effects and a better measurement system was sought.
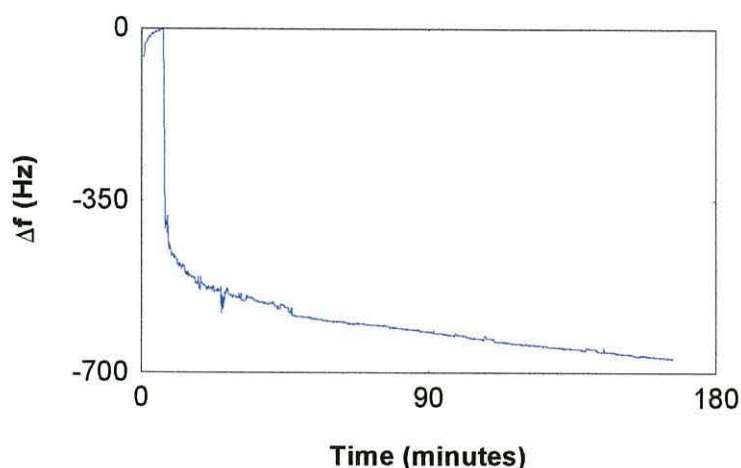
**Figure 5.14 Response of sensor to adsorption of BSA**

When the current controlled oscillator described in section 4.1.3.3 was developed it became possible to use crystals with both faces in contact with liquid and a cell was designed, illustrated in figure 5.15, which allowed adsorption to take place on both surfaces. The sensor was supported on a wire frame to eliminate the acoustic damping that arises from the effect of the silicone sealant on the edges of the crystal. The cell was made in two halves sealed with an O-ring and held together by a spring clamp. Connections for plastic tubing were provided at the top and bottom of the cell to permit solvent to be circulated through the cell by means of a peristaltic pump. After the sensor settled with the solvent circulating, the surfactant solution was introduced to an external reservoir without any mechanical interference to the sensor.

Figure 5.16 illustrates adsorption curves obtained for the thiols in this way. The curves clearly show the process of adsorption. Although ODT has a larger molecular weight

the change in resonant frequency is smaller for ODT than it is for decane thiol. The Sauerbrey microbalance equation (equation 3.15) (Sauerbrey 1959) can be used to estimate the mass densities of the adsorbed layers. The mass density of the ODT layer was $1.716 \times 10^{-6}$ kg m$^{-2}$ this is equivalent to $3.613 \times 10^{18}$ molecules per square metre. The mass density of the decane thiol layer was $1.22 \times 10^{-5}$ kg m$^{-2}$ and this is equivalent to $4.224 \times 10^{19}$ molecules per square metre. Lio (1997) found that a closely packed monolayer of alkane thiol forms a hexagonal ordered structure with a periodicity of 5 angstroms. These films should have $4.62 \times 10^{18}$ molecules per square meter. Thus it seems that ODT forms a complete monolayer while decane thiol deposits around ten monolayers.
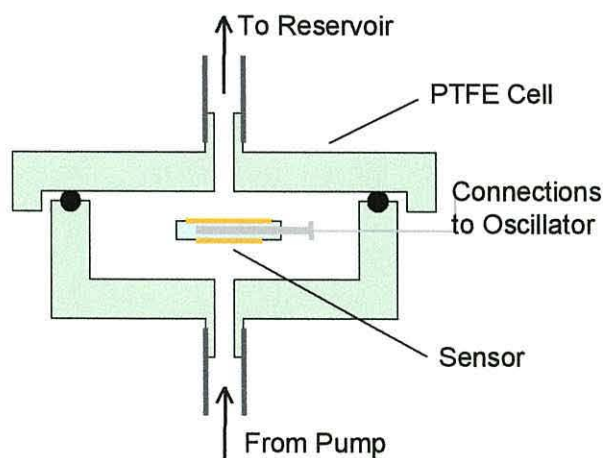


**Figure 5.15 Cell for measuring adsorption**

(a)



(b)
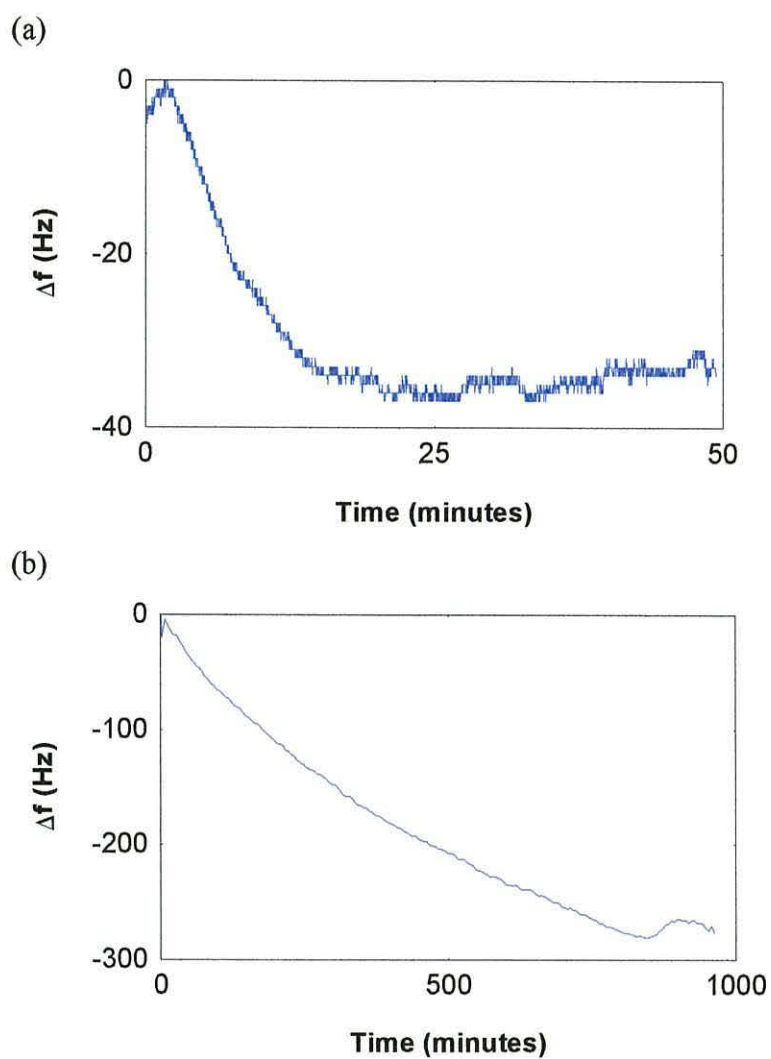


**Figure 5.16 Response to adsorption of thiols**

(a) Octadecane Thiol  (b) Decane Thiol

## 5.3 Normal Load

After a compressed liquid layer has completely broken up there is a small residual load on the sensor. Visual observation, (section 5.1.3) indicates that there are fine water droplets left between the surfaces in addition to surfactant molecules adsorbed onto the surfaces. In order to find out whether the shear wave properties of this residual layer are affected by changes in normal load, the load on the top crystal was altered and the shear wave properties recorded. Simply removing the weight and replacing it with one of a different size proved to be subject to operator-induced variations and a more controllable method was devised which made use of a hollow plastic vessel, illustrated in figure 5.17. A fine needle was held in a clamp so that its tip was just above the floor of the vessel. Water was pumped into and out of the vessel by means of a peristaltic pump connected to the needle. The mass of the load could thus be changed by about 1 g and a qualitative observation of the response to normal load was thus obtained.

Three different types of layer were investigated and all gave different results. When the system was assembled dry with no liquid sample no change could be detected on varying the load. A water layer was compressed until it broke up. Once the process was complete water was pumped into and out of the weight repeatedly. As the normal load increased the imaginary part of the acoustic impedance ($Z_L = R_L + iX_L$) decreased
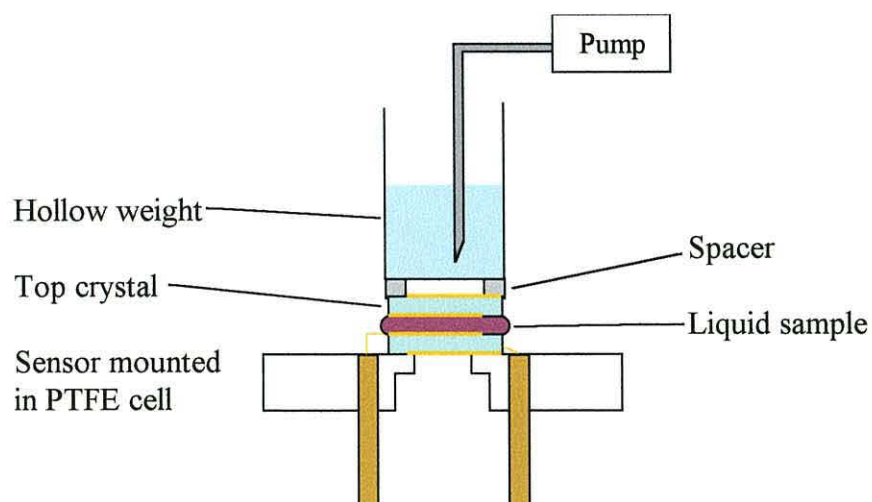


**Figure 5.17 Experimental arrangement used to vary the normal load on the film**

and recovered when the weight was reduced (figure 5.18a). The experiment was then left undisturbed for one hour before the process of cycling the weight was repeated. This time there was no detectable change in the imaginary part but a small change in the real part (figure 5.18b).

(a)



**Time (minutes)**

(b)



**Time (minutes)**
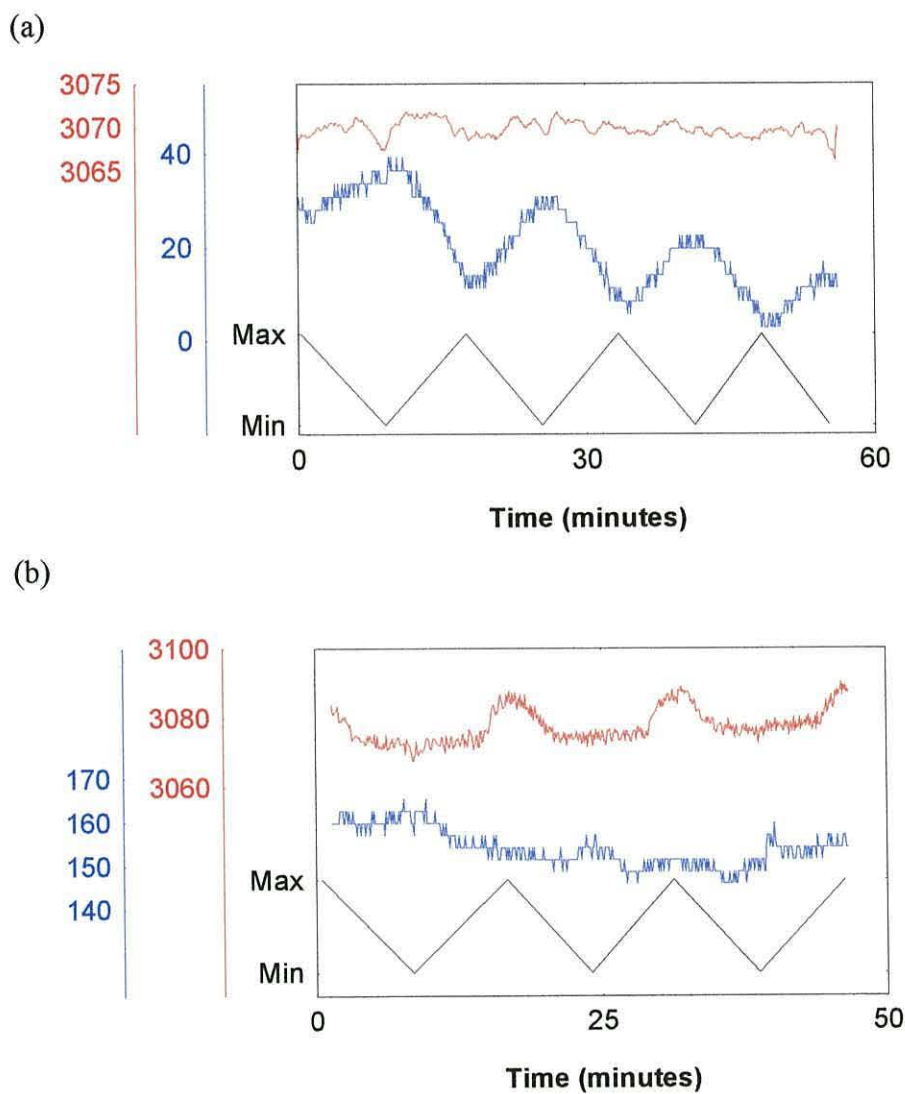
**Figure 5.18 Effect of static load on a residual film**

(a) Immediately after break up of film. (b) One hour after break up.

——— R (kg m$^{-2}$ s$^{-1}$)        ——— Normal load

——— X (kg m$^{-2}$ s$^{-1}$)
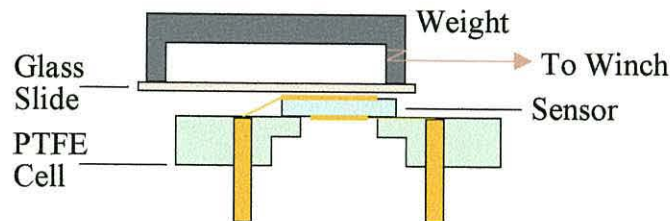
**Figure 5.19 Experimental arrangement for examining sensitivity to shearing**

## 5.4 Sensing Sliding Friction

It was important to determine at an early stage whether the shear wave sensors are capable of detecting the effect of sliding friction on their surfaces by setting up the simple experiment shown in figure 5.19. A thin glass slide slightly wider than the sensor and approximately three times as long had a weight mounted on its upper side supported on short pillars at the ends of the slide. When the slide was placed on top of the sensor the weight provided a normal load upon the surfaces but did not contribute



**Time (minutes)**
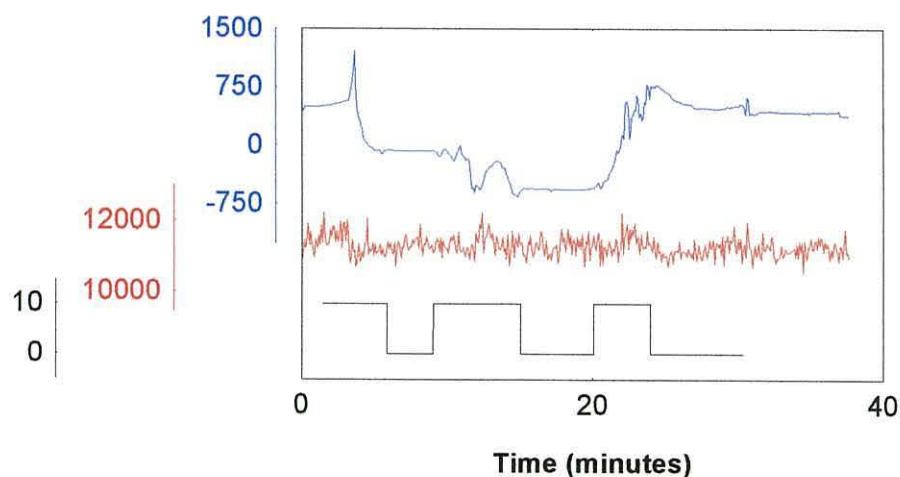
**Figure 5.20 Response of sensor to shearing motion of a glass slide**

R (kg m$^{-2}$ s$^{-1}$)        Shearing speed (μm s$^{-1}$)
X (kg m$^{-2}$ s$^{-1}$)

to the shear wave acoustic load. A light piece of thread was fixed between one end of the slide and the spindle of a constant speed electric motor which 'winched' the slide across the surface of the sensor giving a shearing motion with a speed of approximately 10 $\mu$m s$^{-1}$.

Typical results, illustrated in figure 5.20, show a clear but inconsistent response in the imaginary component of the acoustic load to the motion of the glass slide. This preliminary experimental evidence was sufficiently encouraging to justify a fuller investigation. The design of the precision tribometer described in section 4.2.3 was embarked upon.

## *5.5 Tribometer Experiments*

### 5.5.1 Positional Sensitivity of the AT-Cut Crystal to a Point Contact

The sensitivity of the shear wave sensors to a mechanical contact is not constant over the surface of the sensor but varies according to the position of the contact. It has been shown (Hillier 1992) (Cumpson 1990) (Martin 1989b) that the sensitivity is greatest in the centre of the active area and decreases towards the edges of the sensor following a curve that is approximately Gaussian. In friction experiments, where a physical point of
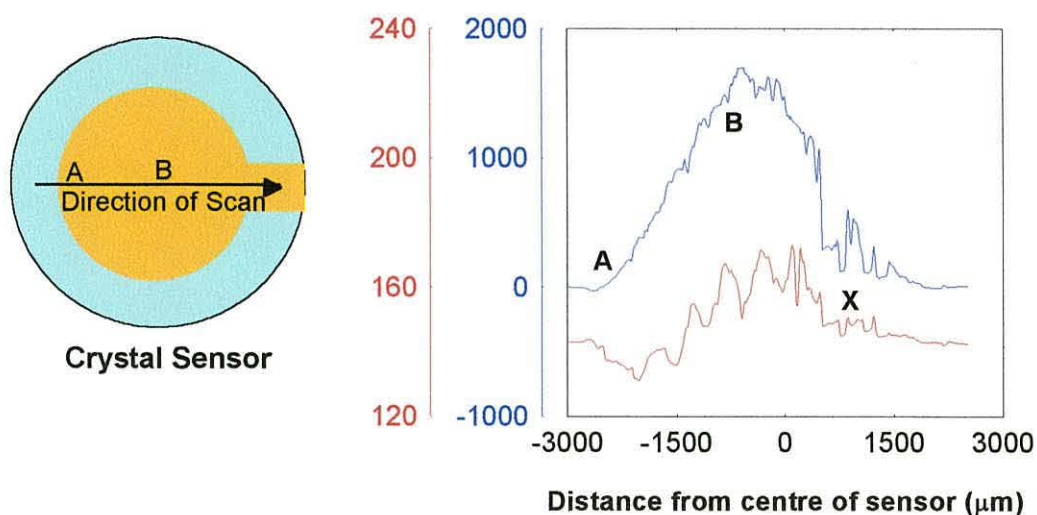


**Figure 5.21 Response of Sensor to a 10 mm diameter ruby sphere**

——— $\Delta f_s$ (Hz)      ——— $|Z_{min}|$ ($\Omega$)

contact is moved over the surface of a sensor, it is essential to allow for this variation in sensitivity.

A 10 mm diameter ruby sphere, polished to a 1.0 $\mu$m finish, was mounted on the friction probe of the tribometer and a 5 g normal load was applied. The ruby makes a well-defined and repeatable contact on the gold electrode of a sensor mounted on the moving stage. The ruby was moved slowly over the surface of the sensor under computer control and stopped every 10 $\mu$m in order to measure the shear wave response to a stationary contact. Figure 5.21 shows the response to the ruby over a diameter of the sensor electrode. Both $\Delta f_s$ and $Z_{min}$ follow the Gaussian profile, $Z_{min}$ also exhibited some cyclic variations. Some noise is present on both curves, e.g. At point X, and this is thought to be caused by microscopic debris that affects the mechanical contact of the ruby.

The smoothest part of the curve is the region between -2600 and -500 $\mu$m, labelled A and B in figure 5.21, and this region was used to examine the response to a sliding contact. The normal load was increased to 10 g and the contact point traversed backwards and forwards between the two points. The response is shown in figure 5.22a along with the output of the strain gauge. Both $\Delta f_s$ and $Z_{min}$ closely follow the profile illustrated in figure 5.21 including the cyclic variations in $Z_{min}$ and the noise in $\Delta f_s$ near point B. When the direction changed the response exactly mirrored that for the opposite direction indicating that the surface was not significantly changed by the process. The force output clearly shows steps as the direction of motion changes. The noise in the force output was shown to be electrical in nature and was reduced in later experiments by incorporating a low pass filter between the output of the instrumentation amplifier and the input of the analogue to digital converter. The sliding ruby deformed the gold surface making a track which appeared to the naked eye as a sharp straight line. Part of this line was studied using an Atomic Force Microscope (AFM). The resulting image is shown in figure 5.22b and reveals that the line is in fact made up of several microscopic furrows spaced about 2 $\mu$m apart. The deformed region has clearly defined edges giving a value for the diameter of the contact of the

(a)
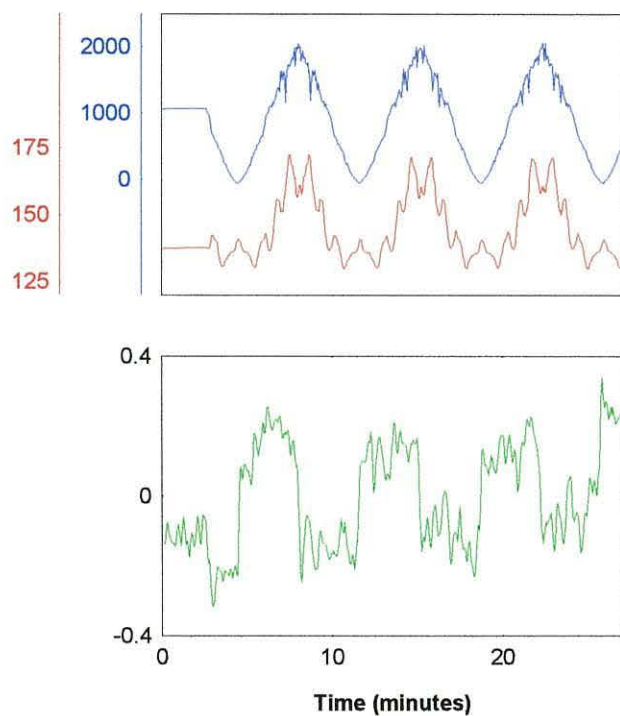


(b)
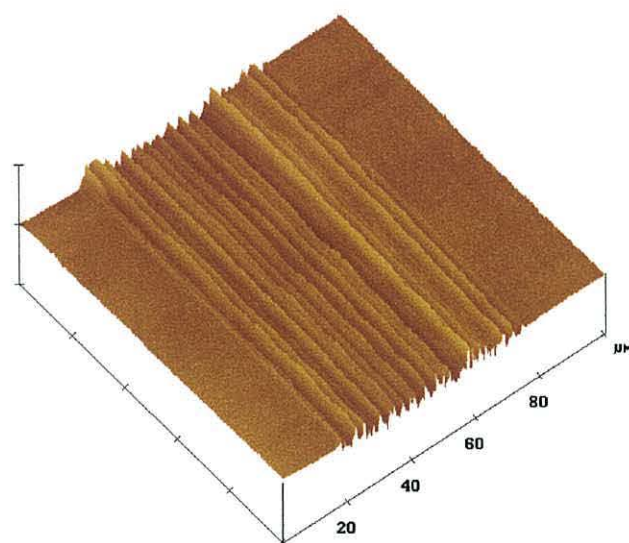


**Figure 5.22 Sliding Contact of Ruby Sphere**

(a) Acoustic and Strain Gauge response to oscillatory motion
(b) AFM image of surface damage produced by sliding

————— $\Delta f_s$ (Hz)     ————— $|Z_{min}|$ ($\Omega$)
————— Ratio of friction force to normal load

ruby as 62 µm. The deepest furrow is approximately 40 nm deep, this is not deep enough to completely penetrate the 100 nm thick gold layer.

The response to a stationary contact was investigated with different normal loads. The results are illustrated in figure 5.23. It is clear that a larger normal load results in a greater response. An abrupt gap in the response at point A reinforces the hypothesis that the response is affected by surface debris. The AFM confirmed that there was a debris particle with a height of around 4.0 µm on the surface of the crystal at that point. Examination of these curves reveals that the cyclic variations observed in $Z_{min}$ are also present in $\Delta f_s$ but are less significant compared to the overall Gaussian shape than they are in the $Z_{min}$ response.
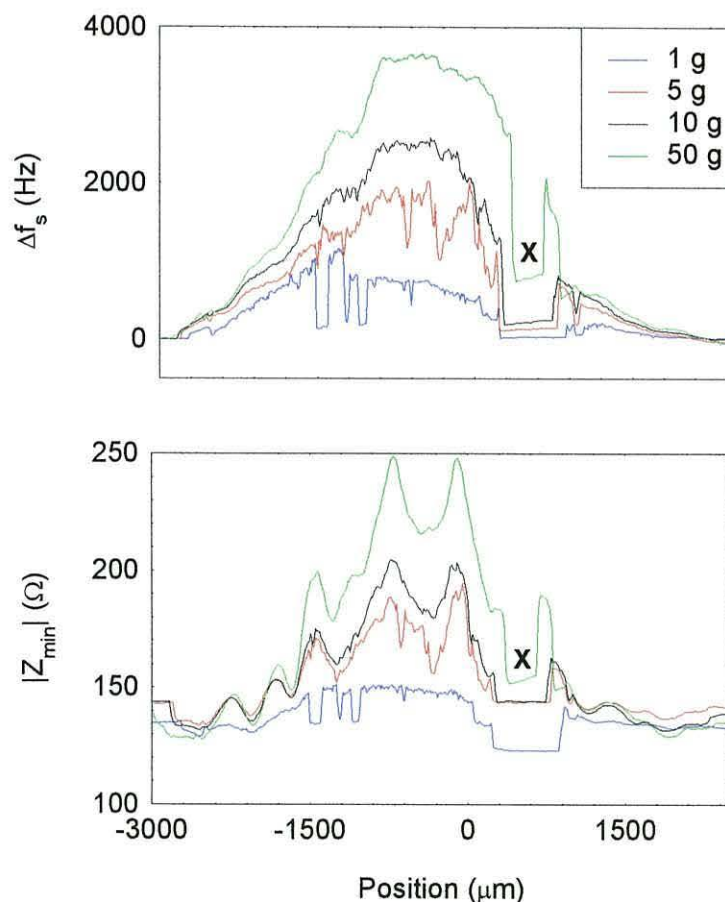


**Figure 5.23 Response of sensor to stationary contact with ruby sphere with selected normal loads.**

X Response interrupted by surface debris

These experiments demonstrate the response of the sensor to a point contact. In tribology experiments, however, the surface of the sensor is in contact with the surface of a matching crystal and this type of contact must also be investigated.

### 5.5.2 Sensitivity of the Quartz Sensor to a Matching Crystal

It is necessary to understand the response of the quartz crystal to a matching crystal as the surfaces are sheared and the area of overlap changes. A sensor crystal was mounted on the tribometer and a matching crystal was glued to the lip of a shallow inverted brass cup so that an air gap was always maintained above the active area of that crystal. This crystal was placed on top of the sensor crystal and a small amount of a two part epoxy adhesive (araldite) was placed on the base of the cup. The friction probe was brought down onto the adhesive and a weight was placed on top of the
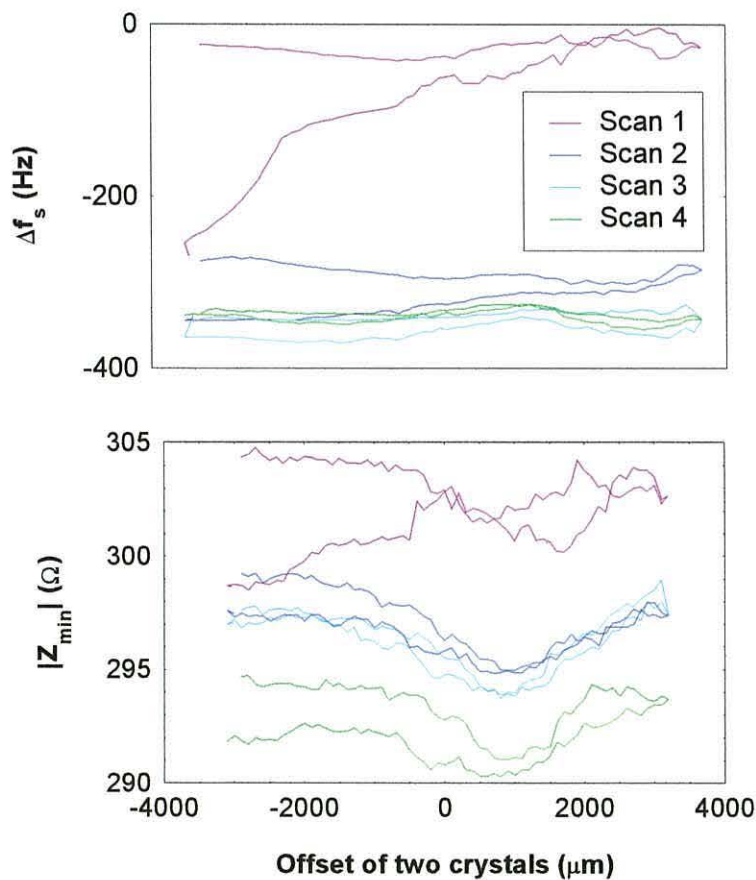


**Figure 5.24 Response to a matching crystal load**

probe in order to keep it in place. Once the adhesive was hardened the crystal remained parallel to the sensor while the probe was raised and lowered.

The effect of a changing area of overlap on the response was investigated. A normal load of 2 g was applied to the surfaces and the top crystal was moved across the sensor and back four times, pausing every 100 μm to measure the response to the stationary contact. The results are illustrated in figure 5.24. Both the series resonant frequency, $f_s$ and the corresponding impedance, $Z_{min}$ of the sensor were reduced by each sweep. This reduction was more pronounced in the first two sweeps indicating that there is a wearing-in process between the surfaces, the reduction is also more pronounced in the reverse direction showing that the wearing-in occurs more readily in this direction. The centre position of the scan had been set by judging by eye when the
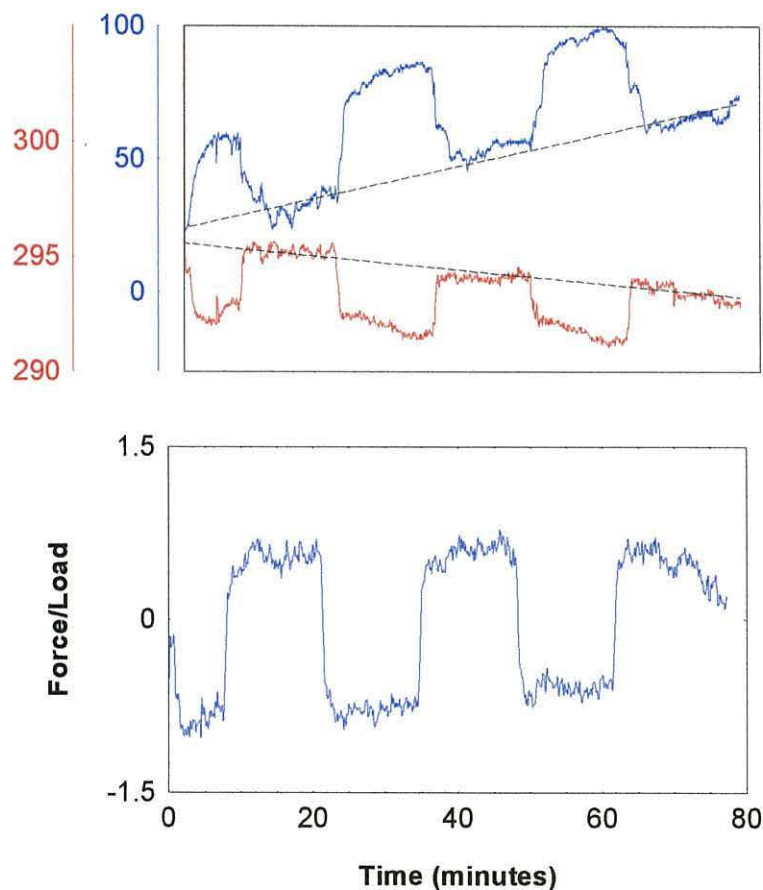


**Figure 5.25 Response to shearing two crystals**

———— $\Delta f_s$ (Hz)       ———— $|Z_{min}|$ (Ω)

crystals were in line. The $Z_{min}$ curves clearly show that the response curve is symmetrical about a point 850 μm offset from the centre of the scan. The centre position for subsequent experiments was adjusted accordingly. Once the surfaces have worn in the response is quite flat around the centre of the curve, shearing experiments were carried out in this region in order to minimise the effect of the change in overlap of the crystals.

The normal load was increased to 20 g and the crystals were sheared with a shear amplitude of 400 μm and a shearing speed of 0.5 μm s$^{-1}$ The results are shown in figure 5.25. $\Delta f_s$ rose by about 50 Hz when the crystals were brought into contact. The sensor responds to sliding motion and is also sensitive to the direction of motion, this is
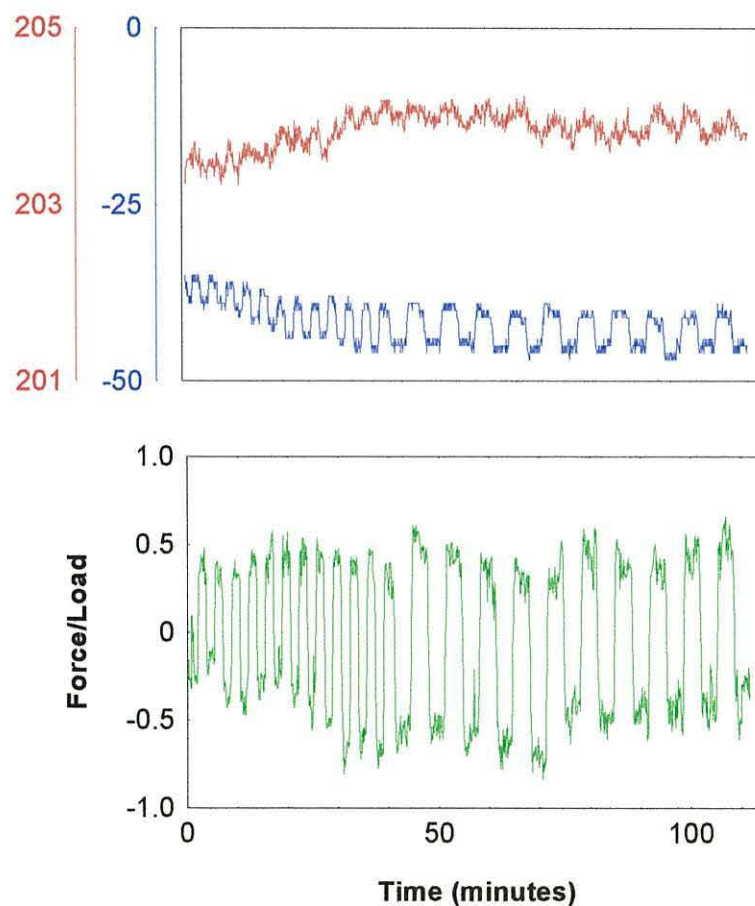


**Figure 5.26 Wearing-in of clean surfaces**

———— $\Delta f_s$ (Hz)          ———— $|Z_{min}|$ (Ω)
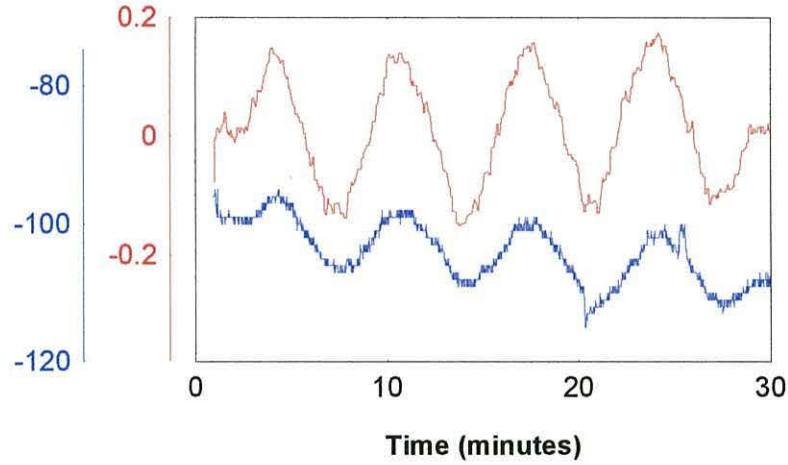
**Figure 5.27 Sticking of surfaces under high normal load**

———— $\Delta f_s$ (Hz)        ———— $|Z_{min}|$ ($\Omega$)

because the acoustic coupling is better in one direction than the other. There is also a drift in both parameters that must be investigated.

Fresh parallel crystals were set up and the experiment was refined by reducing the shear amplitude to 100 μm and ran for a longer time in order to investigate the drift in the measurements. Initially the sliding speed was 1 μm s$^{-1}$ then after 40 minutes the speed was reduced to 0.5 μm s$^{-1}$, the normal load was 10 g. The results are illustrated in figure 5.26, $f_s$ dropped by only 6 Hz as the surfaces wore in and then responded to the shearing motion and the direction of sliding. The ratio of friction force to normal load initially increases as the surfaces wear in then remains roughly constant.

### 5.5.3 Static Friction

*5.5.3.1 Sticking Surfaces*

An experiment was arranged to shear parallel crystals with gold surfaces backwards and forwards with a shear amplitude of 10 μm and a normal load of 50 g. The surfaces did not slide but remained stuck. The speed of the moving stage was 0.125 μm s$^{-1}$, figure 5.27 shows the response of $\Delta f_s$ and the force output. The surfaces are in stick all the time and never slide relative to each other. The force output traces a triangular shape as the tension in the leaf spring increases with the linear motion of the stage. The
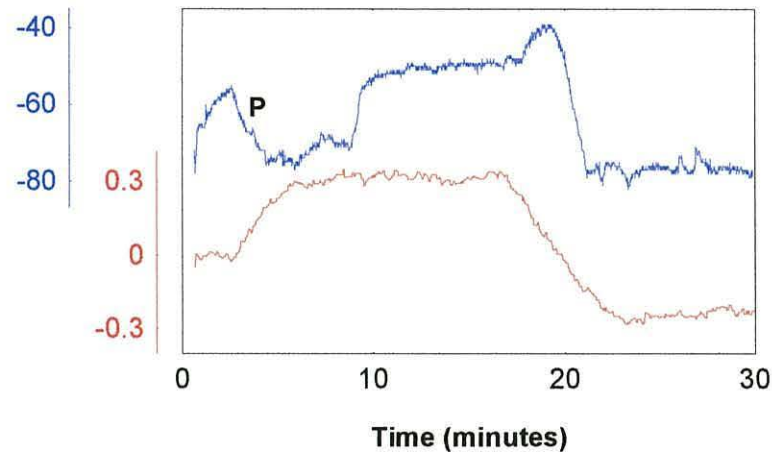
**Figure 5.28 Determining the static friction coefficient**

———— $\Delta f_s$ (Hz)    ———— $|Z_{min}|$ ($\Omega$)

direction of motion is reversed before the tension in the spring is sufficient to overcome the static friction. Measuring the slope of the force plot allows the stiffness of the leaf springs to be calculated. It is 0.7317 KgF mm$^{-1}$. Even though there is no shearing between the two surfaces there is a response in $f_s$ that corresponds to the movement of the stage, this is because, as the stage moves, the load distribution on the sensor crystal shifts slightly. By increasing the shear amplitude the surfaces can be made to slip.

*5.5.3.2 Static Friction Coefficient*

By maintaining the high normal load of 50 g and increasing the shear amplitude to 50 μm it was possible to observe the point at which sliding begins. Figure 5.28 shows the response of $\Delta f_s$ and the force output for this experiment. Once sliding was established the direction of travel was reversed so that a second measurement could be taken. Sliding began to take place when the ratio of friction force to normal load was 0.32. In the forward direction a change in $\Delta f_s$ (P in figure 5.28) indicates that a change in the surface contact takes place before the onset of sliding.

### 5.5.3.3 Stick-Slip Motion

Reducing the normal load to 20 g while maintaining the sliding speed of 0.125 μm s⁻¹ caused the surfaces to exhibit the stick-slip type motion illustrated in figure 5.29. For the first two minutes the surfaces were in a state of stick, and the strain gauge output rose in a linear manner. Shortly after two minutes the surfaces slipped (point A, figure 5.29) resulting in a step drop in the force, at the same time there was a downward spike in $\Delta f_s$ indicating an increased acoustic load at this time. The surfaces then stuck for some time before slipping again (point B, figure 5.29).
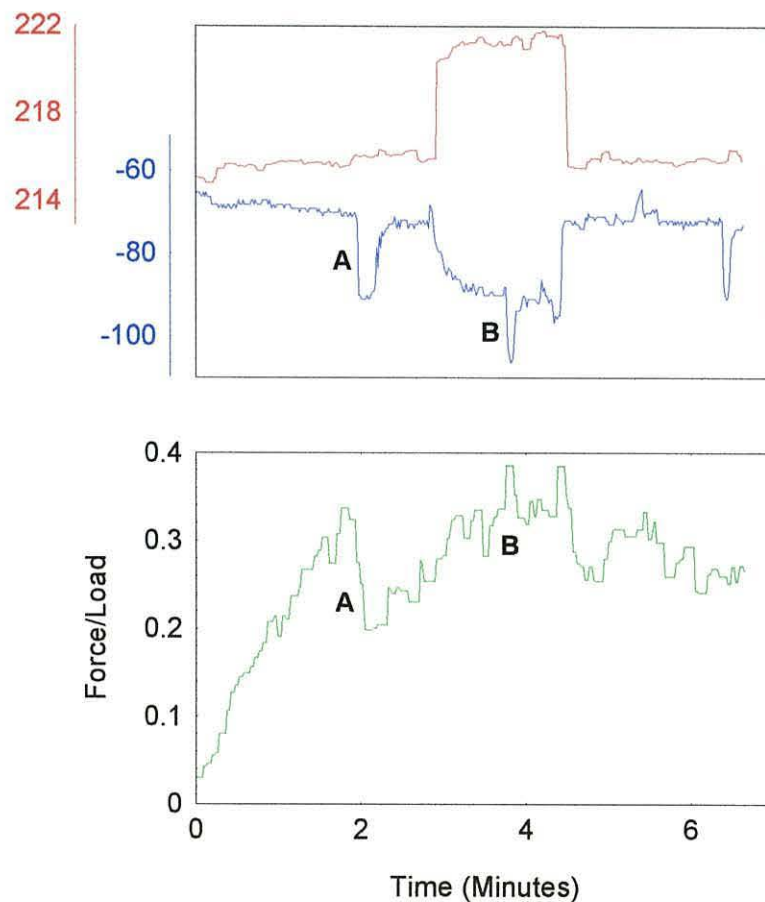


**Figure 5.29 Stick-slip type motion**

────── $\Delta f_s$ (Hz)    ────── $|Z_{min}|$ ($\Omega$)

### 5.5.4 Sliding on Dry Thiol Layers

During the experiment described in section 5.5.2 (Figure 5.26) $\Delta f_s$ responded to the shearing and dropped by about 6 Hz as the surfaces wore in. In order to study the effect of a boundary lubricant on the wearing-in process these crystals were separated at the end of the experiment and the top crystal was immersed in a 2 mM solution of decane thiol in ethanol for one hour and allowed to dry out. The crystals were then brought back together with a normal load of 10 g and the surfaces were sheared at a speed of 0.5 $\mu$m s$^{-1}$, the traces are shown in figure 5.30. $\Delta f_s$ dropped by 57 Hz, a much greater drop than wearing-in produced, due to thiol being transferred from the top crystal onto the clean sensor crystal. In contrast to wearing-in, $Z_{min}$ falls along with $\Delta f_s$. Since the change in $Z_{min}$ is small compared to $\Delta f_s$ the accumulated material can be
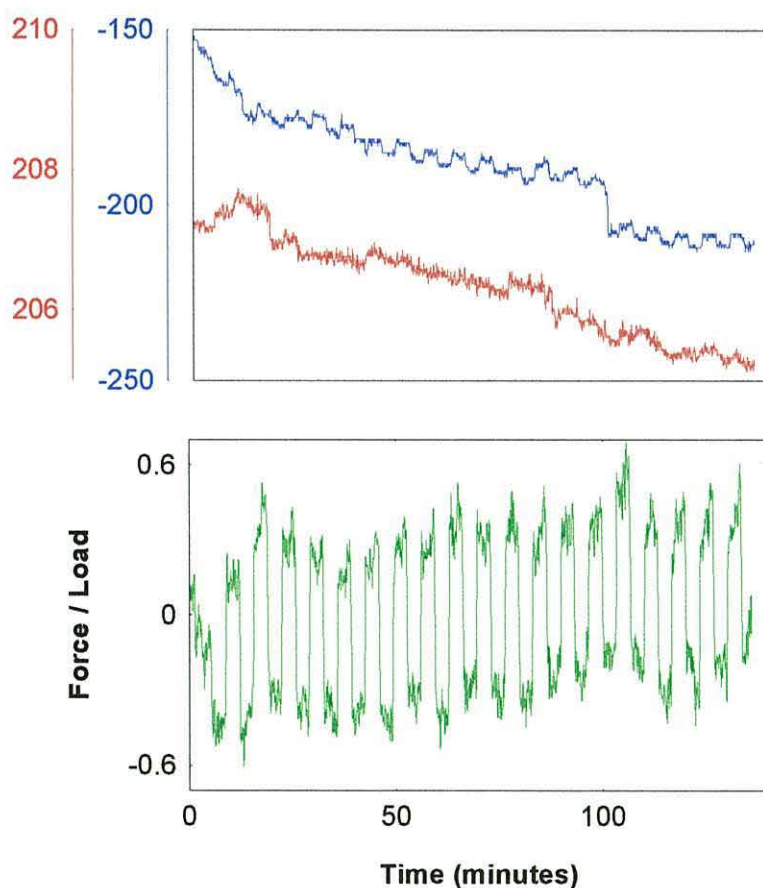


**Figure 5.30 Transfer of thiol from the top crystal to the sensor crystal**

——————— $\Delta f_s$ (Hz)  ——————— $|Z_{min}|$ ($\Omega$)

treated as a Sauerbrey type layer (see section 3.3.4), the density of the layer is $2.60 \times 10^{-6}$ Kg m$^{-2}$ which is equivalent to $8.981 \times 10^{18}$ molecules of decane thiol per square meter. During this experiment the friction coefficient remains fairly constant at 0.29.

### 5.5.5 Effect of Normal Load

As experiments are conducted with varying normal load it is necessary to study the response of the sensor to changes in the normal load applied to the surface. Figure 5.31 illustrates the response of a sensor which is in contact with a matching crystal. Both surfaces have ODT adsorbed onto them. The normal load was increased from zero to 50 g and back to zero, the experiment was then repeated with the load going up to 70 g.

It is expected that changing the normal load should not affect the friction coefficient of the surfaces. In order to check this the static and dynamic friction coefficients, $\mu_s$ and $\mu_d$ respectively, were measured at a variety of normal loads. For each load the crystals were brought into contact and the normal load applied. After a short pause the surfaces were sheared at a sliding speed of 0.125 $\mu$m s$^{-1}$ for a distance of 50 $\mu$m, left stationary for a minute and then sheared back to the starting position and separated. The strain gauge output was recorded and the static friction coefficient was determined by
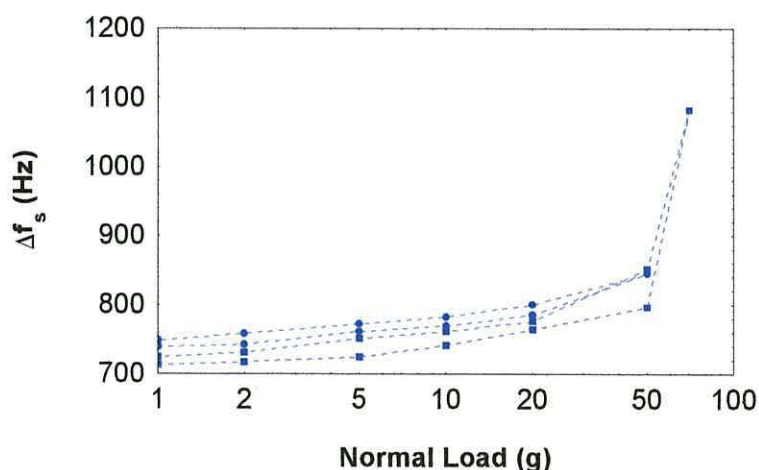


**Figure 5.31 Response of sensor to normal load applied to top crystal**

measuring the point at which sliding starts, the dynamic friction coefficient was determined by averaging the strain gauge output over the time in which sliding took place. The results, tabulated below, show that with a normal load of 20 g or above the friction coefficients are independent of load, below this load the coefficients are increased.

| Load g | $\mu_s$ | $\mu_d$ |
|--------|---------|---------|
| 5      | 0.52    | 0.2     |
| 10     | 0.3     | 0.2     |
| 20     | 0.19    | 0.1     |
| 30     | 0.17    | 0.11    |
| 50     | 0.2     | 0.15    |
| 60     | 0.17    | 0.14    |
| 70     | 0.17    | 0.13    |

### 5.5.6 Sliding under Liquid

A new pair of crystals was assembled using an epoxy resin (Araldite) as the adhesive and sealant, because it is easier to apply than the silicone rubber compound and is likely to hold the sensor more rigidly.

The surfaces were sheared using a motional amplitude of 200 μm at a speed of 1 μm s$^{-1}$ with a normal load of 20 g. The friction was initially high and fell steadily in the first part of the experiment, see figure 5.32. After 50 minutes the sensor cell was filled with iso-propyl alcohol (IPA), this caused the friction to rise steadily for the remainder of the experiment. It is possible that the IPA is removing a layer from the surface, perhaps a grease or water layer picked up from the atmosphere. Adding ethanol to the cell during a dry sliding experiment also has the effect of slightly increasing the friction. In contrast, when the alcohol is replaced by a solution of decane thiol in ethanol the friction begins a marked descent, illustrated in figure 5.33, indicating that a layer of thiol is forming between the two surfaces and reducing the friction.
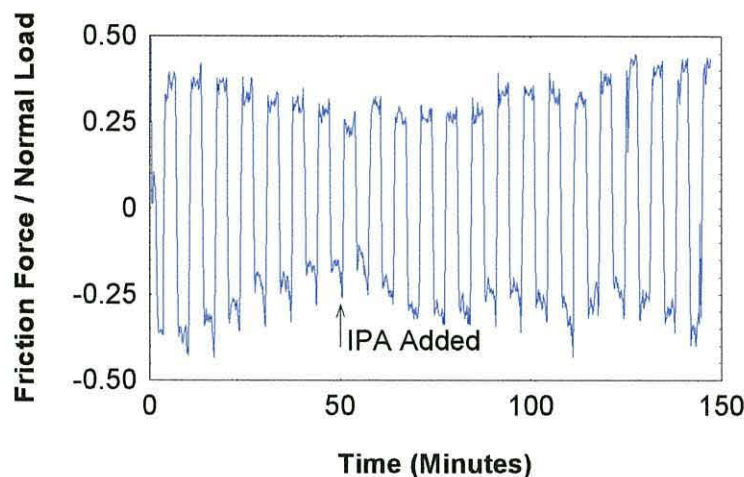
**Figure 5.32 Effect of iso-propanol on clean surfaces**
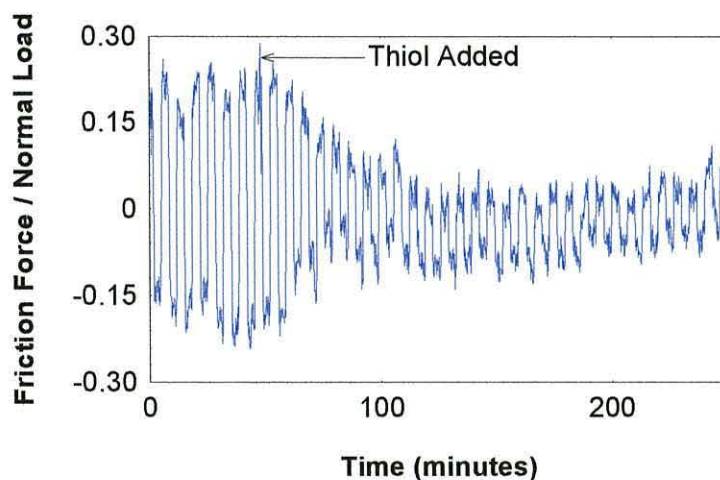


**Figure 5.33 Effect of thiol solution on clean surfaces**

### 5.5.6.1 A Study of Four Lubricants

Four lubricants were tested in order that a comparison may be made between them.

### Octadecane Thiol

A layer of octadecane thiol was formed by immersing gold coated crystals in an 0.5 mM solution of ODT in ethanol. Two planner crystals were mounted upon the tribometer and sheared backwards and forwards over a distance of 100 um with a normal load of 20 g. The speed was initially 0.125 $\mu$m s$^{-1}$ and was stepped up to 4 $\mu$m s$^{-1}$. The results are illustrated in figure 5.34.

# 5 Results

## Decane Thiol

Decane thiol was adsorbed from a 1 mM solution in ethanol onto a planar sensor crystal and a plano-convex counter crystal. With the cell immersed in the thiol solution the surfaces are sheared over a distance of 100 μm with a load of 20g, see figure 5.35. The speed is initially 0.125 μm s$^{-1}$ and is stepped up to 4 μm s$^{-1}$.

## Octanoate

The crystals used here were coated with 500 Angstroms of chromium. A 0.06 M solution of octanoate was prepared. The solution had a pH of 10.5, achieved by adding small amounts of sodium hydroxide and then hydrochloric acid until the correct reading was measured on a pH meter. The friction of the surfaces under the octanoate solution was measured using the tribometer. The shear wave parameters were measured using an impedance analyser (Hewlett Packard HP4294A) because the ionic solution proved incompatible with the oscillator. Friction was measured over a track of 100 μm with a normal load of 20g, illustrated in figure 5.36.

## Oleate

The oleate was made up as a 0.06 M solution (twenty times the critical micelle concentration ) with a pH of 10.5. The oleate adsorbed onto chromium plated crystals which were then mounted into the tribometer cell. The sensor crystal was planar and the counter crystal plano-convex. As with the other three lubricants the surfaces were brought into contact with a 20g normal load and sheared over a distance of 100 μm at various speeds. These results are illustrated in figure 5.37

### 5.5.7 Effect of Shear Waves on Friction Force

An experiment is carried out to ensure that the shear waves do not affect the friction process. The tribometer cycles over a track of 200 um at a speed of 1 μm s$^{-1}$ with a normal load of 10g. The power to the oscillator is switched on and off during this run with no visible effect on the friction record. This leads to the conclusion that the shear waves do not affect the friction process.
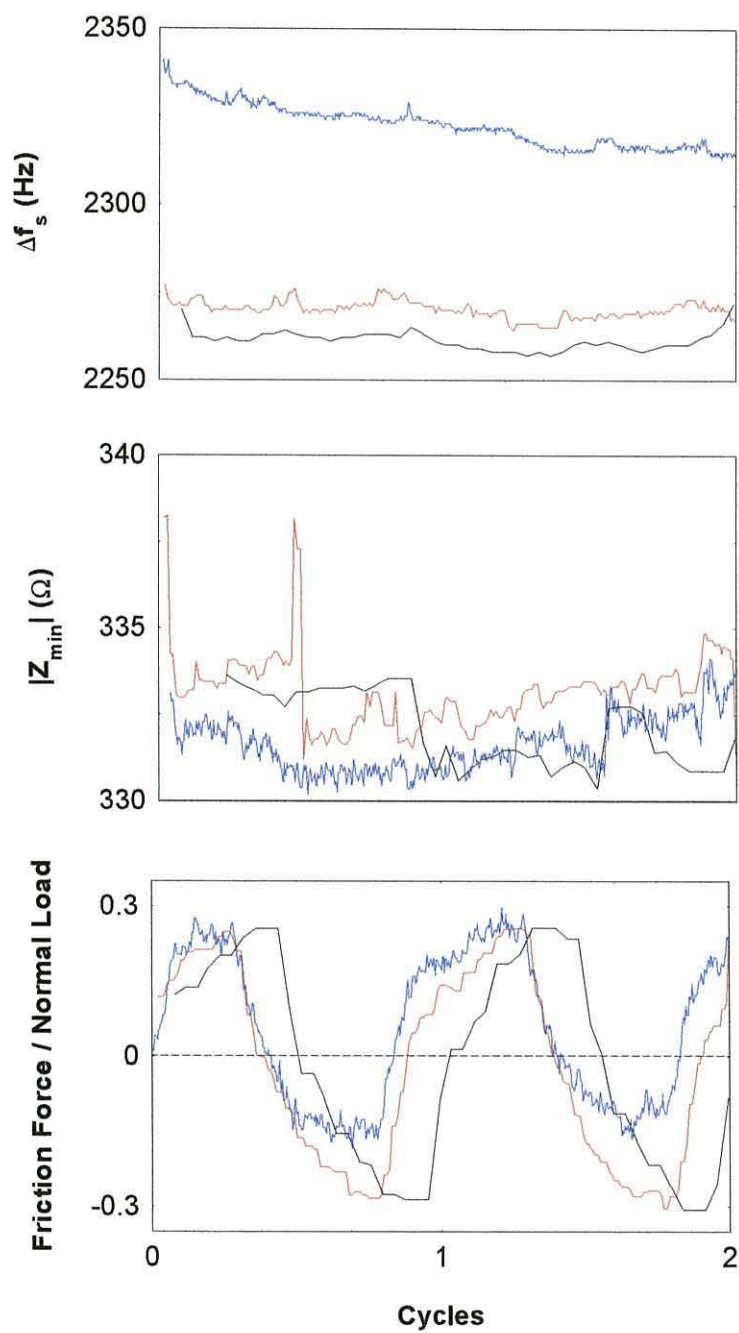
**Figure 5.34 Shearing ODT Layers**

Shearing rates μm s$^{-1}$

| | |
|---|---|
| ———— | 0.125 |
| ———— | 1.0 |
| ———— | 4.0 |
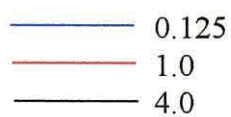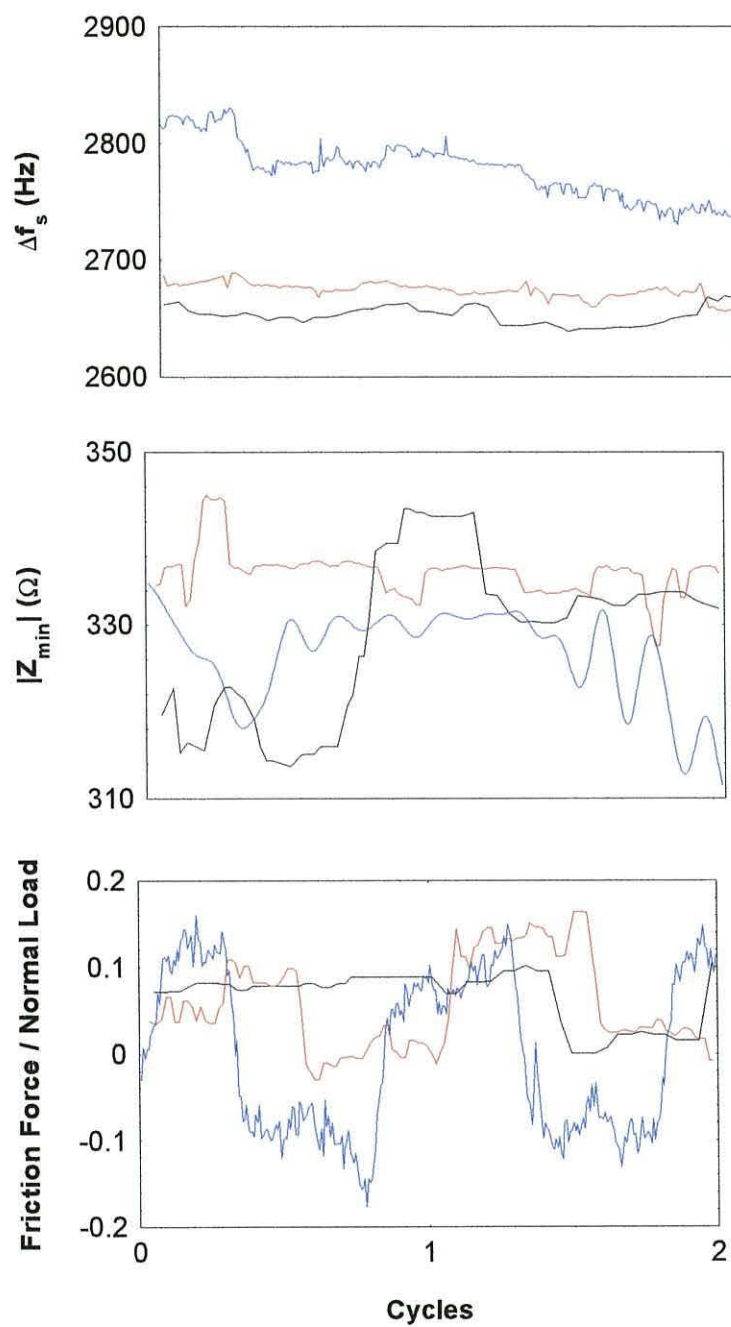
**Figure 5.35 Shearing Decane Thiol Layers**

Shearing rates $\mu m\ s^{-1}$

| | |
|---|---|
| ——— | 0.125 |
| ——— | 1.0 |
| ——— | 4.0 |
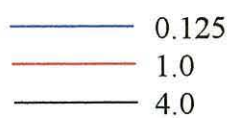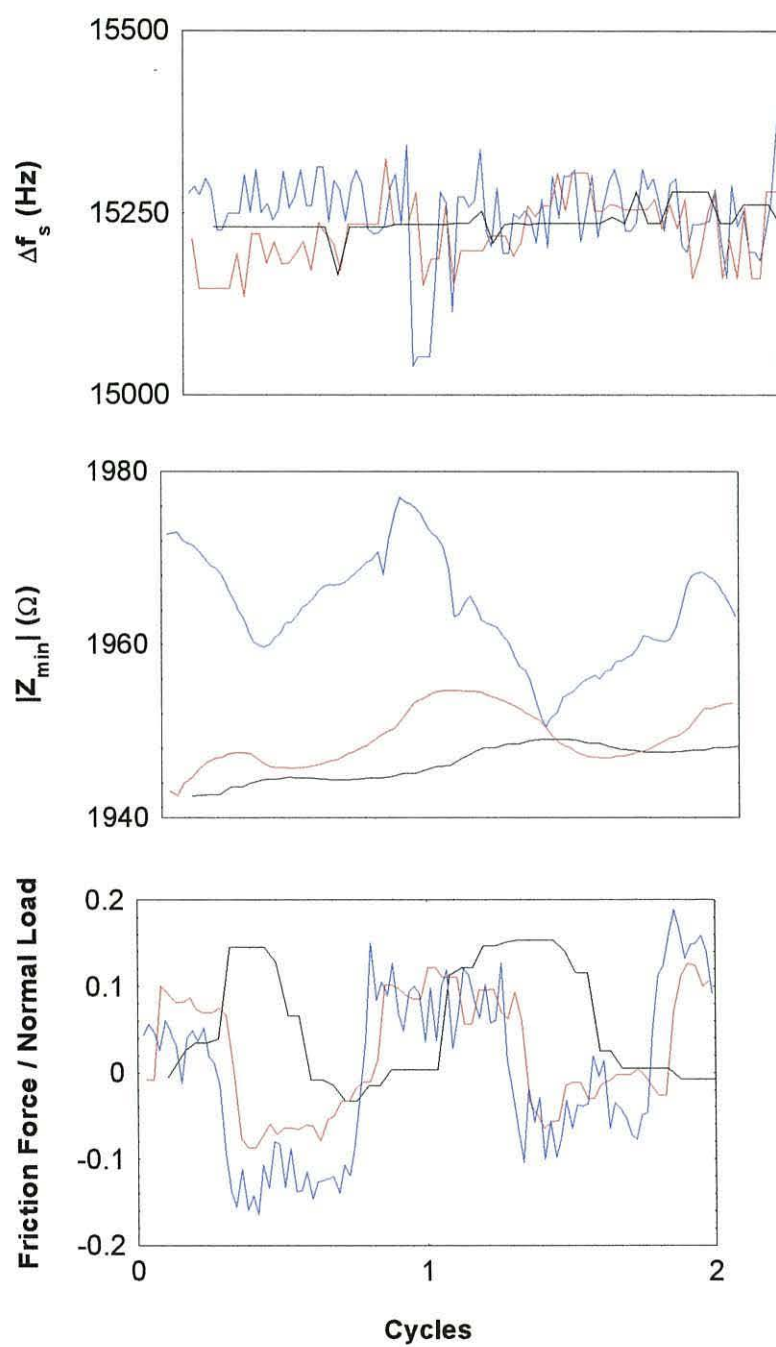
**Figure 5.36 Shearing Octanoate Layers**

Shearing rates $\mu m\ s^{-1}$

| | |
|---|---|
| ——— | 0.125 |
| ——— | 1.0 |
| ——— | 4.0 |
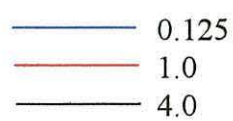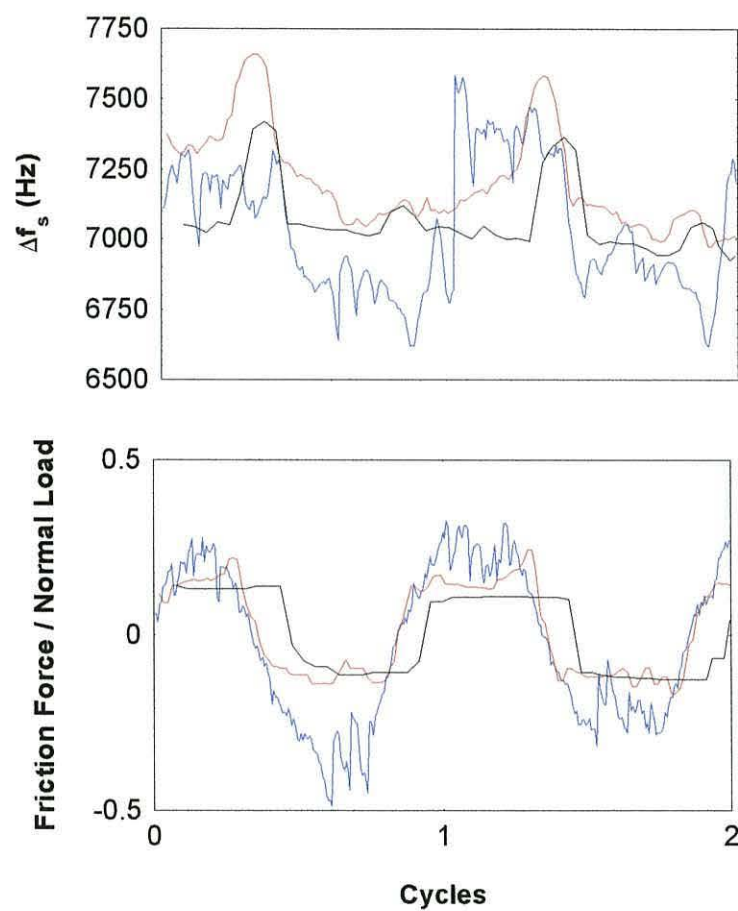
**Figure 5.37 Shearing Oleate Layers**

Shearing rates $\mu m\ s^{-1}$

| | |
|---|---|
| ———— | 0.125 |
| ———— | 1.0 |
| ———— | 4.0 |
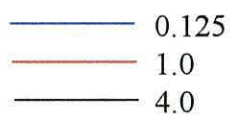
# 6 Discussion

## 6.1 The Compression of Thin Liquid Films

Several aspects of the shear wave responses described in section 5.1 call for further discussion. At point B in figure 5.2 the water droplet is spread across the whole surface and the response becomes close to that which would be expected if the sensor were loaded with a semi-infinite water layer. At point C the response is close to that expected for a sensor loaded only by air. This observation supports the hypothesis, outlined in chapter 3, that a quartz crystal with dimensions close to those of the sensor crystal should present little or no acoustic load. Mathematical modelling of the effect of a matching crystal illustrates this theory.

### 6.1.1 The Matching Crystal

The crystals used in this work had a range of thicknesses and each produced a slightly different resonant frequency. It must be shown that a small difference between the thicknesses of the sensor and the matching crystal does not significantly affect the measurements. The results of a mathematical model of a sensor loaded by a matching crystal of varying thickness is shown in figure 6.1. The matching crystal was treated as a simple elastic load which is not piezo-electrically stiffened and produced a small change in the frequency of the sensor which remains constant over the course of an experiment and can be neglected. The additional impedance offered by the quartz is less than an ohm and can also be neglected.

In the investigation of thin liquid films with the matching crystal shear waves are efficiently reflected at the quartz-air boundary (Shutilov 1988) allowing shear wave resonances to be set up in the liquid layer (figure 5.3a). In this situation a matching crystal with exactly the same resonance frequency as the sensor will reflect the shear waves most efficiently. A small difference between the resonance frequencies of the sensor and matching crystals would affect the efficiency with which the shear waves are transmitted and thus the magnitude of the frequency changes associated with the resonances in the layer but the layer thicknesses at which the resonances occur would
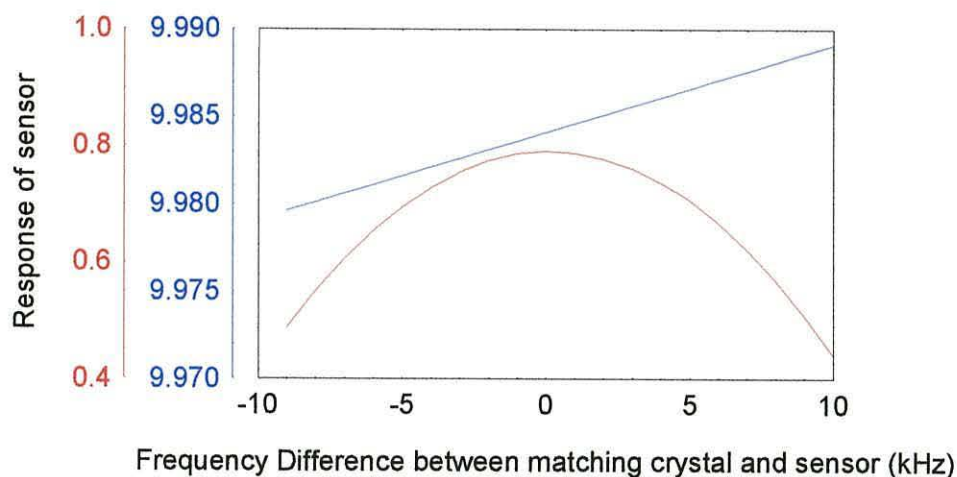
**Figure 6.1 Effect of matching quartz crystal on a sensor**

———— Resonance frequency (MHz)

———— Modulus of impedance ($\Omega$)

not be affected. The matching crystal produced small changes in response when sheared over the sensor in tribometer experiments indicating that it is an appropriate material for forming a friction surface in this investigation.

### 6.1.2 Falling Crystal

Experiments have shown that the matching (top) crystal first falls as the layer thins. After reaching some minimum thickness the liquid layer breaks up and during break up the top crystal rises. The experimental results are summarised in figure 6.2. The dielectric studies give a value for the minimum approach of the surfaces in water as 52 µm. Since the permittivity of the commercial lubricant is unknown the dielectric measurement gives no indication of the minimum separation of the crystals with a lubricant layer but only the final separation after the layer had broken up. This value can be combined with the relative movement recorded with the laser stylus to give an estimate for the minimum thickness of the lubricant layer as 20 µm.

| Change in Resonant Frequency ... Time |
| --- |

| Top crystal falling | Liquid film breaking up |

| Separation, s | | | | | | |
| --- | --- | --- | --- | --- | --- | --- |
| Water Dielectric | ±0.5 | 120.5 | | 52 | | 67.1 |
| Lubricant Dielectric | ±0.5 | | | | | 25.4 |

| Movement (Lubricant) | | | | | |
| --- | --- | --- | --- | --- | --- |
| AFM | | -57.7 | | | |
| Shear wave resonances | | At least 35 | | | |
| Laser | ±0.1 | -63.5 | | 5.3 | |

| Combining laser and dielectric | 83.6 | | 20.1 | |
| --- | --- | --- | --- | --- |
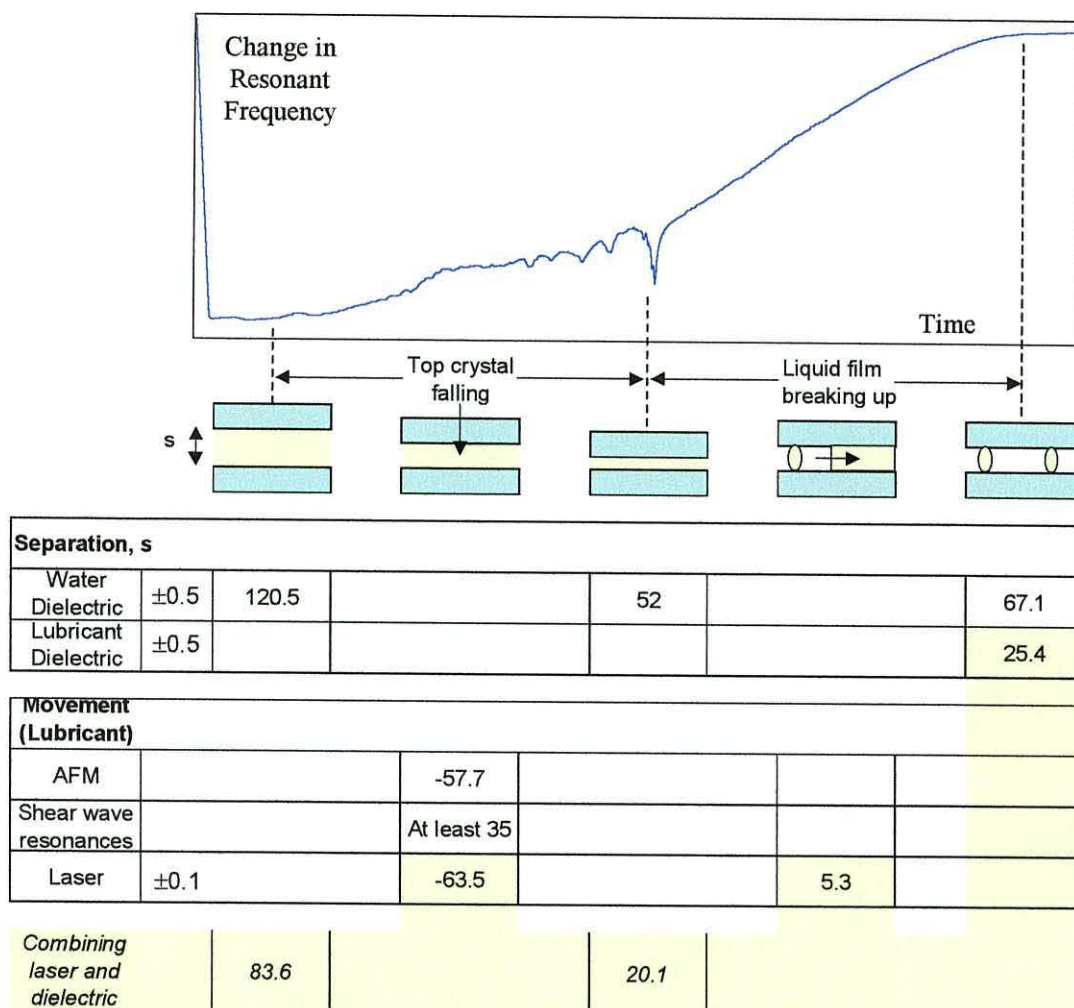
**Figure 6.2 Movement of top crystal as a thin liquid layer is compressed**
(All measurements in μm)

The shear wave attenuation coefficient, $\alpha$, in water is $3.5 \times 10^{6}\,\text{m}^{-1}$ giving a decay length, $\alpha^{-1}$, of 0.29 μm. This means that the shear waves will be completely absorbed in the water if the water layer is more than a few μm thick. In the lubricant the situation is different. The oscillations observed in the shear wave record indicate that the shear wave impedance is dependant upon the thickness of the layer and therefore a significant portion of the shear wave energy must propagate as far as the top surface of the liquid. The lubricant film is observed to be thinner than the water layer when it breaks up, but even so shear wave attenuation in the lubricant must be significantly less than that in water. Mathematical modelling showed that oscillations of the kind observed could be produced in a layer as thick as 20 μm when the attenuation
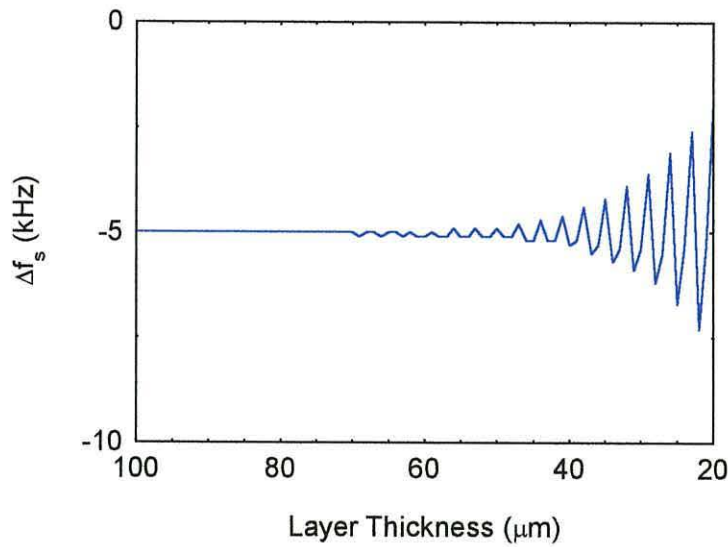
**Figure 6.3 Response of sensor to a water layer bounded by a matching quartz crystal as the layer thickness decreases.**

coefficient was $5.5 \times 10^4 \, \text{m}^{-1}$. The results are illustrated in figure 6.3 and the calculation is presented in the appendix. In this model the thickness of the matching crystal is equal to that of the sensor crystal. If the thickness of the matching crystal is changed then the size of the oscillations in the response is affected but not the number of oscillations or their position. In experiments the oscillations cease when the top crystal stops falling and the film begins to break up.

### 6.1.3 Rising Crystal

The rise of the top crystal as the film breaks up is attributed to the action of small residual droplets of liquid which are capable of lifting and supporting the crystal.

The droplets establish a shape which minimises the surface energy, the work done in raising the top crystal is thus derived from a reduction in the total surface energy.

Consider a droplet with a major radius, $r_1$, in the plane of the crystal surface and a minor radius, $r_2$, perpendicular to the surface, as illustrated in figure 6.4. A pressure difference will exist across the liquid-air interface (Newman 1950) which is given by
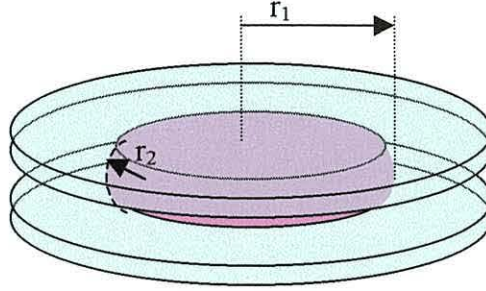
**Figure 6.4 Representation of a liquid droplet identifying**

**the dimensions $r_1$ and $r_2$**

$$\Delta p = \gamma \left[ \frac{1}{r_1} + \frac{1}{r_2} \right]$$

where $\gamma$ is the surface energy, in the case of water this is 0.07197 N m$^{-1}$. The circular

contact between the droplet and the top crystal has a radius, $r_i$, which is given by

$$r_i = r_1 - \left( r_2 - \sqrt{r_2^2 - s^2/4} \right)$$

where s is the distance separating the two crystals. Thus the area, A, of the contact is

$\pi r_i^2$. If the separation of the crystals is much smaller than $r_2$ then the contact area will

be approximately equal to the cross sectional area of the droplet, $\pi r_1^2$. The droplet will

exert a force upon the top crystal given by

$$F = \Delta p\, A$$

If the crystal is supported upon n droplets of identical dimensions the upward force can

be written as

$$F = n \pi r_1^2 \gamma \left[ \frac{1}{r_1} + \frac{1}{r_2} \right]$$
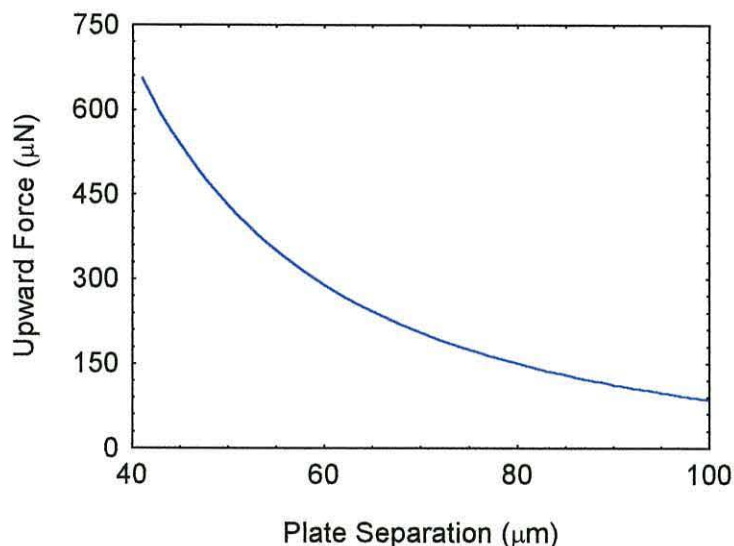
**Figure 6.5 Dependence of the upward force produced by a droplet of water between two gold surfaces on the separation of the surfaces**

Volume of droplet: $8.1 \times 10^{-12}$ m$^3$
Contact angle: $90°$

Figure 6.5 shows the results of a simulation of a single droplet with a volume of $8.1 \times 10^{-12}$ m$^3$ making a $90°$ contact angle with the gold surfaces. The upward force produced by the droplet increases with decreasing separation of the surfaces such that an equilibrium can be reached where the upward force equals the weight of the top crystal. Experimental observations showed approximately 20 droplets of varying sizes and the upward force balancing the weight of the top crystal would in fact be distributed among all of them.

## 6.2 Adsorption Effects

The lubricants tested were all shown to adsorb onto the electrodes of the crystals. The final separation of the crystals after compression of liquid lubricant was lower than that observed with water because the contact angle of the lubricant with the gold is less than that of water.

Measuring the adsorption of two different alkane thiols produced an interesting result. Although octadecane thiol with a molecular mass 286 is the larger molecule, it is

decane thiol with a molecular mass of 174 which produced the largest effect. Figure 5.16 shows the results of two adsorption experiments. The adsorption of octadecane thiol produced a change in frequency of 36 Hz which is equivalent to a mass loading of one monolayer. The frequency change due to adsorption of decane thiol was 280 Hz which is equivalent to a mass loading of nearly ten monolayers. Multilayer adsorption of thiols has been observed (Kim 1993).

The presence of a multilayer of decane thiol is reflected in the behaviour observed in section 5.5.4 where there is clear evidence that during shearing some of the multilayer of thiol is transferred from the matching crystal to the sensor. The results illustrated in figure 5.30 show that after 100 minutes of sliding the density of the thiol layer transferred onto the clean surface was $8.81 \times 10^{18}$ molecules m$^{-2}$, equivalent to nearly two monolayers.

## 6.3 The Effect of Normal Load

The result of a cyclically changing normal load applied to the film which remains after a thin liquid layer has broken up is described in section 5.3. Initially there is a response in X but not in R. After standing for one hour there is a response in R but not in X. Analysis of the residual droplets shows that the separation of the crystals is set by the normal load which is exerted by the top crystal. When the normal load is increased the droplets become compressed as the crystals are brought together. Figure 6.6 shows the results of modelling a thin water layer which covers 6% of the surface of the sensor and is bounded by a matching crystal having the same thickness as the sensor. Close to point A the value of R has no dependence on layer thickness while the value of X is approximately proportional to the layer thickness. Small cyclic variations around this point would produce the response seen in figure 5.18a. If the thickness of the film is increased to point B then it is X which has no dependence on layer thickness while R is proportional to thickness, small cyclic variations here would produce the response seen in figure 5.18b. The thickness of the film appears to have increased slowly over time, but it is difficult to see why this should be so. It implies that the supporting droplets are
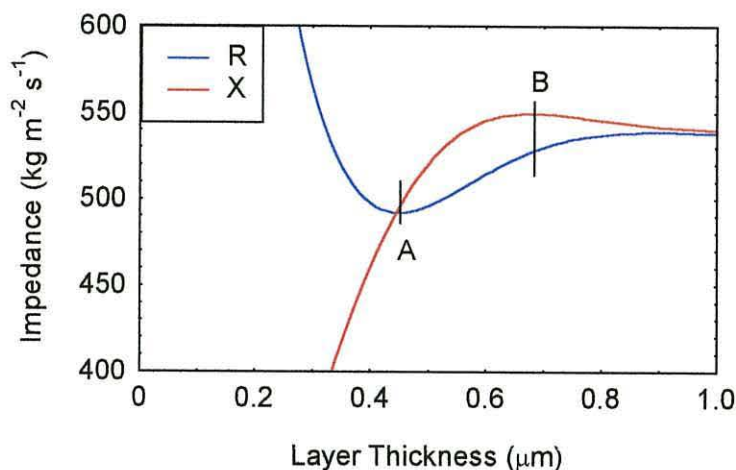
**Figure 6.6 Impedance of a thin water layer bounded by
a quartz crystal**

slowly changing shape due perhaps to droplet reorganisation accompanying evaporative loss.

The microdrive experiment described in section 5.1.4 also indicates that the acoustic response changes with film thickness. It is possible that the s-shaped curve illustrated in figure 5.12 is due to a changing resonance condition in the layer but, since the distance involved is greater than a shear wave half-wavelength and shorter than a compression wave half-wavelength it is more likely that droplets are squeezed and stretched as the surfaces move, thereby changing the area of the sensor which is contacted by the liquid.

## *6.4 Tribometer*

### 6.4.1 Ruby Sphere

A ruby sphere was used to investigate the way in which the sensor crystal responds to a mechanical load. The ruby makes a well-defined and repeatable contact with the sensor surface. This makes it ideal for studying the effect of the position of a load on the response of the sensor. The normal load is controlled by applying weights to the probe of the tribometer and this load remains constant as the ruby is moved over the

surface of the sensor. The radius of contact can be estimated using the Hertz theory of elastic contact (Hertz 1882). The radius is given by

$$r = \left( \frac{3PR}{4E^*} \right)^{\frac{1}{3}}$$

where P is the load, R is the radius of the ruby and E$^*$ is the effective elastic modulus given by

$$E^* = \left( \frac{1-v_r^2}{E_r} + \frac{1-v_g^2}{E_g} \right)^{-1}$$

$E_r$, $v_r$, $E_g$ and $v_g$ are the Young moduli and Poisson ratios of ruby and gold respectively. These values are $78 \times 10^9$ N m$^{-2}$ and 0.43 for gold and $3.52 \times 10^9$ N m$^{-2}$ and 0.3 for ruby. Thus a load of 10 g should produce a circular contact with a diameter of 117 μm.

The AFM image of the damage caused by sliding the ruby over the gold surface is shown in figure 5.22b. This confirmed that the ruby had traversed the surface in a straight line with a constant width of 62 μm which is about half the value of the estimated contact diameter. The most likely reason for this is that the contact pressure is not constant over the area of contact but is greater in the centre. Thus it is possible that the region of the contact where the pressure was sufficient to irreversibly deform the surface had a diameter of 62 μm while over the remainder of the contact area the pressure caused elastic deformation only.

Although the surface is scratched by the ruby the deformation is not sufficient to permanently alter the response of the crystal sensor. When the load is removed the resonant frequency of the crystal returns to its unloaded value and when the ruby is slid backwards and forwards over the same track the response is entirely repeatable. The sensor responds to the mechanical contact but is not permanently affected by the process principally because the deformed area is very much smaller than the total active area. The response of the sensor to the ruby is illustrated in figures 5.21 and 5.23. The shape of the response as the point of contact is moved over a diameter of the

sensor approximately follows the Bessel function described in section 3.3.1. This shape of response has also been found by dragging a tungsten wire across the surface (Martin 1989b), electrochemical deposition of small, localised masses (Hillier 1992) and by depositing small dots of ink at points on the surface using a permanent marker pen (Cumpson 1990). Cumpson and Seah account for this profile by showing that the response of the sensor to mass loading is proportional to the square of the particle velocity at the point where the mass is deposited.

An interesting feature of the response is that the change in resonant frequency, $\Delta f_s$, is positive relative to the resonant frequency of an unloaded crystal whereas most acoustic loads produce a negative frequency shift. Martin and Hager's measurement with the tungsten wire also produced a positive frequency shift when the wire was brought into contact with the surface. They attribute this to the wire acting as a spring and stiffening the resonating system. In the case of the ruby, however, there is evidence that this effect is the result of higher frequency modes of resonance which are excited when the ruby contacts the surface.

Superimposed over the profiles depicted in figures 5.21 and 5.23 there is a cyclic variation with 4 nodes between the centre and the electrode edge. This variation is seen most clearly in the curve for $|Z_{min}|$ but is also present in $\Delta f_s$. The most likely explanation for this is that there is mechanical coupling to a higher frequency mode of the resonator in which the surface wave intensity exhibits a number of nodes across the surface. In section 3.3.1 it was shown that the wave intensity at the surface of a cylindrical resonator is dependent upon distance, r, from the centre of the surface and is given by the Bessel function

$$U_S = J_n(k\,r)$$

The solution to this equation is found by assuming that the wave intensity has a single node at the electrode edge. This produces the Bessel shape which is dominant in these figures. In fact other modes are possible where there are a number of nodes across the electrodes. The response to the ruby exhibits at least two different modes of oscillation. The fundamental frequencies of these two modes can be found by

substituting for $k_{nm}$ in equation 3.4 the terms $k_{01}R=2.4$ and $k_{25}R=17.96$. These yield the values $f_{101}=10.012857$ MHz and $f_{125}=10.696238$ MHz. The second order Bessel function which accounts for the cyclic variation in the response has the higher frequency. If this mode is induced by the presence of the ruby then the measured frequency would be the result of coupling between these two modes giving the positive frequency response observed. In figure 6.7 the response to the ruby is compared to $J_s$ the sum of two Bessel functions where

$$J_s = J_0(k_{01}r) + J_2(k_{25}r)$$

The profile in figure 5.23 is interrupted at point X by microscopic debris on the sensor surface. The balance arm of the tribometer is pivoted, allowing the probe to move freely in the direction normal to the surface. As the ruby is moved across the surface it comes into contact with the debris and rides up over it as illustrated in figure 6.8. As the ruby moves over the debris it is out of contact with the surface, however, the normal load applied to the surface remains constant. The effect of debris on the surface is to reduce the response at that point. This shows that the response is not purely the
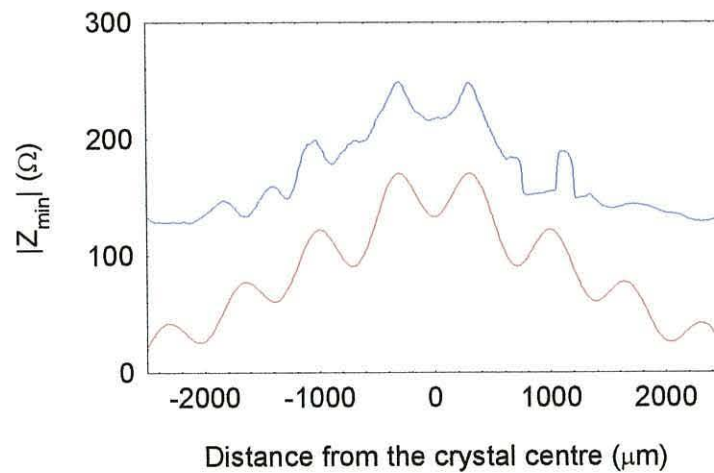


**Figure 6.7 Comparison of the actual response of the sensor with the sum of two Bessel functions.**

——————  Response observed experimentally

——————  $J_s$ the sum of two Bessel functions (arbitrary units)
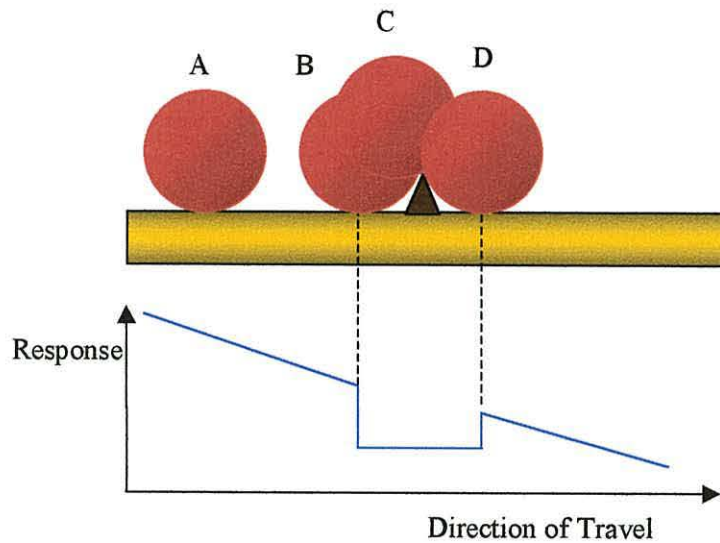
**Figure 6.8 Effect of surface debris on response**

A ruby in contact with surface.
B ruby makes contact with debris and begins to lift off surface.
C ruby rides over debris particle.
D ruby regains contact with surface.

effect of a macroscopic point load but that the ruby itself becomes part of the resonating system. In figure 5.23 the gap in the response is well-defined making it possible to crudely estimate the height of the debris particle by assuming it to be conical. The ruby begins to lift of the surface when it first makes contact with the tip. Since the radius of the ruby is known and the width of the gap can be measured, simple trigonometry can be used to derive the height of the particle. The height of the piece of debris is estimated to be 4.5 $\mu$m based on the width of the gap in the response to the 50 g load. AFM imaging of the surface revealed a particle with a height of approximately 3.9 $\mu$m which is in close agreement with the calculated height. The gap was observed to decrease as the normal load was increased indicating that the debris was compressed by the ruby.

Sliding the ruby across the surface and recording the shear wave parameters while the ruby was in motion produced the same response as the stationary contact at a series of points. This shows that the sensor is only responding to the mechanical contact of the

ruby and not to the sliding process. This result indicates that when a matching crystal is brought into contact with the sensor crystal the sensor will respond to mechanical contact and not to the process of sliding.

### 6.4.2 Wearing-in of surface contacts

When the ruby is replaced by a matching crystal $\Delta f_s$ is negative rather than positive because there is no longer any coupling to the higher frequency modes. The fall in resonant frequency and impedance as the scan is repeated, figure 5.24, is clear evidence of the wearing-in process because it indicates that the acoustic contact between the surfaces is increasing as they are slid over one another. Most of the wearing-in takes place in the reverse direction suggesting that, although every effort was made to assemble the crystals parallel to each other, the mechanism of the shearing is asymmetric and consequently the surfaces experience a greater load in one direction. Even after the initial wearing-in process is complete the shear wave response depends upon the direction in which the crystals are sheared.

This asymmetry is clearly visible in figure 5.24 where the response exhibits step changes each time the direction of motion changes. Both the asymmetry and the wearing-in process are also clear in figure 5.25. $\Delta f_s$ shows a downward drift in the first part of the trace and then exhibits only the step changes associated with changes in the direction of motion. The friction force is initially low, increases while $\Delta f_s$ drifts and then remains constant. It is likely that a thin layer of moisture and airborne detritus deposited onto the surface from the surrounding atmosphere is responsible the initial low friction and this layer is rapidly worn away during the first part of the experiment.

### 6.4.3 Static Friction

The static friction experiments (section 5.5.3) showed that the sensor responds to movement of the tribometer stage even when the surfaces are sticking. For example, in figure 5.28 there is a response in $\Delta f_s$ (point P, figure 5.28) while the surfaces are stuck. This is likely to be due to changes in the distribution of the normal load. In figure 5.29 there are step changes in $\Delta f_s$ (points A and B, figure 5.29) which corresponds to

slipping of the surfaces. However these responses are not repeatable. Thus, although the quartz crystal appears to be sensitive enough to detect sliding, the necessary reproducibility cannot be achieved under the present experimental conditions.

### 6.4.4 Boundary Layer Lubrication

The shear wave sensor is clearly able to detect the formation of boundary layers. Layers of thiols have been observed to form both from solution and also during dry sliding. The results in section 5.5.4 clearly showed the formation of a layer of decane thiol on the sensor as it is sheared against a gold surface bearing a thiol multilayer.

Shearing the surfaces under solutions of boundary lubricants failed to yield any observable changes in the viscoelastic properties of the layers during shear (section5.5.6.1). The response of the sensor to sliding was small and did not show much repeatability. It appears that because the boundary layers are thin, typically a few nm, changes in their acoustic impedance are too small to be detected under dynamic conditions using the quartz crystal sensor. Mathematical modelling confirmed that at such thicknesses the attenuation of the acoustic wave within the layer is negligible and there is effectively no acoustic loss.
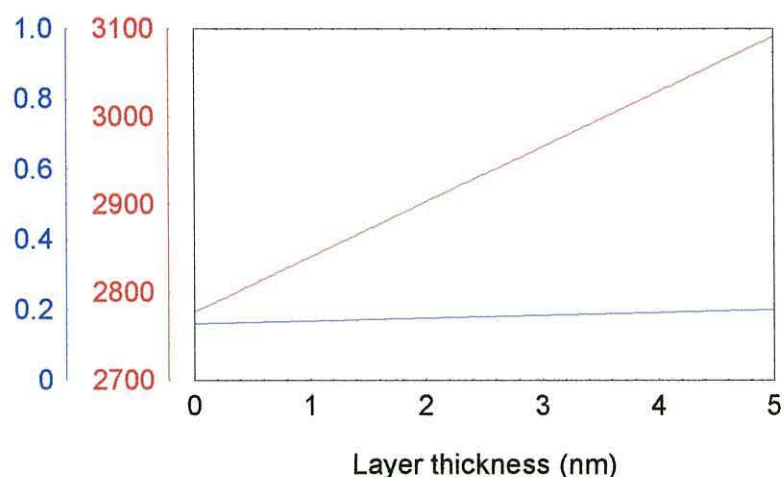


**Figure 6.9 The dependence of acoustic response on the thickness of a confined layer**

————— R (kg m$^{-2}$ s$^{-1}$)          —————X (kg m$^{-2}$ s$^{-1}$)

A layer confined between a sensor and a matching crystal was modelled at thicknesses ranging from 0 to 5 nm. The density of the layer was set at 1000 kg m$^{-3}$, the shear wave velocity at 10 m s$^{-1}$ and the shear wave attenuation at $4 \times 10^6$ m$^{-1}$. The results of this model are illustrated in figure 6.9 and show that the real part of the acoustic

(a)



Shear wave velocity (m s$^{-1}$)

(b)



Shear wave attenuation (m$^{-1}$)
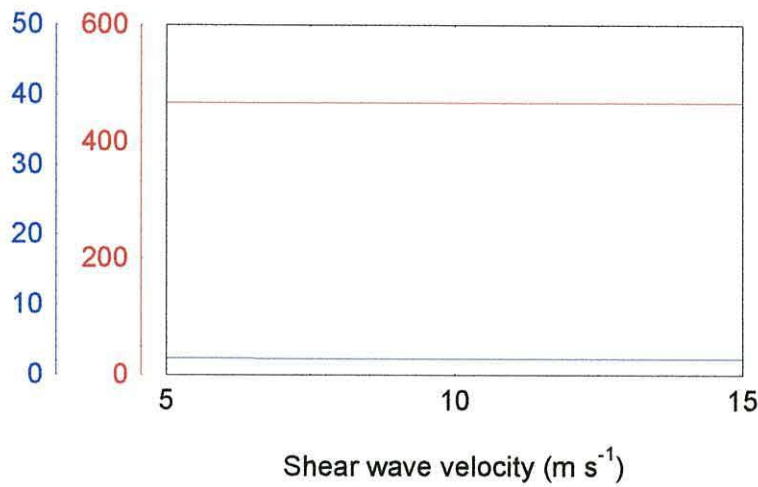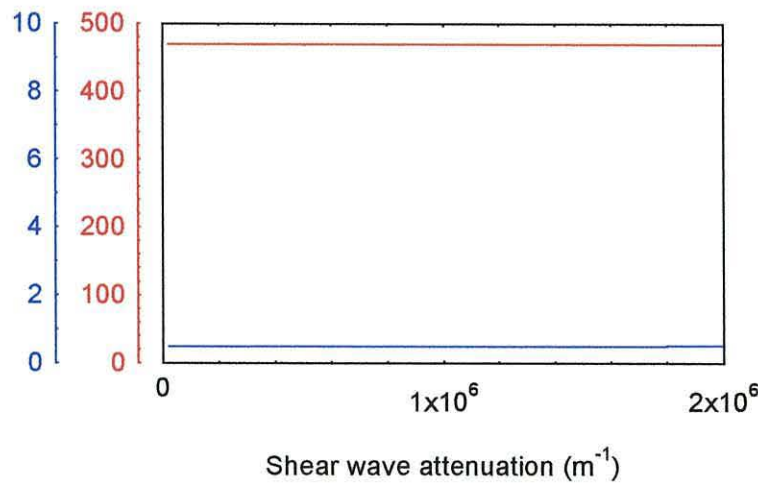
**Figure 6.10 Response of sensor to changes in the shear wave properties of a 3 nm thick layer**

(a) Varying shear wave velocity, attenuation = $4 \times 10^6$ m$^{-1}$
(b) Varying shear wave attenuation, velocity = 10 m s$^{-1}$

———— R (kg m$^{-2}$ s$^{-1}$)     ———— X (kg m$^{-2}$ s$^{-1}$)

impedance, R, is very small and does not change significantly with layer thickness. The imaginary part of the acoustic impedance, X, is proportional to the layer thickness.

The insensitivity of the quartz sensor to changes in the real part of the impedance is confirmed by modelling the effect of changes in the viscoelastic properties of a 3 nm thick layer with a density of 1000 kg m$^{-3}$. Figure 6.10a shows the results of varying the shear wave velocity while the shear wave attenuation is $4 \times 10^6$ m$^{-1}$ and figure 6.10b shows the results of varying the shear wave attenuation while the shear wave velocity is 10 m s$^{-1}$. From this it is immediately apparent that R is very small and independent of the layer parameters whereas X is significant. X exhibits dependence on mass but not on either shear wave velocity or attenuation.

The model thus predicts that a boundary layer will behave as an elastic layer exhibiting no loss. It is not possible to detect changes in the viscoelastic properties which may occur as a result of shearing. It is possible, however, to monitor the formation of boundary layers.

There is however evidence in figure 5.30 that, as the thiol layer forms, there is a small but significant reduction in R even though the layer is thin. This observation contradicts the model suggesting that the model is inadequate for such thin layers. It is possible that this change in R is the result of slippage of the adsorbed layer.

It has been observed that thin liquid films adsorbed onto the surface of a quartz crystal resonator can slip giving rise to a solid-liquid interfacial viscosity (Krim et al 1990). Very thin layers exhibit greater slippage than thicker layers. It seems likely that a reduction in slippage at the quartz crystal surface could account for the observed reduction in R.

# 7 Conclusions

## *7.1 Lubrication*

A boundary layer is typically an adsorbed molecular monolayer with a thickness of a few nanometers. Modeling of the shear wave system has shown that acoustic loss in such a small layer will be negligible and the layer will behave as a loss-free elastic layer. Thus it appears that the quartz sensor is able to detect the formation of a boundary layer but is not able to detect any changes in the viscoelastic properties of the layer which may occur under conditions of shear.

The quartz crystal sensor can monitor the process of wearing-in of surfaces as a progressive improvement in their acoustic coupling and also the effect of introducing a boundary lubricant to surfaces which are in shearing contact.

The formation of a single monolayer of octadecane thiol was clearly observed and decane thiol was observed to form a multilayer approximately ten molecules thick. Moreover, the transfer of molecules from the thiolated surface onto a clean gold surface in shearing contact was readily observed

Adsorption of thiol multilayers has previously been observed using the quartz crystal sensor (Kim 1993), however, the transfer of thiol molecules onto the sensor during dry shearing is believed to be a new observation. The process of molecular transfer may be of significance for the investigation of boundary layer lubrication in conditions where it is not possible to apply the lubricant by adsorption from bulk liquid.

## *7.2 Behaviour of thin liquid layers*

The behaviour of a liquid layer confined between two surfaces can be efficiently monitored using the sensor crystal as one surface.

As the gap between two surfaces is reduced the layer becomes unstable, breaking up into small droplets which appear to form at microscopic irregularities on the confining surfaces. Each droplet adopts a shape which minimises its surface energy and in so

doing exerts a force which acts so as to drive the surfaces apart.

Changes in distribution of a liquid film between two crystals can be sensitively detected by the quartz crystal sensor. The response of the sensor to an incomplete layer can be estimated by integrating the sensitivity function over the area of the surface which is occupied by the film.

The response of the sensor to a thin layer changes with the thickness of the layer. Some layers were shown to exhibit a number of shear wave resonances as the thickness of the layer was reduced. The microdrive experiment also demonstrated the effect of thickness upon the acoustic properties of a layer, this experiment could be refined by arranging for the surfaces to approach one another under bulk liquid thus preventing the confined layer from breaking up.

This technique may be useful in determining the stability of thin liquid films and studying the processes associated with the break-down of the hydrodynamic regime.

## 7.3 Acoustic Loads

In the course of this exploratory work the novel application of the quartz crystal shear wave sensor has led to some useful discoveries in the operation of the device.

The contact of a ruby sphere upon the surface of the sensor induced higher frequency modes of resonance which are predicted by theory (section 3.3.1) but have not previously been observed. These modes were only evident when the ruby was in good acoustic contact with the surface. When the contact of the ruby was interrupted by surface debris the response of the sensor was greatly reduced even though the normal load upon it remained constant. This technique could be used to asses the way the acoustic coupling between surfaces is affected by surface layers.

A quartz crystal with the same nominal frequency as the sensor acts as a matched acoustic load and its use has proved to be a successful technique in measuring the acoustic impedance of a thin confined layer. This may have applications in the study of hydrodynamic or transitional lubrication.

# References

Abbot and Firestone *Mech Eng* **55,** 556 (1933)

Auge, J; Hauptman, P; Eichelbaum, F and Rösler, S *Sensors and Actuators B* 18-19, 518-522 (1994)

Bain, C. D. and Whitesides, G. M. *J. Am. Chem. Soc.* **110,** 3665-3666 (1988)

Ballantine , D. S. et al *Acoustic Wave Sensors* (Academic Press London 1997)

Barnes , C.; D'Silva, C.; Jones, J. P. and Lewis, T. J. *Sensors and Actuators A.* **31,** 159-163 (1992)

Bhushan, B and Kionkar, V. N. *Tribology Trans.* **38,** 119-127 (1995a)

Bhushan, B; Israelachvili, J. N. and Landman, U. *Nature* **374,** 13 607-616 (1995b)

Bhushan, B; KionKar, V. N. and Ruan, J. *Proc. Instn. Mech. Engrs.* **208,** 17-29 (1994)

Binnig, G.; Rohrer, H.; Gerber, Ch. and Weibel, E. *Phys. Rev. Lett.* **49,** 57-61 (1982)

Binnig, G; Quate,C. F. and Gerber, Ch. *Phys. Rev. Lett.* **56,** 930-933 (1986)

Bottom, V Introduction to Quartz Crystal Unit Design Van Nostrand Reinhold, London (1982)

Bowden, F. P. and Tabor, D. *Friction and Lubrication* (Methuen, London 1967)

Bowden, F. P. and Tabor, D. *The Friction and Lubrication of Solids* (Oxford University Press 1950)

Boyd, J. and Robertson, B. P. *Trans. Amer. Soc. Mech. Engrs.* **67,** 51 (1945)

Bridgman, P. W. *Rev. Mod. Phys.* **18,** 1. (1946)

Briscoe, B. J, in *Fundamentals of Friction* ed Singer, I. L. and Pollock, H. M. (Kluwer, Dordrecht 1992)

Bruckenstein, S. and Shay, M. *Electrochemica Acta* **30,** 10 1295-1300 (1985)

Carpick, R. W.; Agrait, N.; Ogletree, D. F. and Salmeron, M. *J. Vac. Sci. Technol., B* **14,** 2 (1996)

Childs, T.H.C. *Wear,* **25,** 3 (1973)

Childs, T. H. C. in *Fundamentals of Friction* ed Singer, I. L. and Pollock, H. M. (Kluwer, Dordrecht 1992)

Cumpson , P. J. and Seah, M. P. *Meas Sci Technol* **1,** 7 544-555 (1990)

Daly, C. and Krim, *J. Phys. Rev. Lett.* **76,** 803 (1996)

Derjaguin, B. V.; Muller, V. M. and Toporov, Y. P. *J. Colloid Interface Sci.* **53**(2), 314 (1975)

Diestler, D., Schoen, M. and Cushman, J. *Science* **262,** 545-547 (1993)

Dowson, D. *History of Tribology,* second edition (Professional Engineering Publishing, London 1998)

Du, Q.; Xiao, X-d.; Charych, D. H.; Wolf, F.;Frantz, P; Shen, Y. R. and Salmeron, M. *Phys. Rev., B: Condens. Matter* **51**(12), 7456 (1995)

Fein, R. S.; Rowe, C. N.; and Kreuz, K. L. *Amer. Soc. Lubric. Engrs. Trans.* **2,** 50 (1959)

Ganti, S. and Bhushan, B. *Wear* **180,** 17-34 (1995)

Granick, S *Science* **253,** 1374-1379 (1991)

Greenwood, J. A. in *Fundamentals of Friction* ed Singer, I. L. and Pollock, H. M. (Kluwer, Dordrecht 1992)

Greenwood, J.A. and Williamson, J.B.P. *Proc. Roy. Soc.* **A295,** 300 (1966)

Hardy, W. B. *Collected Works* (Cambridge Univ. Press 1936)

Harrison, J. A.; White, C. T.; Colton, R. J. and Brenner, D. W. *Mater. Res. Soc. Bull.* **17,** 50-53 (1993)

Hertz, H. *J. reine und angwandte Mathematik* **92,** 156-171 (1882) (English Translation: Miscellaneous Papers by H. Hertz, Eds. Jones and Schott, London: Macmillan, 1896)

Hillier, A. C. and Ward, M. D. *Anal. Chem.* **64,** 2539-2554 (1992)

Hu, J; Xiao, X.-d.; Ogletree, D. F. and Salmeron, M. *Surf. Sci.* **327**(3), 358 (1995)

Hutchings, I. M. *Tribology. Friction and Wear of Engineering Materials* (Edward Arnold, London 1992)

Israelachvili, J. N. in *Fundamentals of Friction* ed Singer, I. L. and Pollock, H. M. (Kluwer, Dordrecht 1992)

Israelachvili, J.; Mcguiggan, P.; Gee, M.; Homola A, Robbins, M.; Thompson, P. *J. Phys.: Condensed Matter* **2**, SA89-SA98 (1990)

Israelachvili, J. N. and Tabor, D. *Proc. R. Soc. London* Ser A **331**, 19 (1972)

Israelachvili, J. N. and Tabor, D. *Nature* **241**, 148-149 (1973)

Johannsmann,D.; Mathauer, K.; Wenger, G. and Knoll, W. Phys. Rev. B. 46,12, 7808-7815 (1992)

Johnson, K. L. *Contact Mechanics* (Cambridge Univ. Press 1985)

Johnson, K. L.; Kendall, K. and Roberts,A. D. *Proc. R. Soc. London* Ser. A **324**, (1558), 301. (1971)

Kanazawa, K. K. *Faraday Discuss.* **107,** 5 (1997)

Kaneko, R.; Umemura, S.; Hirano, M.; Andoh, Y.; Miyamoto, T. and Fukui, S. *Wear* **200**, 296-304 (1996)

Kim, Y.; McCarley, R. L. and Bard, A. J. *Langmuir* **9**, 8 (1993)

Konash, P. L. and Bastiaans, G. J. *Anal. Chem* **52,** 1929-1931 (1980)

Krim, J. and Widom, A. *Phys. Rev. B* **38,** 17 12184-12189 (1988)

Krim, J.; Watts, E. T. and Digel, J. *J. Vac. Sci. Technol. A* **8,** 4 (1990)

Krim, J. *Langmuir* **12,** 4564-4566 (1996a)

Krim, J. *Scientific American* 48-56 October (1996b)

Lamont, R. L. *Waveguides* (Methuen, London 1942)

Landman, U.; Barnett, R. N.; Cheng, H.-P.; Cleveland, C. L. and Luedtke, W. D. in *Computations for the Nano-Scale* 75-113 ed Bloohl, P. E.; Joachim, C. and Fisher, A. J. (Kluwer, Dordrecht, 1993)

Landman, U.; Luedtke, W. D.; Burnham, N. A. and Colton, R. J. *Science* **248**, 454-461 (1990)

Landman, U.; Luedtke, W. D. and Ringer, E. M. *Wear* **153,** 3-30 (1992a)

Landman, U.; Luedtke, W. D. and Ringer, E. M. in *Fundementals of Friction* ed Singer, I. L. and Pollock, H. M. (Kluwer, Dordrecht 1992) (1992b)

Laschitsch, A and Johannsmann, D. *J Appl Phys.* **85,** 7 3759-3765 (1999)

Lin, Z. and Ward, M. D. *Anal. Chem.* **67,** 4 685-693 (1995)

Lio, A; Charych, D. H. and Salmeron, M. *J. Phys. Chem. B* **10**(19), 3800. (1997)

Liu, G-y. and Salmeron, M. B. *Langmuir* **10,** 2, 367 (1994)

Ludema, K.C. and Tabor, D. *Wear* **9,** 329 (1966)

Martin , B. A. and Hagar, H. E. *J. Appl. Phys.* **65,** 7 2627-2629 (1989a)

Martin, B. A. and Hagar, H. E. *J. Appl. Phys.* **65,** 7 2630-2635 (1989b)

Mason, W. P. *Piezoelectric Crystals and their Applications to Ultrasonics* (Van Nostrand, Princeton, 1948)

Mate, C. M.; McClelland, G. M.; Erlandsson, R. and Chiang, S. *Phys. Rev. Lett.* **59,** 1942-1945 (1987)

Matveevsky, R. M. *A temperature method for estimating the limiting lubricating properties of machine oils* (in Russian) *Acad. Sci. U.S.S.R.* 1956

McClelland , G.M. and Glosli, J.N. in *Fundementals of Friction* ed Singer, I. L. and Pollock, H. M. (Kluwer, Dordrecht) (1992)

Meyer, G. and Amer, N. M. *Appl. Phys. Lett.* **57,** 2089-2091 (1990)

Meyer, E.; Overney, R.; Brodbeck, D.; Howald, L.; Lüthi, R.; Frommer, J. and Güntherodt, H.-J. *Phys. Rev. Let.* **69,** 12 (1992)

Mindlin, R. D. *J. Appl. Phys.* **22,** 316 (1951)

Newman, F. H. and Searle, V. H. L. *The General Properties of Matter* (Edward Arnold & Co, London 1950)

Numura, T. and Minemura, A. *Nippon Kagaku Kaishi* 1621 (1980)

Pascoe, M. W. Ph.D. Dissertation, Cambridge (1954)

Persson, B. N. J. *Sliding Friction: Physical principles and applications* (Springer, Berlin1998)

Rabinowicz, E. and Tabor, D. *Proc. R. Soc.* A **208,** 455 (1951)

Rayleigh, Lord *Proc. London Math. Soc.* **17,** 4-11 (1885)

Reddy, S. M.; Jones, J. P. and Lewis, T. J. *J. Appl. Phys.* **83,** 5 2524-2532 (1998)

Robbins, M. O. and Thompson, P. A. *Science* **253** 916 (1991)

Robinson, I.; Sambles, J. R. and Cade, N.A. *J. Colloid Interf. Sci* **133,** 2 321-332 (1989)

Ruan, J. and Bhushan, B. J. *J. Appl. Phys.* **76,** 5022-5035 (1994)

Ruan, J. and Bushan, B. J. *Mater. Res.* **8,** 3019-3022 (1993)

Quinn, T. J.F. *Physical Analysis for Tribology* (Cambridge University Press, 1991)

Salmeron, M *Chem Tech* 17-23 (1998)

Salmeron, M.; Lui, G.-y. and Ogletree, D. F. in *Forces in Scanning Probe Methods* (Kluwer Academic Publishers: Dordrecht, The Netherlands, 1995)

Sauerbrey, G. Z. *Phys.* **155,** 206-222 (1959)

Shutilov, V. A. *Fundamental Physics of Ultrasound* (Trans M. E. Alferieff) (Gordon and Breach Science Publishers, London 1988)

Smith, E. D.; Robbins, M. O. and Cieplak, M. *Phys. Rev. B* **54**(11) 8252-8260 (1996)

Tabor, D *Trib. Int.* **28,** 1 (1995)

Tabor, D. and Winterton, R. H. S. *Proc. R. Soc. London* Ser A **312,** 435 (1969)

Thompson, P. A. and Robbins, M. O. *Science* **250** 792-792 (1990)

Tomlinson, G. A. *Philos. Mag.* **7,** 905 (1929)

Tsukruk, V.V.; Bliznyuk, V.N.; Hazel, J.; Visser, D. and Everson, M.P. *Langmuir* **12,** 4840 (1996)

White , R. M. *Proc. IEEE* **58,** 1238-1276 (1970)

Xiao, X-d.; Hu, J.; Charych, D. H. and Salmeron, M. *Langmuir* **12**(2), 235. (1996)

Yoshizawa, H., Chen, Y. L. and Israelachvili, J. N. *J. Phys. Chem.* **97,** 4128 (1993a)

Yoshizawa, H.; Mcguiggan, P. and Israelachvili, J. N. *Science* **259,** 1305 (1993b)

AUTOMATIC LEVEL CONTROL

ACTIVE RECTIFIER

SET AMPLITUDE
(1V P-P)

IC2   EL4452C

YELLOW

XTAL

BLUE

100Ω

| I D B Ltd |
| --- |
| Dean St, Bangor, Gwynedd LL57 IUT |

CRYSTAL OSCILLATOR

| ID747301 SC1 | ID747/001/04 |
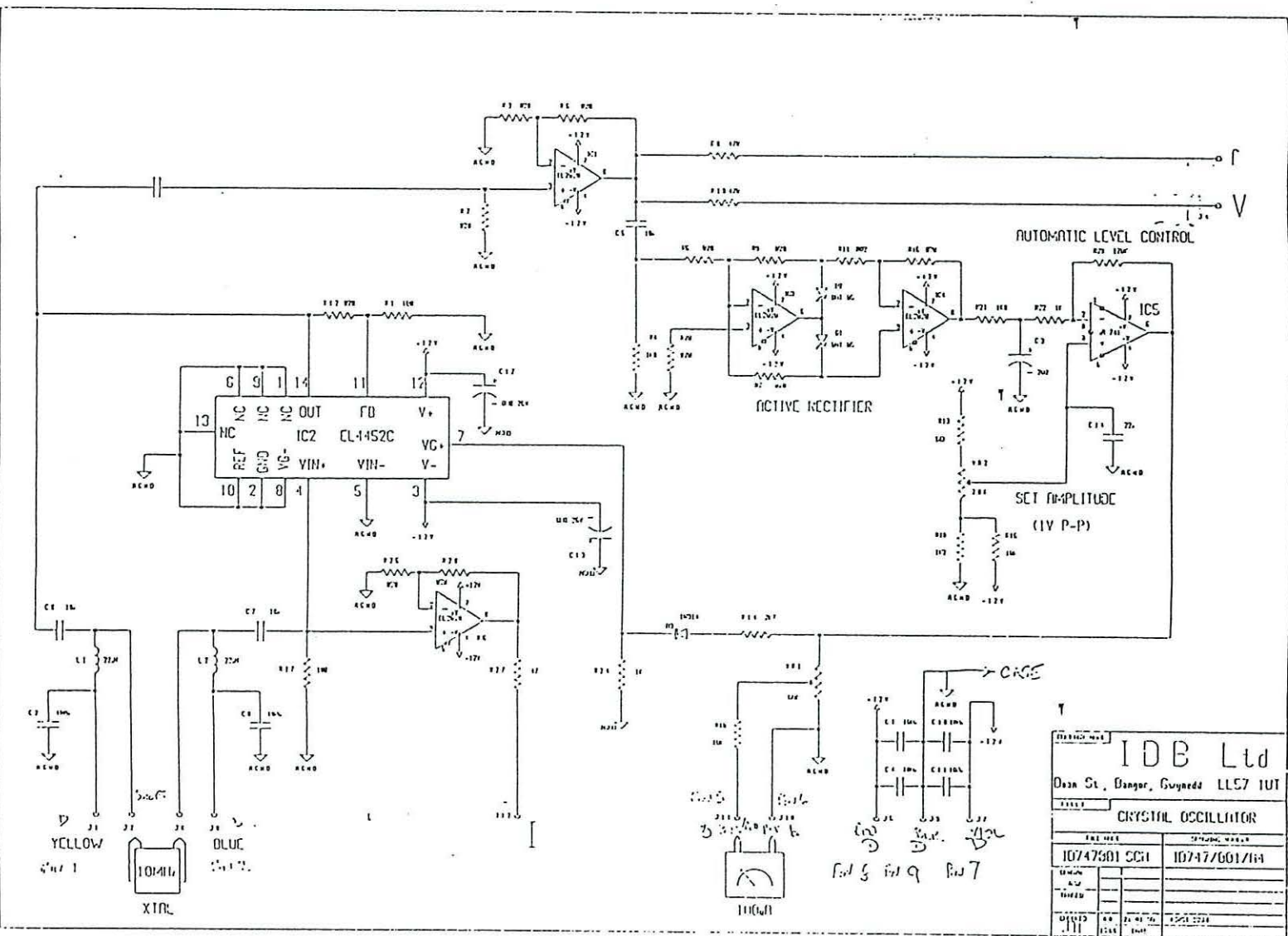
# Appendix B Listing of Visual Basic Program

```
AL2.VBP
=======

Form=MAIN.FRM
Form=FILES.FRM
Form=RT_PLOT.FRM
Module=Measure; MEASURE.BAS
Module=ADC_16; ADC16.BAS
Module=GLOBAL; GLOBAL.BAS
Module=HPIBERR; HPIBERR.TXT
Object={F9043C88-F6F2-101A-A3C9-08002B2F49FB}#1.0#0; COMDLG16.OCX
Object={BDC217C8-ED16-11CD-956C-0000C04E4C0A}#1.0#0; TABCTL16.OCX
Object={FAEEE763-117E-101B-8933-08002B2F4F5A}#1.0#0; DBLIST16.OCX
Object={00028C01-0000-0000-0000-000000000046}#1.0#0; DBGRID16.OCX
Reference=*\G{BEF6E001-A874-101A-8BBA-00AA00300CAB}
           #1.0#0#C:\WINDOWS\SYSTEM\OC25.DLL#Standard OLE Types
Reference=*\G{00025E01-0000-0000-C000-000000000046}
           #2.5#0#C:\WINDOWS\SYSTEM\DAO2516.DLL#Microsoft DAO 2.5 Object Library
ProjWinSize=69,434,252,209
ProjWinShow=2
IconForm="Main"
ExeName="AL2.EXE"
Name="AutoLab2"
HelpContextID="0"
StartMode=0
VersionCompatible="0"
MajorVer=1
MinorVer=0
RevisionVer=0
AutoIncrementVer=0
ServerSupportFiles=0
VersionCompanyName="Quartz Crystal Sensors Group"


MAIN.FRM
========

VERSION 4.00
Begin VB.Form Main
   Caption        =    "AutoLab 2.0"
   Icon           =    "MAIN.frx":0000
   LinkTopic      =    "Form1"
   Begin VB.TextBox TextComOld
      Enabled     =    0     'False
      Text        =    "Comment Log"
   End
   Begin VB.TextBox TextCom
   End
   Begin VB.Timer TimerIco
      Interval    =    750
   End
   Begin VB.TextBox TextRelF
      Text        =    "10e6"
   End
   Begin VB.Frame Experiment
      Caption        =    "Experiment"
      Begin VB.OptionButton OptionPM
         Caption     =    "Philips 6666"
         Value       =    -1   'True
      End
      Begin VB.OptionButton OptionRacal
         Caption     =    "Racal-Dana"
      End
      Begin VB.OptionButton OptionStanford
         Caption     =    "Stanford Synth"
      End
      Begin VB.OptionButton OptionFarnell
         Caption     =    "Farnell Synth"
      End
   End
   Begin VB.CommandButton CmdGraph
      Caption        =    "Graph"
   End
```

```
    Begin VB.TextBox TimeInterval
    End
    Begin VB.CommandButton CmdExit
       Caption         =    "Exit"
    End
    Begin VB.CommandButton CmdStop
       Caption         =    "Stop"
       Enabled         =    0    'False
    End
    Begin VB.CommandButton CmdStart
       Caption         =    "Start"
    End
    Begin VB.Image ImageIco
       Picture         =    "MAIN.frx":030A
       Visible         =    0    'False
    End
    Begin VB.Image ImageIco
       Picture         =    "MAIN.frx":0614
    End
    Begin VB.Image ImageIco
       Picture         =    "MAIN.frx":091E
    End
    Begin VB.Image ImageIco
       Picture         =    "MAIN.frx":0C28
    End
    Begin VB.Image ImageIco
       Picture         =    "MAIN.frx":0F32
    End
    Begin VB.Label Label7
       Caption         =    "Fs relative to:"
    End
    Begin VB.Image ImgDisc
       Picture         =    "MAIN.frx":123C
    End
    Begin VB.Label Label6
       Caption         =    "Seconds"
    End
    Begin VB.Label Label5
       Caption         =    "write every"
    End
    Begin VB.Label LabelFile
       Caption         =    "<File = none>"
    End
    Begin VB.Label Label4
       Caption         =    "Phase degrees"
    End
    Begin VB.Label Label3
       Caption         =    "R ohms"
    End
    Begin VB.Label Label2
       Caption         =    "Freq Hz"
    End
    Begin VB.Label Label1
       Caption         =    "time (s)"
    End
End

Attribute VB_Name = "Main"
Attribute VB_Creatable = False
Attribute VB_Exposed = False
Dim TInt As Integer
Dim DStart As Date
Dim Instrument As Integer

Private Sub CmdExit_Click()
    Call hpib_close
    End
End Sub
Private Sub CmdGraph_Click()
    If ImgDisc.Visible Then
        Call RTPlot.StartUp(LabelFile.Caption)
    Else
        Call MsgBox("Graph needs a file!", vbOKOnly)
    End If
End Sub
```

```
Private Sub CmdStart_Click()
    Dim LabTemp As Double
    Dim Frequency As Double
    Dim Zmin As Double
    Dim Phase As Double
    Dim Z As Double
    Dim P As Double
    Dim NoOfPoints As Integer
    Dim T As Double
    Dim TT As Double
    Dim day As Integer
    Dim FD As Date

    CmdStop.Enabled = True
    CmdStart.Enabled = False
    Frequency = MeasureSetUp(Instrument) - Val(TextRelF.Text)
    LabTemp = MeasureLabTemp
    Zmin = GetZmin
    Phase = GetPhase
    NoOfPoints = 1
    DStart = Now
    T = 0
    TextCom.Text = Now

    While CmdStop.Enabled = True
        DoEvents
        Frequency = Frequency / NoOfPoints
        LabTemp = LabTemp / NoOfPoints
        Zmin = Zmin / NoOfPoints
        Phase = Phase / NoOfPoints
        Label1.Caption = Str$(T) + " s"
        Label2.Caption = Left$(Str$(Frequency), 11) + " Hz"
        Label3.Caption = Left$(Str$(Zmin), 7) + " ohms"
        Label4.Caption = Left$(Str$(Phase), 6) + " degrees"
        If ImgDisc.Visible Then Call FileSel.WriteData(T, Frequency, Zmin,↵
                                                Phase, LabTemp)
        If RTPlot.Visible Then Call RTPlot.Plot(T, Frequency, Zmin, Phase)

        FD = DateAdd("s", TInt, Now)
        Frequency = 0
        LabTemp = 0
        Zmin = 0
        Phase = 0
        NoOfPoints = 0
        Do
            Frequency = Frequency + MeasureFreq() - Val(TextRelF.Text)
            LabTemp = LabTemp + MeasureLabTemp
            Zmin = Zmin + GetZmin
            Phase = Phase + GetPhase
            NoOfPoints = NoOfPoints + 1
            DoEvents
        Loop While FD > Now And CmdStop.Enabled
        T = DateDiff("s", DStart, Now)
    Wend
    CmdStart.Enabled = True
    Call hpib_close
    Call adc16_close
End Sub

Private Sub CmdStop_Click()
    CmdStop.Enabled = False
End Sub

Private Sub Form_Load()
    TInt = 5
    Instrument = 3
End Sub
```

```vb
Private Sub LabelFile_Click()
    Dim filename As String

    If ImgDisc.Visible Then
        If MsgBox("Stop Recording to file?", vbYesNo + vbExclamation) = vbYes Then
            ImgDisc.Visible = False
            LabelFile.Caption = "<file = none>"
            Exit Sub
        End If
    End If
    filename = FileSel.GetFile()
    If filename <> "" Then
        LabelFile.Caption = filename
        ImgDisc.Visible = True
        DStart = Now
    Else
        LabelFile.Caption = "<file = none>"
    End If
End Sub

Private Sub OptionFarnell_Click()
    Instrument = 0
End Sub

Private Sub OptionPM_Click()
    Instrument = 3
End Sub

Private Sub OptionRacal_Click()
    Instrument = 2
End Sub

Private Sub OptionStanford_Click()
    Instrument = 1
End Sub

Private Sub TextCom_KeyPress(KeyAscii As Integer)
    If KeyAscii = 13 Then
        TextComOld.Text = TextCom.Text
        If ImgDisc.Visible Then
            Call FileSel.WriteLog(DateDiff("s", DStart, Now), TextCom.Text)
        End If
    TextCom.Text = ""
    End If
End Sub

Private Sub TimeInterval_KeyPress(KeyAscii As Integer)
    If KeyAscii = 13 Then TInt = Val(TimeInterval.Text)
End Sub

Private Sub TimerIco_Timer()
        Static IcoIndex As Integer
        IcoIndex = IcoIndex + 1
        If IcoIndex > 4 Then IcoIndex = 0
        Main.Icon = ImageIco(IcoIndex).Picture
End Sub
```

```
FILES.FRM
=========

VERSION 4.00
Begin VB.Form Files
   Caption         =    "Select Output File"
   Icon            =    "FILES.frx":0000
   LinkTopic       =    "Form1"
   Begin VB.CommandButton Cancel
      Caption          =    "Cancel"
   End
   Begin VB.CommandButton CmdOK
      Caption          =    "OK"
   End
   Begin VB.TextBox TextFile
   End
   Begin VB.FileListBox File1
      Pattern          =    "*.frq;*.zmn;*.phs;*.alg"
   End
   Begin VB.DirListBox Dir1
   End
   Begin VB.DriveListBox Drive1
   End
End
Attribute VB_Name = "FileSel"
Attribute VB_Creatable = False
Attribute VB_Exposed = False
Dim running As Integer

Function GetFile() As String
    Show 0       'Display this form (modeless so this function can continue)
    running = 1 'set flag (Global variable)
    While running = 1
        DoEvents
    Wend            'Wait for OK or cancel
    Hide            'Hide this form
    GetFile = TextFile.Text
End Function

Sub WriteData(ByVal T As Double, ByVal F As Long, ByVal Z As Double,↵
                            ByVal P As Double, ByVal LT As Double)
     Dim filename As String
     filename = TextFile.Text
     Open filename + ".frq" For Append As #1
     Print #1, T, F
     Close #1
     Open filename + ".zmn" For Append As #1
     Print #1, T, Z
     Close #1
     Open filename + ".phs" For Append As #1
     Print #1, T, P
     Close #1
     Open filename + ".lt" For Append As #1
     Print #1, T, LT
     Close #1
End Sub

Sub WriteLog(T As Double, Comment As String)
    Dim filename As String
    filename = TextFile.Text
    Open filename + ".log" For Append As #2
    Print #2, T, Comment
    Close #2
End Sub

Private Sub Cancel_Click()
      TextFile.Text = ""
      running = 0
End Sub
```

```vb
Private Sub CmdOK_Click()
    response = 0
    'Check for attempt to return directory
    If Right$(TextFile.Text, 1) = "\" Then
      response = MsgBox("Choose a File Name", vbOKOnly, "Output File")
      Exit Sub
    End If

    On Error GoTo error_FNF
    'Try to make File1 same as text box (User might have typed)
    File1.filename = TextFile.Text
    'If there were no errors file exists so querry overwrite
    response = MsgBox("File Already Exists. Overwrite?",↵
                                    vbYesNo + vbQuestion, "Output File")
    If response = vbNo Then
        File1.Pattern = "*.frq;*.zmn;*.phs;*.alg"
        Exit Sub
    Else
         While InStr(TextFile.Text, ".")
            TextFile.Text = Left$(TextFile.Text, Len(TextFile.Text) - 1)
         Wend
         Kill TextFile.Text + ".*"
    End If

error_FNF:
    File1.Pattern = "*.frq;*.zmn;*.phs;*.alg"
    If Err = 53 Or response = vbYes Then
        While InStr(TextFile.Text, ".")
            TextFile.Text = Left$(TextFile.Text, Len(TextFile.Text) - 1)
        Wend

        running = 0
        Exit Sub
    End If
    response = MsgBox(error$, vbOKOnly + vbExclamation, "Output File")
End Sub

Private Sub Dir1_Change()
    File1.Path = Dir1.Path
    If Right$(Dir1.Path, 1) = "\" Then
        TextFile.Text = Dir1.Path
    Else
        TextFile.Text = Dir1.Path + "\"
    End If
End Sub

Private Sub Drive1_Change()
    Dir1.Path = Drive1.Drive
    If Right$(Dir1.Path, 1) = "\" Then
        TextFile.Text = Dir1.Path
    Else
        TextFile.Text = Dir1.Path + "\"
    End If
End Sub

Private Sub File1_Click()
        If Right$(File1.Path, 1) = "\" Then
          TextFile.Text = File1.Path + File1.filename
        Else
          TextFile.Text = File1.Path + "\" + File1.filename
        End If
End Sub

Private Sub Form_Load()
    Drive1_Change
    If Right$(Dir1.Path, 1) = "\" Then
        TextFile.Text = Dir1.Path
    Else
        TextFile.Text = Dir1.Path + "\"
    End If
End Sub

Private Sub TextFile_KeyPress(KeyAscii As Integer)
    If KeyAscii = 13 Then CmdOK_Click
End Sub
```

```
RT_PLOT.FRM
===========

VERSION 4.00
Begin VB.Form RT_Plot
   Caption         =   "AutoLab Real Time Plotting"
   Icon            =   "RT_Plot.frx":0000
   LinkTopic       =   "Form1"
   Begin VB.Frame MouseOut
      Caption      =   "Cursor"
      Begin VB.TextBox MouseX
      End
      Begin VB.TextBox MouseY
      End
      Begin VB.Label Label2
         Caption   =   "Y"
      End
      Begin VB.Label Label1
         Caption   =   "Time"
      End
   End
   Begin VB.TextBox YBot
      Alignment    =   1 'Right Justify
      Text         =   "-90"
   End
   Begin VB.TextBox YTop
      Text         =   "90"
   End
   Begin VB.TextBox YBot
      Text         =   "0"
   End
   Begin VB.TextBox YTop
      Text         =   "500"
   End
   Begin VB.PictureBox graph
      AutoRedraw   =   -1  'True
      MousePointer =   2  'Cross
   End
   Begin VB.PictureBox graph
      AutoRedraw   =   -1  'True
      MousePointer =   2  'Cross
   End
   Begin VB.CommandButton Close
      Caption      =   "Close"
   End
   Begin VB.TextBox YBot
      Text         =   "-1000"
   End
   Begin VB.TextBox YTop
      Text         =   "1000"
   End
   Begin VB.TextBox TimeAxis
      Text         =   "1000"
   End
   Begin VB.TextBox TimeAxis
      Text         =   "0"
   End
   Begin VB.PictureBox graph
      AutoRedraw   =   -1  'True
      MousePointer =   2  'Cross
   End
   Begin VB.Label Title
      Caption      =   "Phase /degrees"
   End
   Begin VB.Label Title
      Caption      =   "Impedance /ohms"
   End
   Begin VB.Label Title
      Caption      =   "Frequency /Hz"
   End
   Begin VB.Image Select
      Picture      =   "RTP.frx":030A
   End
```

```
   Begin VB.Image Select
      Picture          =    "RTP.frx":0614
   End
   Begin VB.Image Select
      Picture          =    "RTP.frx":091E
   End
End

Attribute VB_Name = "RTPlot"
Attribute VB_Creatable = False
Attribute VB_Exposed = False
Dim Graph_File As String
Dim last_box As Object
Dim t1 As Single
Dim t2 As Single
Dim y1(3) As Single
Dim y2(3) As Single
Dim axis As Integer

Sub Plot(ByVal T As Double, ByVal F As Long, ByVal Z As Double, ByVal P As Double)
      On Error Resume Next

      TAxis = Val(TimeAxis(1).Text)
      If T < TAxis And TAxis <> 0 Then
          y2(0) = F: y2(1) = Z: y2(2) = P
          For para% = 0 To 2
              graph(para%).Line (t1, y1(para%))-(T, y2(para%))
              y1(para%) = y2(para%)
          Next para%
          t1 = T
      Else
          TimeAxis(1).Text = TimeAxis(1).Text + 1000
          Call Rescale
      End If
End Sub

Sub Rescale(Optional idx)
      On Error GoTo err_rs

      If IsMissing(idx) Then
          For Index% = 0 To 2
              Call Rescale(Index%)
          Next Index%
          Exit Sub
      End If

      Select Case idx
      Case 0
          Open Graph_File + ".frq" For Input As #2
      Case 1
          Open Graph_File + ".zmn" For Input As #2
      Case 2
          Open Graph_File + ".phs" For Input As #2
      Case Else
          Exit Sub 'idx out of range
      End Select

      graph(idx).Scale (TimeAxis(0).Text, YTop(idx).Text)-(TimeAxis(1).Text,↵
                                                      Ybot(idx).Text)
      graph(idx).Cls
      Input #2, t1, y1(idx)
      Do
          Input #2, t2, y2(idx)
          graph(idx).Line (t1, y1(idx))-(t2, y2(idx))
          t1 = t2
          y1(idx) = y2(idx)
      Loop While Not EOF(2)
      Close #2
      Exit Sub
```

```
err_rs:
        If Err = 62 Then 'Check for empty file
            t1 = AutoLab.TextOut(3)
            y1(idx) = AutoLab.TextOut(idx)
        End If
        Close #2
        Exit Sub

End Sub

Sub StartUp(filename As String)
        Graph_File = filename
            Show
            Call Rescale
            YTop(0).ZOrder
            Ybot(0).ZOrder
            graph(0).ZOrder
            Title(0).ZOrder
End Sub

Private Sub Close_Click()
    Hide
End Sub

Private Sub Form_Load()
        Set last_box = TimeAxis(0)
        axis = 0
End Sub

Private Sub graph_MouseDown(Index As Integer, Button As Integer, Shift As Integer,↵
                                        X As Single, Y As Single)
        If Button = vbRightButton Or Shift = vbShiftMask Then
                If axis = 0 Then
                last_box.Text = X
                        Call Rescale
                Else
                last_box.Text = Y
                        Call Rescale(Index)
                End If
        End If
End Sub

Private Sub graph_MouseMove(Index As Integer, Button As Integer, Shift As Integer,↵
                                        X As Single, Y As Single)
        MouseX.Text = X
        MouseY.Text = Y
End Sub

Private Sub Select_Click(Index As Integer)
        YTop(Index).ZOrder
        Ybot(Index).ZOrder
        graph(Index).ZOrder
        Title(Index).ZOrder
End Sub

Private Sub TimeAxis_GotFocus(Index As Integer)
        Set last_box = TimeAxis(Index)
        axis = 0
End Sub

Private Sub TimeAxis_KeyPress(Index As Integer, KeyAscii As Integer)
        If KeyAscii = 13 Then
            Call Rescale
        End If
End Sub

Private Sub Ybot_GotFocus(Index As Integer)
        Set last_box = Ybot(Index)
        axis = 1
End Sub

Private Sub Ybot_KeyPress(Index As Integer, KeyAscii As Integer)
        If KeyAscii = 13 Then Call Rescale(Index)
End Sub
```

A10

```
Private Sub YTop_GotFocus(Index As Integer)
        Set last_box = YTop(Index)
        axis = 1
End Sub

Private Sub YTop_KeyPress(Index As Integer, KeyAscii As Integer)
    If KeyAscii = 13 Then Call Rescale(Index)
End Sub
```

A11

```
MEASURE.BAS
===========

Attribute VB_Name = "Measure"
Declare Function getvolts Lib "sample.DLL" (ByVal channel As Integer) As Long

Const pi As Double = 3.14159265359

Dim device As Long
Dim hHpib As Integer
Dim open_hpib As Integer
Dim error_hpib As Integer
Dim Frequency As Double
Dim Instrument As Integer
Dim PhaseCorection As Double
Dim R As Double
Dim Zmin As Double
Dim Phase As Double

Function GetPhase() As Double
        GetPhase = Phase
End Function

Function GetZmin() As Double
        GetZmin = Zmin
End Function

Function MeasureFreq() As Double
        Select Case Instrument
        Case 0
            MeasureFreq = FarnellFreq()
        Case 1
            MeasureFreq = StanfordFreq()
        Case 2
            MeasureFreq = RacalDanaFreq()
        Case 3
            MeasureFreq = PhilipsFreq()
        Case Else
            MeasureFreq = 0
        End Select
        MeasureZmin
End Function

Function MeasureLabTemp() As Double
    MeasureLabTemp = adc16_read(8) * (2500 / 65535)
End Function

Function MeasureSetUp(Instmt As Integer) As Double
        Instrument = Instmt
        Select Case Instmt
        Case 0
            MeasureSetUp = FarnellSetUp()
        Case 1
            MeasureSetUp = StanfordSetUp()
        Case 2
            MeasureSetUp = RacalDanaSetUp()
        Case 3
            MeasureSetUp = PhilipsSetUp()
        Case Else
            MeasureSetUp = 0
            '1 for stanford 2 for RD 3 for HP
        End Select
        MeasureZmin
End Function
```

A12

```
Sub MeasureZmin()
        On Error Resume Next
        Dim A As Double
        Dim B As Double
        Dim C As Double
        Dim Rad As Double
        Dim Real As Double
        Dim Imag As Double

        If Instrument < 2 Then
            A = getvolts(0) / 100000000
            B = getvolts(1) / 100000000
            C = 361# * getvolts(2) / 100000000
            C = C - PhaseCorection - 0.378
        Else
            A = adc16_read(1)
            B = adc16_read(2)
            C = 0.01388571 * adc16_read(3) - PhaseCorection
            'A = A * 3.047296 'Allow for 10 dB Attn in V
        End If
        Rad = C * pi / 180
        Real = R * A * Cos(Rad) / B - R
        Imag = -R * A * Sin(Rad) / B
        Zmin = Sqr(Real ^ 2 + Imag ^ 2)
        Phase = Atn(Imag / Real) * 180 / pi
End Sub

Function out_f(F As Long) As Double
        Dim volts As Double
        Dim pause

        fval$ = Str$(F)
        If Instrument = 0 Then  'Farnell
        no_space$ = Right$(fval$, Len(fval$) - 1)
        f_out$ = "F" + String$(9 - Len(no_space$), "0") + no_space$
        Else                    'Stanford
        f_out$ = "FREQ" + fval$
        End If
        Call hpib_write(f_out$)
        pause = Timer
        While Timer < (pause + 0.07)
        Wend  'wait 70 mS
        volts = getvolts(3) / 100000000#
        out_f = volts
End Function

Function FarnellSetUp() As Double
    Dim F As Long
    Dim df As Long
    Dim v_low As Double
    Dim v_mid As Double
    Dim v_high As Double

    PhaseCorection = 0
    R = 103.4
    F = 1000000
    df = 32768
    'phase _cor = 0:R=103.4

    Call hpib_open("hpib6,10", 2000)
    v_mid = out_f(F)
    While (df >= 1)
       v_low = out_f(F - df)
       v_high = out_f(F + df)
       If v_low > v_mid Then F = F - df: v_mid = v_low
       If v_high > v_mid Then F = F + df: v_mid = v_high
       df = df / 2
    Wend
    Frequency = F * 10
    FarnellSetUp = F * 10
End Function
```

```
Function FarnellFreq() As Double
    Dim F As Long
    Dim df As Long
    Dim v_low As Double
    Dim v_mid As Double
    Dim v_high As Double

    F = CLng(Frequency / 10)
    df = 128
    v_mid = out_f(F)
    While (df >= 1)
        v_low = out_f(F - df)
        v_high = out_f(F + df)
        If v_low > v_mid Then F = F - df: v_mid = v_low
        If v_high > v_mid Then F = F + df: v_mid = v_high
        df = df / 2
    Wend
    Frequency = F * 10
    FarnellFreq = F * 10
End Function

Sub hpib_close()
        If open_hpib Then
            error_hpib = HpibClose(hHpib)
            Debug.Print HpibErrStr$(error_hpib)
            open_hpib = False
        End If
End Sub

Function hpib_open(addr As String, Time As Integer)
        Dim TimeVal As Single
        Dim inst As Integer
        Dim error As Integer

        box$ = Right$(addr, 2)
        inst = Val(box$)
        Debug.Print "Inst"; inst
        device = 600 + inst

        TimeVal = Time / 1000#
        error_hpib = HpibOpen(6, hHpib)
        Debug.Print HpibErrStr$(error_hpib)
        error_hpib = HpibReset(hHpib, 6)
        Debug.Print HpibErrStr$(error_hpib)
        error_hpib = HpibTimeout(hHpib, 6, TimeVal)
        Debug.Print HpibErrStr$(error_hpib)
        open_hpib = True
        hpib_open = True
End Function

Function hpib_read() As String
        Dim Z As String
        Z = Space$(21)
        error_hpib = HpibEnters(hHpib, device, Z, 21)
        Debug.Print HpibErrStr$(error_hpib)
        Debug.Print "Read"; Z
        crlfpos = InStr(Z, Chr$(13))
        If crlfpos Then
          Z = Left(Z, crlfpos - 1)
        End If
        crlfpos = InStr(Z, Chr$(10))
        If crlfpos Then
          Z = Left(Z, crlfpos - 1)
        End If
        hpib_read = Z
End Function

Sub hpib_write(com As String)
        Dim length As Integer
        length = Len(com)
        error_hpib = HpibOutputs(hHpib, device, com, length)
        Debug.Print HpibErrStr$(error_hpib)
End Sub
```

```
Function PhilipsFreq() As Double
    F$ = hpib_read()
    PhilipsFreq = Val(Right(F$, Len(F$) - 4))
End Function

Function PhilipsSetUp() As Double
    PhaseCorection = 31
    R = 69.7
    Call adc16_open
    Call hpib_open("hpib6,10", 5000)
    Call hpib_write("AUTO ON")
    Call hpib_write("FREQ A")
    Call hpib_write("MTIME 1")
    F$ = hpib_read()

    For chan% = 1 To 3
        Call adc16_setup(chan%, 16)
        garbage = adc16_read(chan%)
        garbage = adc16_read(chan%)
        garbage = adc16_read(chan%)
    Next chan%
    chan% = 8
        Call adc16_setup(chan%, 16)
        garbage = adc16_read(chan%)
        garbage = adc16_read(chan%)
        garbage = adc16_read(chan%)
    PhilipsSetUp = Right(F$, Len(F$) - 4)
End Function

Function RacalDanaFreq() As Double
    Call hpib_write("RF")
    Frequency = Val(hpib_read())
    RacalDanaFreq = Frequency
End Function

Function RacalDanaSetUp() As Double
    PhaseCorection = 31
    R = 69.7
    Call adc16_open
    Call hpib_open("hpib6,15", 2000)
    Call hpib_write("S81")
    Call hpib_write("S20")
    Call hpib_write("FA")
    Call hpib_write("T0")
    Call hpib_write("SRS7")
    Call hpib_write("RF")
    Frequency = Val(hpib_read())

    For chan% = 1 To 3
        Call adc16_setup(chan%, 16)
        garbage = adc16_read(chan%)
        garbage = adc16_read(chan%)
        garbage = adc16_read(chan%)
    Next chan%
    chan% = 8
        Call adc16_setup(chan%, 16)
        garbage = adc16_read(chan%)
        garbage = adc16_read(chan%)
        garbage = adc16_read(chan%)

    RacalDanaSetUp = Frequency
End Function
```

```
Function StanfordFreq() As Double
        Dim F As Long
        Dim df As Long
        Dim v_low As Double
        Dim v_mid As Double
        Dim v_high As Double

        F = CLng(Frequency)
        df = 128
        v_mid = out_f(F)
        While (df >= 1)
         v_low = out_f(F - df)
         v_high = out_f(F + df)
         If v_low > v_mid Then F = F - df: v_mid = v_low
         If v_high > v_mid Then F = F + df: v_mid = v_high
         df = df / 2
        Wend
        Frequency = F
        StanfordFreq = F
End Function

Function StanfordSetUp() As Double
        Dim F As Long
        Dim df As Long
        Dim v_low As Double
        Dim v_mid As Double
        Dim v_high As Double

        PhaseCorection = 0
        R = 103.4
        F = 10000000
        df = 262144
        'phase _cor = 0:R=103.4

        Call hpib_open("hpib6,19", 2000)
        v_mid = out_f(F)
        While (df >= 1)
         v_low = out_f(F - df)
         v_high = out_f(F + df)
         If v_low > v_mid Then F = F - df: v_mid = v_low
         If v_high > v_mid Then F = F + df: v_mid = v_high
         df = df / 2
        Wend
        Frequency = F
        StanfordSetUp = F
End Function
```

A16

```vb
Attribute VB_Name = "ADC_16"
Declare Function adc16_open_unit Lib "ADC16.DLL" (ByVal Port As Integer) As Boolean
Declare Sub adc16_close_unit Lib "ADC16.DLL" (ByVal Port As Integer)
Declare Sub adc16_set_channel Lib "ADC16.DLL" (ByVal Port As Integer, ByVal channel As
Integer, ByVal Resolution As Integer, ByVal SingleEnded As Integer,↵
                                        ByVal Factor As Integer)
Declare Sub adc16_poll Lib "ADC16.DLL" ()
Declare Function adc16_get_value Lib "ADC16.DLL" (value As Long,↵
                    ByVal Port As Integer, ByVal channel As Integer) As Boolean
Declare Function adc16_get_filtered_value Lib "ADC16.DLL" (value As Long,↵
                    ByVal Port As Integer, ByVal channel As Integer) As Boolean
Declare Function adc16_get_cycle Lib "ADC16.DLL" (cycle As Long,↵
                                        ByVal Port As Integer) As Boolean
Dim Port As Integer
Dim opened As Integer
Dim cycle As Long
Dim last_cycle As Long
Dim value As Long

Sub adc16_close()
        Call adc16_close_unit(Port)
        opened = False
End Sub

Function adc16_cycle()
    If adc16_get_cycle(cycle, Port) Then
        adc16_cycle = Str(cycle)
    Else
        adc16_cycle = "errrrr"
    End If
End Function

Function adc16_open()
    On Error GoTo adc_err_o

    Port = 1
    If adc16_open_unit(Port) Then
        opened = True
        adc16_open = True
    Else
        opened = False
    End If
    adc16_open = opened
    Exit Function

adc_err_o:
    Debug.Print "error no"; Err
    Debug.Print error$
    Call adc16_close
    Exit Function

End Function

Function adc16_read(chan%)
        Static ok%
        On Error GoTo adc_err_r

      ok% = adc16_get_value(value, Port, chan%)
      If ok% Then
                adc16_read = value
      Else
        adc16_read = 0
      End If
      Exit Function

adc_err_r:
        Call adc16_close
        Exit Function

End Function
Sub adc16_setup(chan%, res%)
```

A17

```
        On Error GoTo adc_err_se

          Call adc16_set_channel(Port, chan%, res%, 1, 1)
          ok% = adc16_get_value(value, Port, chan%)
            Exit Sub

adc_err_se:
      Call adc16_close
      Exit Sub

End Sub

Sub adc16_sync()
        Static ok3%
        On Error GoTo adc_err_sy

        ok3% = adc16_get_cycle(last_cycle, Port)
        cycle = last_cycle
        While (cycle <= last_cycle + 1)
         DoEvents
         ok3% = adc16_get_cycle(cycle, Port)
         Call adc16_poll
        Wend
        Exit Sub

adc_err_sy:
        Call adc16_close
        Exit Sub

End Sub
```

A18

```
GLOBAL.BAS
==========


Attribute VB_Name = "GLOBAL"
Global waveform%(4000)
Global preamble!(10)


'HPIB.DLL Access
'Put into your GLOBAL.BAS file


Declare Function HpibAbort Lib "HPIB.DLL" (ByVal hWnd%, ByVal LVar&) As Integer
Declare Function HpibClear Lib "HPIB.DLL" (ByVal hWnd%, ByVal LVar&) As Integer
Declare Function HpibClose Lib "HPIB.DLL" (ByVal hWnd%) As Integer
Declare Function HpibControl Lib "HPIB.DLL" (ByVal hWnd%, ByVal LVar&,↵
                                ByVal IVar%, ByVal IVar%) As Integer
Declare Function HpibEnter Lib "HPIB.DLL" (ByVal hWnd%, ByVal LVar&,↵
                                        fVar As Single) As Integer
Declare Function HpibEntera Lib "HPIB.DLL" (ByVal hWnd%, ByVal LVar&,↵
                            fVar As Single, IVar As Integer) As Integer
Declare Function HpibEnterab Lib "HPIB.DLL" (ByVal hWnd%, ByVal LVar&,↵
                        fVar As Any, IVar As Integer, ByVal IVar%) As Integer
Declare Function HpibEnterb Lib "HPIB.DLL" (ByVal hWnd%, ByVal LVar&, fVar As Any,↵
                            IVar As Integer, ByVal IVar%) As Integer
Declare Function HpibEnterf Lib "HPIB.DLL" (ByVal hWnd%, ByVal LVar&,↵
                    ByVal aString As String, IVar As Long, ByVal IVar%) As Integer
Declare Function HpibEnters Lib "HPIB.DLL" (ByVal hWnd%, ByVal LVar&,↵
                        ByVal aString As String, IVar As Integer) As Integer
Declare Function HpibEoi Lib "HPIB.DLL" (ByVal hWnd%, ByVal LVar&, ByVal IVar%)↵
                                            As Integer
Declare Function HpibEol Lib "HPIB.DLL" (ByVal hWnd%, ByVal LVar&,↵
                        ByVal eolstring As String, ByVal IVar%) As Integer
Declare Function HpibFastout Lib "HPIB.DLL" (ByVal hWnd%, ByVal LVar&, ByVal IVar%)↵
                                            As Integer
Declare Function HpibGetterm Lib "HPIB.DLL" (ByVal hWnd%, ByVal LVar&,↵
                                IVar As Integer) As Integer
Declare Function HpibGetversion Lib "HPIB.DLL" () As Integer
Declare Function HpibLlockout Lib "HPIB.DLL" (ByVal hWnd%, ByVal LVar&) As Integer
Declare Function HpibLocal Lib "HPIB.DLL" (ByVal hWnd%, ByVal LVar&) As Integer
Declare Function HpibMatch Lib "HPIB.DLL" (ByVal hWnd%, ByVal LVar&,↵
                            ByVal char As Integer, ByVal IVar%) As Integer
Declare Function HpibOpen Lib "HPIB.DLL" (ByVal LVar&, hHandle As Integer) As Integer
Declare Function HpibOutput Lib "HPIB.DLL" (ByVal hWnd%, ByVal LVar&, ByVal DVar#)↵
                                            As Integer
Declare Function HpibOutputa Lib "HPIB.DLL" (ByVal hWnd%, ByVal LVar&,↵
                                fVar As Single, ByVal IVar%) As Integer
Declare Function HpibOutputab Lib "HPIB.DLL" (ByVal hWnd%, ByVal LVar&, fVar As Any,↵
                            ByVal IVar%, ByVal IVar%) As Integer
Declare Function HpibOutputb Lib "HPIB.DLL" (ByVal hWnd%, ByVal LVar&, fVar As Any,↵
                            ByVal IVar%, ByVal IVar%) As Integer
Declare Function HpibOutputf Lib "HPIB.DLL" (ByVal hWnd%, ByVal LVar&,↵
                    ByVal strdata As String, ByVal LVar As Long) As Integer
Declare Function HpibOutputs Lib "HPIB.DLL" (ByVal hWnd%, ByVal LVar&,↵
                            ByVal strdata As String, ByVal IVar%) As Integer
Declare Function HpibPpoll Lib "HPIB.DLL" (ByVal hWnd%, ByVal LVar&,↵
                                    IVar As Integer) As Integer
Declare Function HpibPpollc Lib "HPIB.DLL" (ByVal hWnd%, ByVal LVar&, ByVal IVar%)↵
                                            As Integer
Declare Function HpibPpollu Lib "HPIB.DLL" (ByVal hWnd%, ByVal LVar&) As Integer
Declare Function HpibRemote Lib "HPIB.DLL" (ByVal hWnd%, ByVal LVar&) As Integer
Declare Function HpibReset Lib "HPIB.DLL" (ByVal hWnd%, ByVal LVar&) As Integer
Declare Function HpibSend Lib "HPIB.DLL" (ByVal hWnd%, ByVal LVar&,↵
                        ByVal commands As String, ByVal IVar%) As Integer
Declare Function HpibSpoll Lib "HPIB.DLL" (ByVal hWnd%, ByVal LVar&, IVar As Integer)↵
                                            As Integer
Declare Function HpibStatus Lib "HPIB.DLL" (ByVal hWnd%, ByVal LVar&, ByVal IVar%,↵
                                IVar As Integer) As Integer
Declare Function HpibTimeout Lib "HPIB.DLL" (ByVal hWnd%, ByVal LVar&, ByVal DVar#)↵
                                            As Integer
Declare Function HpibTrigger Lib "HPIB.DLL" (ByVal hWnd%, ByVal LVar&) As Integer
```

```
Declare Function HpibPassctl Lib "HPIB.DLL" (ByVal hWnd%, ByVal LVar&) As Integer
Declare Function HpibTakectl Lib "HPIB.DLL" (ByVal hWnd%, ByVal LVar&, ByVal IVar%)↵
                                                          As Integer
Declare Function HpibRequest Lib "HPIB.DLL" (ByVal hWnd%, ByVal LVar&, ByVal IVar%)↵
                                                          As Integer

Global Const NOERR = 0
Global Const EUNKNOWN = 1
Global Const ESEL = 2
Global Const ERANGE = 3
Global Const ETIME = 4
Global Const ECTRL = 5
Global Const EPASS = 6
Global Const ENUMB = 7
Global Const EADDR = 8
Global Const EFILE = 9
Global Const EOPEN = 10
Global Const ENOOPEN = 11
Global Const ECLOSE = 12
Global Const EHANDLE = 13
Global Const STATREM = 0
Global Const STATSRQ = 1
Global Const STATNDAC = 2
Global Const STATSC = 3
Global Const STATAC = 4
Global Const STATTALK = 5
Global Const STATLIST = 6
Global Const STATADDR = 7
Global Const STATATN = 8
Global Const STATADR = 9
Global Const STATDIO = 10
Global Const STATBUS = 11
Global Const STATCARD = 12
```

```
HPIBERR.TXT
===========

Attribute VB_Name = "HPIBERR"

Function HpibErrStr$(errorcode As Integer)
        Select Case errorcode
            Case NOERR
                Msg$ = " No error "
            Case EUNKNOWN
                Msg$ = " Unknown error "
            Case ESEL
                Msg$ = " Invalid select code or device address "
            Case ERANGE
                Msg$ = " Value out of range "
            Case ETIME
                Msg$ = " Timeout "
            Case ECTRL
                Msg$ = " HP-IB must be controller "
            Case EPASS
                Msg$ = " Pass control not permitted "
            Case EFILE
                Msg$ = " File I/O Error "
            Case ENUMB
                Msg$ = " Invalid Number "
            Case EADDR
                Msg$ = " Improper addressing "
            Case EOPEN
                Msg$ = " Cannot Open This Card "
            Case ENOOPEN
                Msg$ = " Card is not open "
            Case ECLOSE
                Msg$ = " Cannot close card "
            Case EHANDLE
                Msg$ = " Invalid handle for this ISC "
            Case Else
                Msg$ = " What? "
        End Select
        HpibErrStr$ = Msg$
End Function
```

# Appendix C - Modelling a Matching Crystal

Calculates the expected resonance frequency and impedance when a quartz layer of variable thickness is in good acoustic contact with the surface of an active AT-cut crystal of 10 MHz resonance frequency.

## Resonator Parameters

This section defines the characteristics of the thickness shear mode resonator.

| | |
|---|---|
| Thickness | $lq := 1.66 \cdot 10^{-4} \cdot m$ |
| Effective Electrode Area | $A := 2.8 \cdot 10^{-5} \cdot m^2$ |
| Permittivity of Quartz | $\varepsilon := 40.71 \cdot 10^{-12} \cdot farad \cdot m^{-1}$ |
| Crystal Capacitance Co | $Co := \dfrac{A \cdot \varepsilon}{lq}$ |
| Density of Quartz | $\rho q := 2650 \cdot kg \cdot m^{-3}$ |
| Shear Wave Velocity in Quartz | $vq := 3320 \cdot m \cdot s^{-1}$ |
| Characteristic Impedance | $Zq := \rho q \cdot vq$ |
| Piezoelectric Coefficient | $e := 9.65 \cdot 10^{-2} \cdot coul \cdot m^{-2}$ |
| Fundamental Resonance fo | $fo := \dfrac{vq}{2 \cdot lq}$  $\qquad \omega o := 2 \cdot \pi \cdot fo$ |

## Layer Parameters

This section defines the characteristics of the second layer and generates an array of thickness values at which the model will be evaluated.

| | |
|---|---|
| Density | $\rho 2 := \rho q$ |
| Shear Wave Velocity | $v2 := vq$ |
| Attenuation | $\alpha := 0$ |
| Thickness (array) | $l := 1, 2 .. 200$ |
| | $l2_l := [0.998 + (0.00002 \cdot l)] \cdot 1.665 \cdot 10^{-4} \cdot m$ |
| Set first element to zero (unloaded sensor) | $l2_1 := 0$ |

## Frequency Range

Here an array of frequency values is generated. These are the frequencies at which the system will be modelled.

Range

$$f\_lower := 9.960 \cdot 10^6 \cdot Hz$$

$$f\_upper := 10.00 \cdot 10^6 \cdot Hz$$

Resolution

$$res := 100 \cdot Hz$$

index

$$f := 1, 2 \,..\, \frac{f\_upper - f\_lower}{res}$$

Frequency array

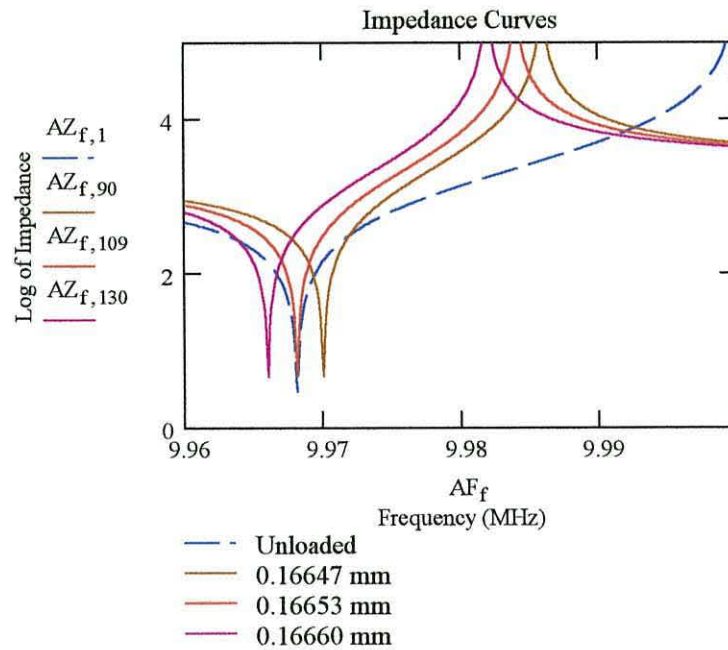$$\omega_f := 2 \cdot \pi \cdot (f\_lower + f \cdot res)$$

## Impedances

The impedances of electro-acoustic model are calculated for the range of frequencies and layer thicknesses defined above.

Electrical Capacitance

$$ZCo_f := \frac{1}{j \cdot \omega_f \cdot Co}$$

Transformer Ratio

$$\Phi := \frac{A \cdot e}{lq}$$

Acoustic Impedances

$$Zk_f := j \cdot \frac{4 \cdot \Phi^2}{\omega_f \cdot Co}$$

$$ZA_f := -2j \cdot A \cdot Zq \cdot \cot\left(\frac{\omega_f \cdot lq}{2 \cdot vq}\right)$$

$$ZB_f := 2j \cdot A \cdot Zq \cdot \tan\left(\frac{\omega_f \cdot lq}{2 \cdot vq}\right)$$

Layer Impedance

$$Z2_{f,1} := A \cdot \rho 2 \cdot v2 \cdot \tanh\left(\frac{j \cdot \omega_f}{vq} \cdot l2_1\right)$$

Total acoustic Impedance

$$Zac_{f,1} := Zk_f + ZA_f + \frac{ZB_f \cdot Z2_{f,1}}{ZB_f + Z2_{f,1}}$$

Transformed to electrical

$$Ztrans_{f,1} := \frac{Zac_{f,1}}{4 \cdot \Phi^2}$$

Total electrical Impedance

$$Z_{f,1} := \frac{ZCo_f \cdot Ztrans_{f,1}}{ZCo_f + Ztrans_{f,1}}$$

## Plotting Impedance Curves

Plot of the magnitude of the impedance against the frequency for varying thickness of matching crystal.

$$AZ_{f,1} := \log\left(\left|Z_{f,1}\cdot mho\right|\right) \qquad AF_f := \frac{\omega_f}{2\cdot\pi\cdot 10^6}$$

Impedance Curves

$AZ_{f,1}$

$AZ_{f,90}$

$AZ_{f,109}$

$AZ_{f,130}$

Log of Impedance

$AF_f$
Frequency (MHz)

— · Unloaded
— 0.16647 mm
— 0.16653 mm
— 0.16660 mm

## Locating Zmin

These programs simulate the action of the measurement system by locating the minimum of each impedance curve.

$$minima(M) := \begin{vmatrix} j \leftarrow 1 \\ a \leftarrow min(M) \\ \text{for } i \in 1..rows(M) \\ \quad minima \leftarrow i \text{ if } M_i = a \\ minima \end{vmatrix}$$

$$mins(M) := \begin{vmatrix} \text{for } i \in 1..cols(M) \\ \quad \begin{vmatrix} \text{for } j \in 1..rows(M) \\ \quad A_j \leftarrow M_{j,i} \\ mins_i \leftarrow minima(A) \end{vmatrix} \\ mins \end{vmatrix}$$

$$idx := mins(AZ)$$

$$Fzmin_1 := \frac{\omega_{(idx_1)}}{2\cdot\pi}$$

$$Zmin_1 := \left|Z_{(idx_1),1}\right|$$

**Plotting f(Zmin) and Zmin**    $1 := 2, 3 .. 200$

**Resonant Frequency**



**Minimum Impedance**

| | |
|---|---|
| **Resonant Frequency of unloaded sensor.** | $\text{Fzmin}_1 = 9.9682 \times 10^6 \, \text{Hz}$ |
| **Impedance of unloaded sensor at resonance** | $\text{Zmin}_1 = 2.916 \, \Omega$ |
| **Resonant Frequency with best matching crystal.** | $\text{Fzmin}_{109} = 9.9682 \times 10^6 \, \text{Hz}$ |
| **Impedance at resonance with best matching crystal** | $\text{Zmin}_{109} = 4.702 \, \Omega$ |
| **Thickness of best matching crystal.** | $l2_{109} = 1.6653 \times 10^{-4} \, \text{m}$ |

# Appendix D - Modelling a Thinning Water Layer

Calculates the expected resonance frequency and impedance when an AT-cut crystal of 10 MHz resonance frequency is loaded by a thinning water layer and a matching crystal.

## Resonator Parameters

This section defines the characteristics of the thickness shear mode resonator.

| | |
|---|---|
| Thickness | $lq := 1.66 \cdot 10^{-4} \cdot m$ |
| Effective Electrode Area | $A := 2.8 \cdot 10^{-5} \cdot m^2$ |
| Permittivity of Quartz | $\varepsilon := 40.71 \cdot 10^{-12} \cdot farad \cdot m^{-1}$ |
| Crystal Capacitance Co | $Co := \dfrac{A \cdot \varepsilon}{lq}$ |
| Density of Quartz | $\rho q := 2650 \cdot kg \cdot m^{-3}$ |
| Shear Wave Velocity in Quartz | $vq := 3320 \cdot m \cdot s^{-1}$ |
| Characteristic Impedance | $Zq := \rho q \cdot vq$ |
| Piezoelectric Coefficient | $e := 9.65 \cdot 10^{-2} \cdot coul \cdot m^{-2}$ |
| Fundamental Resonance fo | $fo := \dfrac{vq}{2 \cdot lq} \qquad \omega o := 2 \cdot \pi \cdot fo$ |

## Layer Parameters

This section defines the characteristics of the water layer and generates an array of thickness values at which the model will be evaluated.

| | | |
|---|---|---|
| Density | $\rho 2 := 1200 \cdot kg \cdot m^{-3}$ | $\rho 3 := \rho q$ |
| Shear Wave Velocity | $vw := 30 \cdot m \cdot s^{-1}$ | $v3 := vq$ |
| Attenuation | $\alpha w := 5.5 \cdot 10^4 \cdot m^{-1}$ | $\alpha 3 := 0$ |
| Thickness (array) | $l := 1, 2 .. 100$ | |
| | $l2_1 := 1 \cdot 10^{-6} \cdot m$ | $l3 := 1.66 \cdot 10^{-4} \cdot m$ |

## Frequency Range

Here an array of frequency values is generated. These are the frequencies at which the system will be modelled.

| | |
|---|---|
| Range | $f\_lower := 9.90 \cdot 10^6 \cdot Hz$ |
| | $f\_upper := 9.98 \cdot 10^6 \cdot Hz$ |
| Resolution | $res := 100 \cdot Hz$ |
| index | $f := 1, 2 .. \dfrac{f\_upper - f\_lower}{res}$ |
| Frequency array | $\omega f := 2 \cdot \pi \cdot (f\_lower + f \cdot res)$ |

## Impedances

The impedances of electro-acoustic model are calculated for the range of frequencies and layer thicknesses defined above.

**Electrical Capacitance**

$$ZCo_f := \frac{1}{j \cdot \omega_f \cdot Co}$$

**Transformer Ratio**

$$\Phi := \frac{A \cdot e}{lq}$$

**Acoustic Impedances**

$$Zk_f := j \cdot \frac{4 \cdot \Phi^2}{\omega_f \cdot Co}$$

$$ZA_f := -2j \cdot A \cdot Zq \cdot \cot\left(\frac{\omega_f \cdot lq}{2 \cdot vq}\right)$$

$$ZB_f := 2j \cdot A \cdot Zq \cdot \tan\left(\frac{\omega_f \cdot lq}{2 \cdot vq}\right)$$

**Layer Impedance**

$$Z3_f := j \cdot A \cdot \rho3 \cdot v3 \cdot \tan\left(\frac{\omega_f}{v3} \cdot l3\right)$$

$$v2_f := \left(\frac{1}{vw} - \frac{j \cdot \alpha w}{\omega_f}\right)^{-1} \qquad \theta2_f := \alpha w + \frac{j \cdot \omega_f}{vw} \qquad z2_f := A \cdot \rho2 \cdot v2_f$$

$$Z2_{f,1} := z2_f \cdot \frac{Z3_f + z2_f \cdot \tanh\left(\theta2_f \cdot l2_1\right)}{z2_f + Z3_f \cdot \tanh\left(\theta2_f \cdot l2_1\right)}$$

**Total acoustic Impedance**

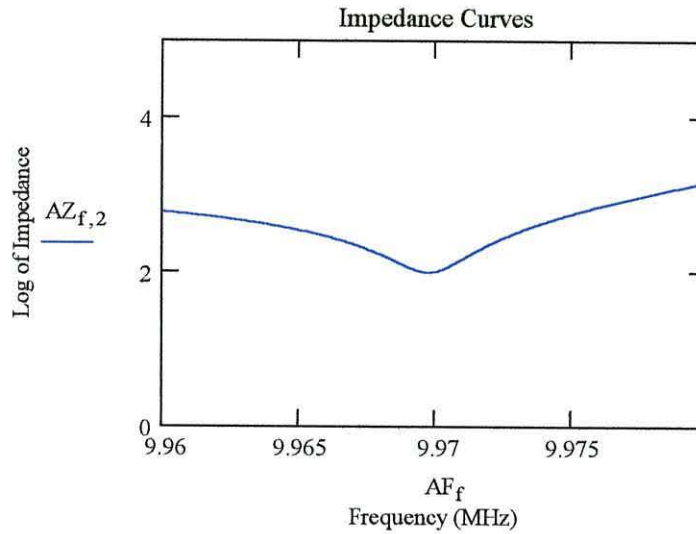$$Zac_{f,1} := Zk_f + ZA_f + \frac{ZB_f \cdot Z2_{f,1}}{ZB_f + Z2_{f,1}}$$

**Transformed to electrical**

$$Ztrans_{f,1} := \frac{Zac_{f,1}}{4 \cdot \Phi^2}$$

**Total electrical Impedance**

$$Z_{f,1} := \frac{ZCo_f \cdot Ztrans_{f,1}}{ZCo_f + Ztrans_{f,1}}$$

## Plotting Impedance Curves

Plot of the magnitude of the impedance against the frequency for varying thickness of matching crystal.

$$AZ_{f,1} := \log\left(\left|Z_{f,1}\cdot \text{mho}\right|\right) \qquad AF_f := \frac{\omega_f}{2\cdot\pi\cdot 10^6}$$

**Impedance Curves**



Log of Impedance $AZ_{f,2}$ — vertical axis
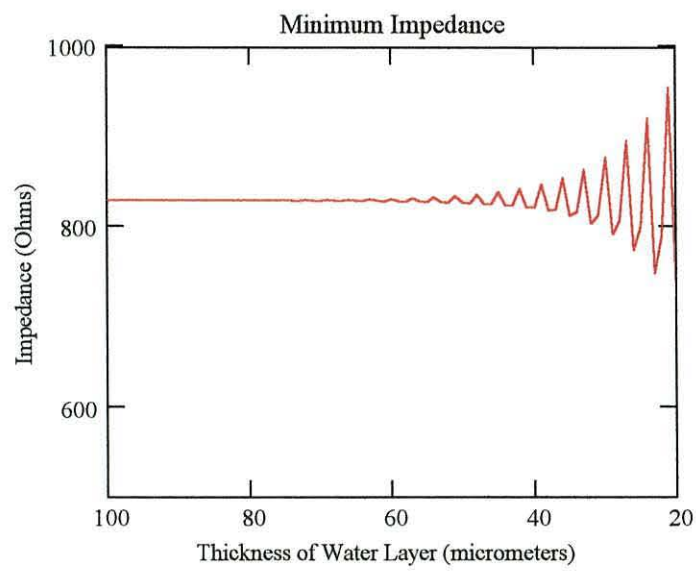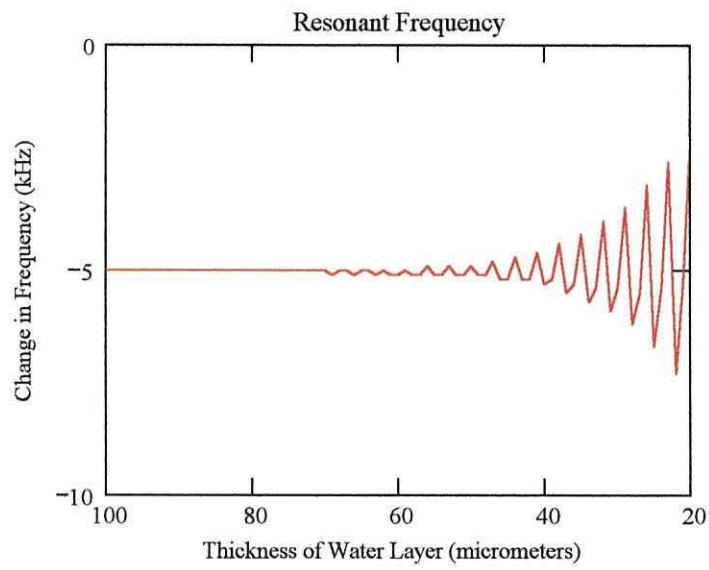
AF_f
Frequency (MHz) — horizontal axis

## Locating Zmin

These programs simulate the action of the measurement system by locating the minimum of each impedance curve.

$$\text{minima}(M) := \begin{vmatrix} j \leftarrow 1 \\ a \leftarrow \min(M) \\ \text{for } i \in 1..\text{rows}(M) \\ \quad \text{minima} \leftarrow i \text{ if } M_i = a \\ \text{minima} \end{vmatrix} \qquad \text{mins}(M) := \begin{vmatrix} \text{for } i \in 1..\text{cols}(M) \\ \quad \begin{vmatrix} \text{for } j \in 1..\text{rows}(M) \\ \quad A_j \leftarrow M_{j,i} \\ \text{mins}_i \leftarrow \text{minima}(A) \end{vmatrix} \\ \text{mins} \end{vmatrix}$$

$$\text{idx} := \text{mins}(AZ)$$

$$\text{Fzmin}_1 := \frac{\omega_{(\text{idx}_1)}}{2\cdot\pi}$$

$$\text{Zmin}_1 := \left|Z_{(\text{idx}_1),1}\right|$$

**Plotting f(Zmin) and Zmin**

### Resonant Frequency



Resonant Frequency

### Minimum Impedance



Minimum Impedance
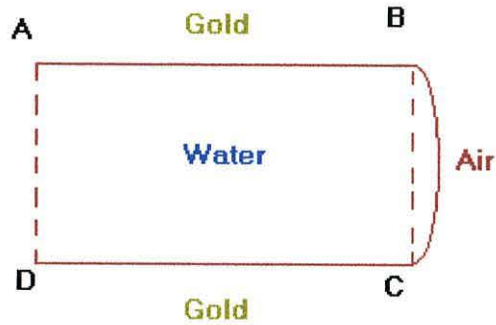
# Appendix E - Analysis of Residual Droplets After Free Fall

Consider a droplet of major radius r1, minor radius, r2 and thickness,s.
One half of the cross section of the droplet can be represented as a rectangle, ABCD, plus a circular segment, BC.

Angle of segment: $\theta = 2 \cdot asin\left(\dfrac{s}{2 \cdot r2}\right)$

Length of segment: $BC = \theta \cdot r2$

Area of segment: $A\_BC = \dfrac{r2^2}{2} \cdot (\theta - \sin(\theta))$

Height of segment: $h = r2 - \sqrt{r2^2 - \dfrac{s^2}{4}}$

Length of rectangle: $AB = r1 - h$

Area of rectangle: $A\_ABCD = s \cdot AB$

Total area: $Area = A\_BC + A\_ABCD$

Distance from centre of droplet to centroid: $Centroid = \dfrac{Area}{2 \cdot s}$

Volume of droplet: $Volume = Area \cdot 2 \cdot \pi \cdot Centroid$    (Pappus-Guldinus theorum)

Area of liquid-gold interface: $LG = 2 \cdot \pi \cdot AB^2$

Distance from centre of droplet to centroid of segment: $Centroid\_BC = \dfrac{Area}{s}$

Area of liquid-air interface: $LA = BC \cdot 2 \cdot \pi \cdot Centroid\_BC$

Surface tension of water: $\gamma := 0.07197 \cdot \dfrac{\text{newton}}{\text{m}}$

$i := 41, 42 .. 100$

Guess volume: $V := 8.1 \cdot 10^{-12} \cdot \text{m}^3$

Separation: $s_i := i \cdot 10^{-6} \cdot \text{m}$

Assume a 90 degree contact angle: $r2 = \dfrac{s}{2}$

Expand expression for volume:

$$\text{Volume} = \left[ \frac{1}{2} \cdot r2^2 \cdot (\theta - \sin(\theta)) + s \cdot \left[ r1 - r2 + \frac{1}{2} \cdot \left( 4 \cdot r2^2 - s^2 \right)^{\left( \frac{1}{2} \right)} \right] \right]^2 \cdot \frac{\pi}{s}$$
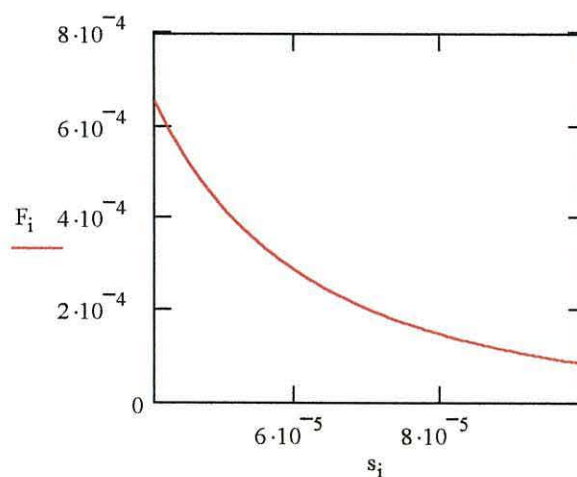
Solve for r1:

$$r1_i := \frac{-1}{(8 \cdot \pi)} \cdot \frac{\left[ -4 \cdot (s_i)^2 \cdot \pi + (s_i)^2 \cdot \pi^2 - 8 \cdot (\pi \cdot V \cdot s_i)^{\left( \frac{1}{2} \right)} \right]}{s_i}$$

Area of interface with top crystal: $A_i := \pi \cdot \left( r1_i - \dfrac{1}{2} \cdot s_i \right)^2$

Pressure across water-air boundary: $\Delta P_i := \gamma \cdot \left( \dfrac{1}{r1_i} + \dfrac{2}{s_i} \right)$

Upward force on top crystal: $F_i := \Delta P_i \cdot A_i$

At equilibrium: $F_{67} = 2.268 \times 10^{-4} \, \text{N}$

# Appendix F - Modelling a Thin Water Layer

Calculates the expected resonance frequency and impedance when an AT-cut crystal of 10 MHz resonance frequency is loaded by a thinning water layer.

## Resonator Parameters

This section defines the characteristics of the thickness shear mode resonator.

| | |
|---|---|
| Thickness | $lq := 1.66 \cdot 10^{-4} \cdot m$ |
| Effective Electrode Area | $A := 2.8 \cdot 10^{-5} \cdot m^2$ |
| Permittivity of Quartz | $\varepsilon := 40.71 \cdot 10^{-12} \cdot farad \cdot m^{-1}$ |
| Crystal Capacitance Co | $Co := \dfrac{A \cdot \varepsilon}{lq}$ |
| Density of Quartz | $\rho q := 2650 \cdot kg \cdot m^{-3}$ |
| Shear Wave Velocity in Quartz | $vq := 3320 \cdot m \cdot s^{-1}$ |
| Characteristic Impedance | $Zq := \rho q \cdot vq$ |
| Piezoelectric Coefficient | $e := 9.65 \cdot 10^{-2} \cdot coul \cdot m^{-2}$ |
| Fundamental Resonance fo | $fo := \dfrac{vq}{2 \cdot lq} \qquad \omega o := 2 \cdot \pi \cdot fo$ |

## Layer Parameters

This section defines the characteristics of the water layer and generates an array of thickness values at which the model will be evaluated.

| | | |
|---|---|---|
| Density | $\rho 2 := 1000 \cdot kg \cdot m^{-3}$ | $\rho 3 := \rho q$ |
| Shear Wave Velocity | $vw := 18 \cdot m \cdot s^{-1}$ | $v3 := vq$ |
| Attenuation | $\alpha w := 3.5 \cdot 10^{6} \cdot m^{-1}$ | $\alpha 3 := 0$ |
| Thickness (array) | $l := 1, 2 .. 100$ | |
| | $l2_l := 1 \cdot 10^{-8} \cdot m$ | $l3 := 1.66 \cdot 10^{-4} \cdot m$ |

## Frequency Range

Here an array of frequency values is generated. These are the frequencies at which the system will be modelled.

| | |
|---|---|
| Range | $\text{f\_lower} := 9.965 \cdot 10^6 \cdot \text{Hz}$ |
| | $\text{f\_upper} := 9.97 \cdot 10^6 \cdot \text{Hz}$ |
| Resolution | $\text{res} := 2 \cdot \text{Hz}$ |
| index | $f := 1, 2 .. \dfrac{\text{f\_upper} - \text{f\_lower}}{\text{res}}$ |
| Frequency array | $\omega_f := 2 \cdot \pi \cdot (\text{f\_lower} + f \cdot \text{res})$ |

## Impedances

The impedances of electro-acoustic model are calculated for the range of frequencies and layer thicknesses defined above.

**Electrical Capacitance**

$$ZCo_f := \frac{1}{j \cdot \omega_f \cdot Co}$$

**Transformer Ratio**

$$\Phi := \frac{A \cdot e}{lq}$$

**Acoustic Impedances**

$$Zk_f := j \cdot \frac{4 \cdot \Phi^2}{\omega_f \cdot Co}$$

$$ZA_f := -2j \cdot A \cdot Zq \cdot \cot\left(\frac{\omega_f \cdot lq}{2 \cdot vq}\right)$$

$$ZB_f := 2j \cdot A \cdot Zq \cdot \tan\left(\frac{\omega_f \cdot lq}{2 \cdot vq}\right)$$

**Layer Impedance**

$$Z3_f := j \cdot A \cdot \rho3 \cdot v3 \cdot \tan\left(\frac{\omega_f}{v3} \cdot l3\right)$$

$$v2_f := \left(\frac{1}{vw} - \frac{j \cdot \alpha w}{\omega_f}\right)^{-1} \qquad \theta2_f := \alpha w + \frac{j \cdot \omega_f}{vw}$$

$$z2_f := 0.06 \cdot A \cdot \rho2 \cdot v2_f$$

$$Z2_{f,1} := z2_f \cdot \frac{Z3_f + z2_f \cdot \tanh\left(\theta2_f \cdot l2_1\right)}{z2_f + Z3_f \cdot \tanh\left(\theta2_f \cdot l2_1\right)}$$

| Total acoustic Impedance | $\mathrm{Zac}_{f,1} := \mathrm{Zk}_f + \mathrm{ZA}_f + \dfrac{\mathrm{ZB}_f \cdot \mathrm{Z2}_{f,1}}{\mathrm{ZB}_f + \mathrm{Z2}_{f,1}}$ |
|---|---|

| Transformed to electrical | $\mathrm{Ztrans}_{f,1} := \dfrac{\mathrm{Zac}_{f,1}}{4 \cdot \Phi^2}$ |
|---|---|

| Total electrical Impedance | $Z_{f,1} := \dfrac{\mathrm{ZCo}_f \cdot \mathrm{Ztrans}_{f,1}}{\mathrm{ZCo}_f + \mathrm{Ztrans}_{f,1}}$ |
|---|---|

## Plotting Impedance Curves

Plot of the magnitude of the impedance against the frequency for varying thickness of matching crystal.

$$AZ_{f,1} := \log\left( \left| Z_{f,1} \cdot \mathrm{mho} \right| \right) \qquad AF_f := \dfrac{\omega_f}{2 \cdot \pi \cdot 10^6}$$



Impedance Curves

Legend:
- Unloaded
- 0.16647 mm
- 0.16653 mm

## Locating Zmin

These programs simulate the action of the measurement system by locating the minimum of each impedance curve.

$$\text{minima}(M) := \begin{vmatrix} j \leftarrow 1 \\ a \leftarrow \min(M) \\ \text{for } i \in 1 .. \text{rows}(M) \\ \quad \text{minima} \leftarrow i \text{ if } M_i = a \\ \text{minima} \end{vmatrix}$$

$$\text{mins}(M) := \begin{vmatrix} \text{for } i \in 1 .. \text{cols}(M) \\ \quad \begin{vmatrix} \text{for } j \in 1 .. \text{rows}(M) \\ \quad A_j \leftarrow M_{j,i} \\ \text{mins}_i \leftarrow \text{minima}(A) \end{vmatrix} \\ \text{mins} \end{vmatrix}$$

$$\text{idx} := \text{mins}(AZ)$$

$$\text{Fzmin}_1 := \frac{\omega_{(\text{idx}_1)}}{2 \cdot \pi}$$

$$\text{Zmin}_1 := \left| Z_{(\text{idx}_1),1} \right|$$

$$R2_1 := \frac{\text{Re}\left[ Z2_{(\text{idx}_1),1} \right]}{A}$$

$$X2_1 := \frac{\text{Im}\left[ Z2_{(\text{idx}_1),1} \right]}{A}$$

## Plotting f(Zmin) and Zmin



Resonant Frequency
(x-axis: Thickness of Water Layer (micrometers); y-axis: Change in Frequency (kHz))

## Minimum Impedance
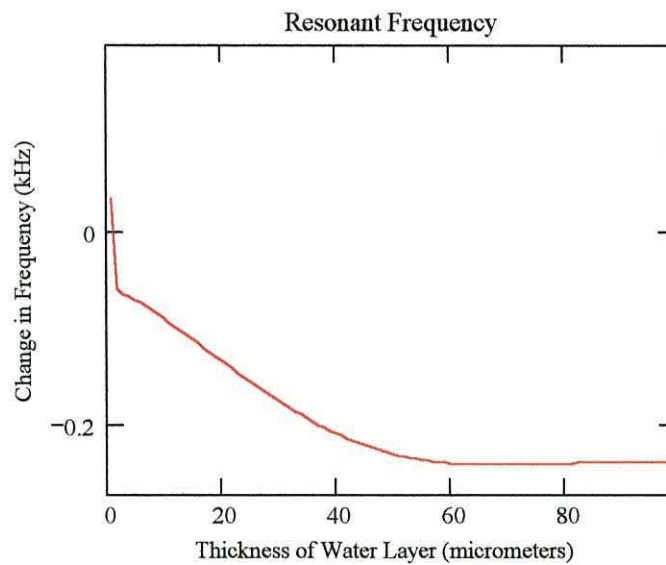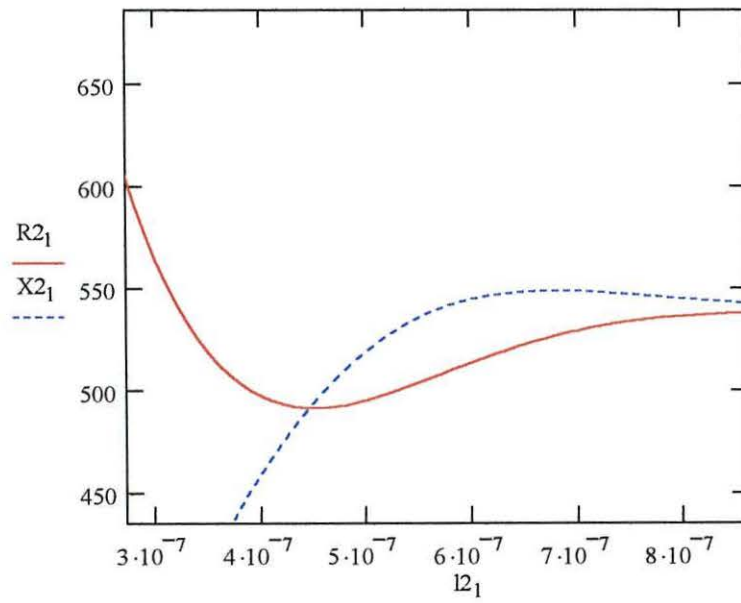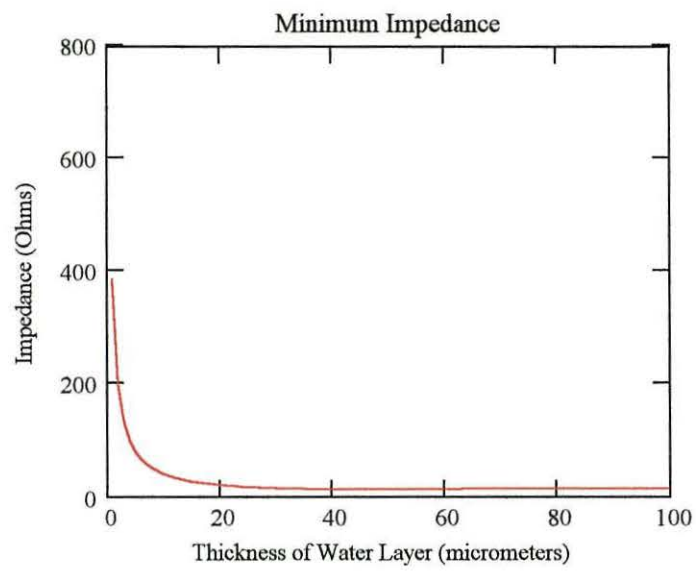
# Appendix G - Modelling a Very Thin Layer

Calculates the expected resonance frequency and impedance when a quartz layer of variable thickness is in good acoustic contact with the surface of an active AT-cut crystal of 10 MHz resonance frequency.

## Resonator Parameters

This section defines the characteristics of the thickness shear mode resonator.

| | |
|---|---|
| Thickness | $lq := 1.66 \cdot 10^{-4} \cdot m$ |
| Effective Electrode Area | $A := 2.8 \cdot 10^{-5} \cdot m^2$ |
| Permittivity of Quartz | $\varepsilon := 40.71 \cdot 10^{-12} \cdot farad \cdot m^{-1}$ |
| Crystal Capacitance Co | $Co := \dfrac{A \cdot \varepsilon}{lq}$ |
| Density of Quartz | $\rho q := 2650 \cdot kg \cdot m^{-3}$ |
| Shear Wave Velocity in Quartz | $vq := 3320 \cdot m \cdot s^{-1}$ |
| Characteristic Impedance | $Zq := \rho q \cdot vq$ |
| Piezoelectric Coefficient | $e := 9.65 \cdot 10^{-2} \cdot coul \cdot m^{-2}$ |
| Fundamental Resonance fo | $fo := \dfrac{vq}{2 \cdot lq} \qquad \omega o := 2 \cdot \pi \cdot fo$ |

# Thickness

## Layer Parameters

This section defines the characteristics of the second layer and generates an array of thickness values at which the model will be evaluated.

| | |
|---|---|
| Density | $\rho 2 := 1000 \cdot kg \cdot m^{-3}$ |
| Shear Wave Velocity | $v2 := 10 \cdot m \cdot sec^{-1}$ |
| Attenuation | $\alpha := 4 \cdot 10^{6} \cdot m^{-1}$ |
| Thickness (array) | $l := 1, 2 .. 101$ |
| | $l2_l := (l - 1) \cdot 5 \cdot 10^{-11} \cdot m$ |

## Frequency Range

Here an array of frequency values is generated. These are the frequencies at which the system will be modelled.

Range

$$f\_lower := 9.960 \cdot 10^6 \cdot Hz$$

$$f\_upper := 10.00 \cdot 10^6 \cdot Hz$$

Resolution

$$res := 100 \cdot Hz$$

index

$$f := 1, 2 .. \frac{f\_upper - f\_lower}{res}$$

Frequency array

$$\omega_f := 2 \cdot \pi \cdot (f\_lower + f \cdot res)$$

## Impedances
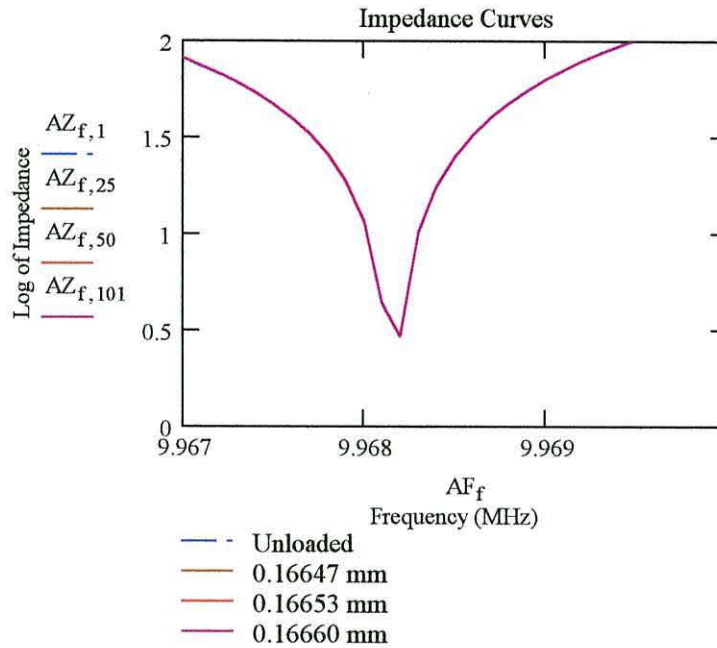
The impedances of electro-acoustic model are calculated for the range of frequencies and layer thicknesses defined above.

Electrical Capacitance

$$ZCo_f := \frac{1}{j \cdot \omega_f \cdot Co}$$

Transformer Ratio

$$\Phi := \frac{A \cdot e}{lq}$$

Acoustic Impedances

$$Zk_f := j \cdot \frac{4 \cdot \Phi^2}{\omega_f \cdot Co}$$

$$ZA_f := -2j \cdot A \cdot Zq \cdot \cot\left(\frac{\omega_f \cdot lq}{2 \cdot vq}\right)$$

$$ZB_f := 2j \cdot A \cdot Zq \cdot \tan\left(\frac{\omega_f \cdot lq}{2 \cdot vq}\right)$$

Layer Impedance

$$Z2_{f,1} := A \cdot \rho2 \cdot v2 \cdot \tanh\left(\frac{j \cdot \omega_f}{vq} \cdot l2_1\right)$$

Total acoustic Impedance

$$Zac_{f,1} := Zk_f + ZA_f + \frac{ZB_f \cdot Z2_{f,1}}{ZB_f + Z2_{f,1}}$$

Transformed to electrical

$$Ztrans_{f,1} := \frac{Zac_{f,1}}{4 \cdot \Phi^2}$$

Total electrical Impedance

$$Z_{f,1} := \frac{ZCo_f \cdot Ztrans_{f,1}}{ZCo_f + Ztrans_{f,1}}$$

## Plotting Impedance Curves

Plot of the magnitude of the impedance against the frequency for varying thickness of matching crystal.

$$AZ_{f,1} := \log\left(\left|Z_{f,1} \cdot mho\right|\right) \qquad AF_f := \frac{\omega_f}{2 \cdot \pi \cdot 10^6}$$

**Impedance Curves**



Frequency axis: $AF_f$ — Frequency (MHz), ranging 9.967, 9.968, 9.969
Vertical axis: Log of Impedance, 0 to 2

Legend:
- — · Unloaded
- —— 0.16647 mm
- —— 0.16653 mm
- —— 0.16660 mm

Y-axis labels: $AZ_{f,1}$, $AZ_{f,25}$, $AZ_{f,50}$, $AZ_{f,101}$

## Locating Zmin

These programs simulate the action of the measurement system by locating the minimum of each impedance curve.

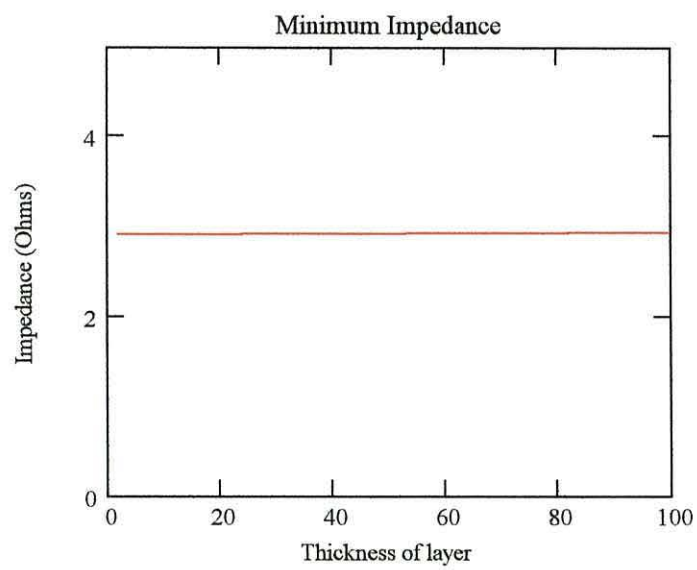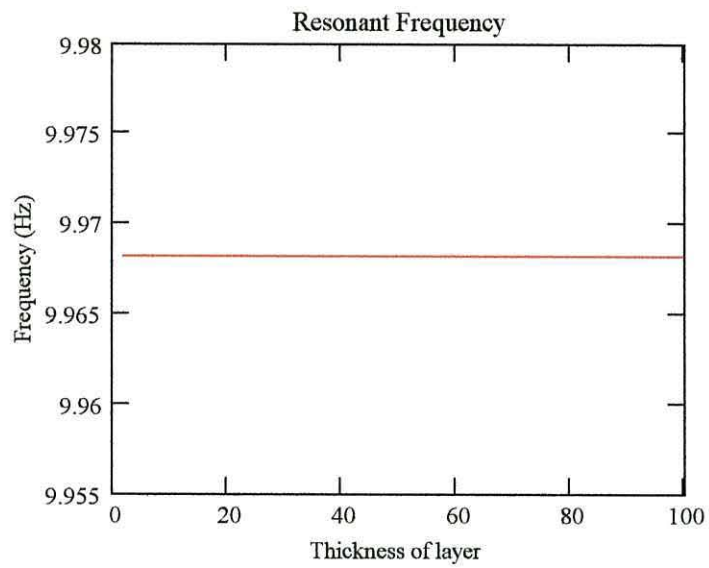$$minima(M) := \begin{vmatrix} j \leftarrow 1 \\ a \leftarrow min(M) \\ \text{for } i \in 1 .. rows(M) \\ \quad minima \leftarrow i \text{ if } M_i = a \\ minima \end{vmatrix}$$

$$mins(M) := \begin{vmatrix} \text{for } i \in 1 .. cols(M) \\ \quad \begin{vmatrix} \text{for } j \in 1 .. rows(M) \\ \quad A_j \leftarrow M_{j,i} \\ mins_i \leftarrow minima(A) \end{vmatrix} \\ mins \end{vmatrix}$$

$$idx := mins(AZ)$$

$$Fzmin_1 := \frac{\omega_{(idx_1)}}{2 \cdot \pi}$$

$$Zmin_1 := \left|Z_{(idx_1),1}\right|$$

**Plotting f(Zmin) and Zmin**     $1 := 2, 3 .. 200$



Resonant Frequency



Minimum Impedance

# Velocity

### Layer Parameters

This section defines the characteristics of the second layer and generates an array of thickness values at which the model will be evaluated.

Density

$$\rho2 := 1000 \cdot kg \cdot m^{-3}$$

Shear Wave Velocity    $l := 1, 2 .. 150$    $v2_l := 0.1 \cdot l \cdot m \cdot sec^{-1}$

Attenuation

$$\alpha := 4 \cdot 10^6 \cdot m^{-1}$$

Thickness

$$l2 := 3 \cdot 10^{-9} \cdot m$$

### Impedances

The impedances of electro-acoustic model are calculated for the range of frequencies and layer thicknesses defined above.

Electrical Capacitance

$$ZCo_f := \frac{1}{j \cdot \omega_f \cdot Co}$$

Transformer Ratio

$$\Phi := \frac{A \cdot e}{lq}$$

Acoustic Impedances

$$Zk_f := j \cdot \frac{4 \cdot \Phi^2}{\omega_f \cdot Co}$$

$$ZA_f := -2j \cdot A \cdot Zq \cdot \cot\left(\frac{\omega_f \cdot lq}{2 \cdot vq}\right)$$

$$ZB_f := 2j \cdot A \cdot Zq \cdot \tan\left(\frac{\omega_f \cdot lq}{2 \cdot vq}\right)$$

Layer Impedance

$$Z2_{f,1} := A \cdot \rho2 \cdot v2_1 \cdot \tanh\left(\frac{j \cdot \omega_f}{vq} \cdot l2\right)$$

Total acoustic Impedance

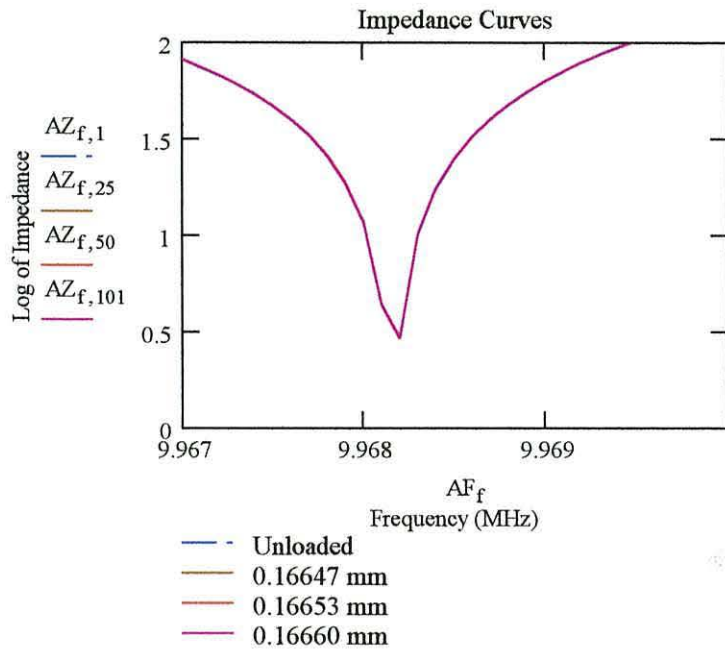$$Zac_{f,1} := Zk_f + ZA_f + \frac{ZB_f \cdot Z2_{f,1}}{ZB_f + Z2_{f,1}}$$

Transformed to electrical

$$Ztrans_{f,1} := \frac{Zac_{f,1}}{4 \cdot \Phi^2}$$

Total electrical Impedance

$$Z_{f,1} := \frac{ZCo_f \cdot Ztrans_{f,1}}{ZCo_f + Ztrans_{f,1}}$$

## Plotting Impedance Curves

Plot of the magnitude of the impedance against the frequency for varying thickness of matching crystal.

$$AZ_{f,1} := \log\left(\left|Z_{f,1} \cdot mho\right|\right) \qquad AF_f := \frac{\omega_f}{2 \cdot \pi \cdot 10^6}$$

**Impedance Curves**



Log of Impedance

$AZ_{f,1}$
$AZ_{f,25}$
$AZ_{f,50}$
$AZ_{f,101}$

$AF_f$
Frequency (MHz)

— · Unloaded
—— 0.16647 mm
—— 0.16653 mm
—— 0.16660 mm

## Locating Zmin
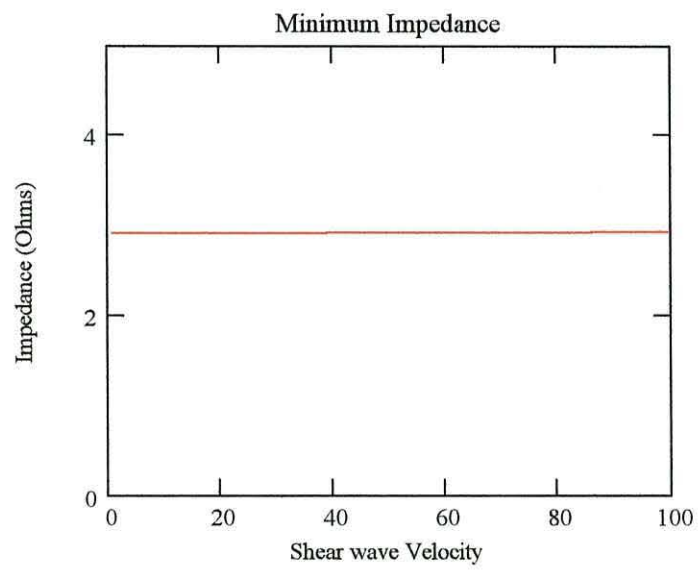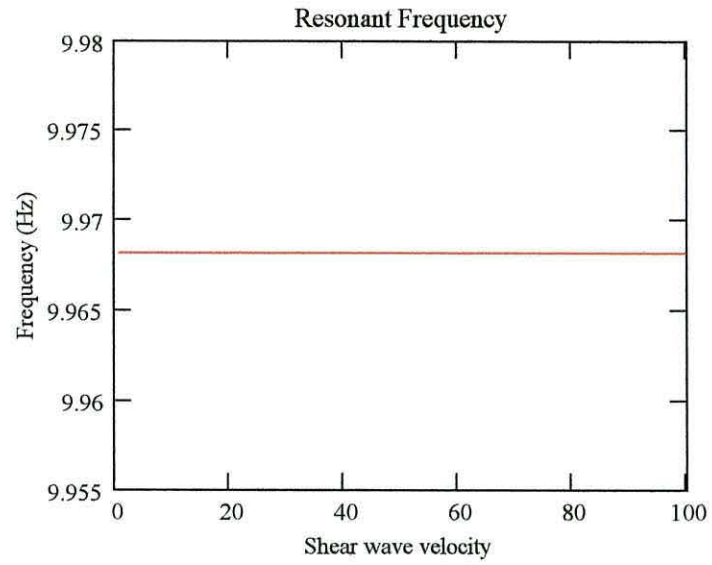
These programs simulate the action of the measurement system by locating the minimum of each impedance curve.

$$minima(M) := \begin{vmatrix} j \leftarrow 1 \\ a \leftarrow \min(M) \\ \text{for } i \in 1 .. rows(M) \\ \quad minima \leftarrow i \text{ if } M_i = a \\ minima \end{vmatrix} \qquad mins(M) := \begin{vmatrix} \text{for } i \in 1 .. cols(M) \\ \quad \text{for } j \in 1 .. rows(M) \\ \qquad A_j \leftarrow M_{j,i} \\ \quad mins_i \leftarrow minima(A) \\ mins \end{vmatrix}$$

$$idx := mins(AZ)$$

$$Fzmin_1 := \frac{\omega_{\left(idx_1\right)}}{2 \cdot \pi}$$

$$Zmin_1 := \left|Z_{\left(idx_1\right),1}\right|$$

**Plotting f(Zmin) and Zmin**

### Resonant Frequency



### Minimum Impedance

# Attenuation

## Layer Parameters

This section defines the characteristics of the second layer and generates an array of thickness values at which the model will be evaluated.

Density $\quad \rho2 := 1000 \cdot kg \cdot m^{-3}$

Attenuation $\quad 1 := 1, 2 .. 100 \quad \alpha_1 := 2 \cdot 1 \cdot 10^4 \cdot m^{-1}$ $\qquad$ Shear Wave Velocity

Thickness $\qquad 12 := 3 \cdot 10^{-9} \cdot m$

$$v := 10 \cdot m \cdot sec^{-1} \quad v2_1 := \left( \frac{1}{v} - \frac{j \cdot \alpha_1}{\omega_1} \right)^{-1}$$

## Impedances

The impedances of electro-acoustic model are calculated for the range of frequencies and layer thicknesses defined above.

Electrical Capacitance $\qquad ZCo_f := \dfrac{1}{j \cdot \omega_f \cdot Co}$

Transformer Ratio $\qquad \Phi := \dfrac{A \cdot e}{lq}$

Acoustic Impedances $\qquad Zk_f := j \cdot \dfrac{4 \cdot \Phi^2}{\omega_f \cdot Co}$

$$ZA_f := -2j \cdot A \cdot Zq \cdot cot\left( \frac{\omega_f \cdot lq}{2 \cdot vq} \right)$$

$$ZB_f := 2j \cdot A \cdot Zq \cdot tan\left( \frac{\omega_f \cdot lq}{2 \cdot vq} \right)$$

Layer Impedance $\qquad Z2_{f,1} := A \cdot \rho2 \cdot v2_1 \cdot tanh\left( \dfrac{j \cdot \omega_f}{vq} \cdot 12 \right)$

Total acoustic Impedance $\qquad Zac_{f,1} := Zk_f + ZA_f + \dfrac{ZB_f \cdot Z2_{f,1}}{ZB_f + Z2_{f,1}}$
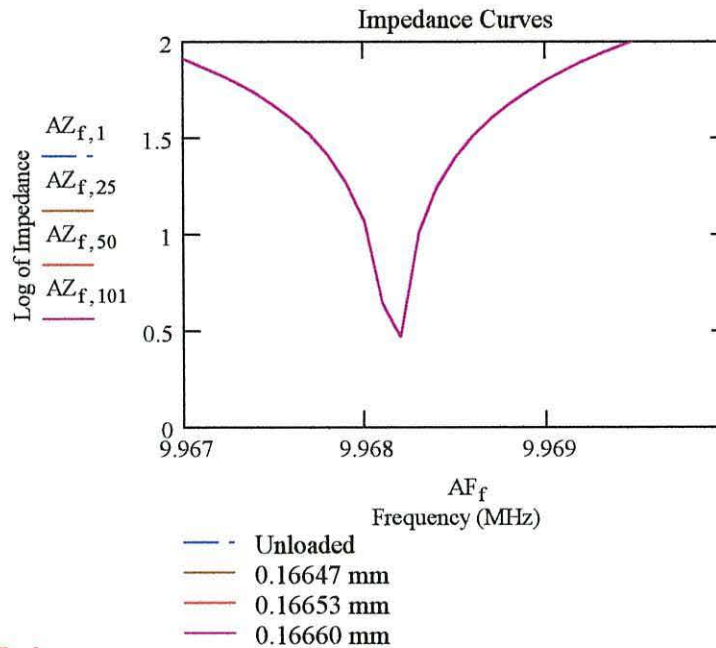
Transformed to electrical $\qquad Ztrans_{f,1} := \dfrac{Zac_{f,1}}{4 \cdot \Phi^2}$

Total electrical Impedance $\qquad Z_{f,1} := \dfrac{ZCo_f \cdot Ztrans_{f,1}}{ZCo_f + Ztrans_{f,1}}$

## Plotting Impedance Curves

Plot of the magnitude of the impedance against the frequency for varying thickness of matching crystal.

$$AZ_{f,1} := \log\left(\left|Z_{f,1}\cdot mho\right|\right) \qquad AF_f := \frac{\omega_f}{2\cdot\pi\cdot 10^6}$$



Impedance Curves

- — - Unloaded
- ——— 0.16647 mm
- ——— 0.16653 mm
- ——— 0.16660 mm

## Locating Zmin

These programs simulate the action of the measurement system by locating the minimum of each impedance curve.

$$minima(M) := \begin{vmatrix} j \leftarrow 1 \\ a \leftarrow min(M) \\ \text{for } i \in 1..rows(M) \\ \quad minima \leftarrow i \text{ if } M_i = a \\ minima \end{vmatrix}$$

$$mins(M) := \begin{vmatrix} \text{for } i \in 1..cols(M) \\ \quad \text{for } j \in 1..rows(M) \\ \quad\quad A_j \leftarrow M_{j,i} \\ \quad mins_i \leftarrow minima(A) \\ mins \end{vmatrix}$$

$$idx := mins(AZ)$$

$$Fzmin_1 := \frac{\omega_{(idx_1)}}{2\cdot\pi}$$

$$Zmin_1 := \left|Z_{(idx_1),1}\right|$$

## Plotting f(Zmin) and Zmin



Resonant Frequency



Minimum Impedance